ABSTRACT

Title of dissertation: TOPOLOGICAL SUPERCONDUCTIVITY AND MAJORANA ZERO MODES

FNU Setiawan, Doctor of Philosophy, 2017

Dissertation directed by: Professor Sankar Das Sarma
Department of Physics

Recent years have seen a surge interest in realizing Majorana zero modes in condensed matter systems. Majorana zero modes are zero-energy quasiparticle excitations which are their own anti-particles. The topologically degenerate Hilbert space and non-Abelian statistics associated with Majorana zero modes renders them useful for realizing topological quantum computation. These Majorana zero modes can be found at the boundary of a topological superconductor. While preliminary evidence for Majorana zero modes in form of zero-bias conductance peaks have already been observed, confirmatory signatures of Majorana zero modes are still lacking.

In this thesis, we theoretically investigate the robustness of several signatures of Majorana zero modes, thereby suggesting improvement and directions that can be pursued for an unambiguous identification of the Majorana zero modes. We begin by studying analytically the differential conductance of the normal-metal–topological superconductor junction across the topological transition within the Blonder-Tinkham-Klapwijk formalism. We show that despite being quantized in the topological regime, the zero-bias conductance only develops as a peak in the conductance spectra for sufficiently small junction transparencies, or for small and

large spin-orbit coupling strength. We proceed to investigate the signatures of Majorana zero modes in superconductor–normal-metal–superconductor junctions and show that the conductance quantization in this junction is not robust against increasing junction transparency. Finally, we propose a dynamical scheme to study the short-lived topological phases in ultracold systems by first preparing the systems in its long-lived non-topological phases and then driving it into the topological phases and back. We find that the excitations' momentum distributions exhibit Stückelberg oscillations and Kibble-Zurek scaling characteristic of the topological quantum phase transition, thus provides a bulk probe for the topological phase.

TOPOLOGICAL SUPERCONDUCTIVITY AND MAJORANA ZERO MODES

by

FNU Setiawan

Dissertation submitted to the Faculty of the Graduate School of the
University of Maryland, College Park in partial fulfillment
of the requirements for the degree of
Doctor of Philosophy
2017

Advisory Committee:
Professor Sankar Das Sarma, Chair/Advisor
Assistant Professor Jay Deep Sau
Assistant Professor Maissam Barkeshli
Professor Theodore L. Einstein
Professor Christopher Jarzynski

Acknowledgments

First and foremost, I would like to express my sincere gratitude to my advisor, Professor Sankar Das Sarma for his guidance and support of my research. I have benefited a lot from his enthusiasm and insight in physics. This thesis would not have been possible without his insight and advice. I am also greatly indebted to Professor Jay D. Sau for his excellent mentorship. I am always amazed by his quick grasp of the problem at hand and his ability to give an insightful guidance on how to solve the problem. I am truly grateful for his careful guidance and support.

I would like to thank Professors Maissam Barkeshli, Theodore Einstein, and Christopher Jarzynski for serving as my dissertation committee.

I have greatly benefited from the interaction with Professor Jason Kestner, Xin Wang, and Hoi-Yin Hui during my initial stage of Ph.D. research on the subject of spin qubit. I have also enjoyed my collaboration with other postdoctoral researchers in Condensed Matter Theory Center, including Dong-Ling Deng, William S. Cole, Jedediah Pixley, and Philip Brydon. I would like to express my gratitude for their time and patience. Besides, I had the privilege to collaborate with Professors Ian Spielman and Krishnendu Sengupta on the subject of ultracold atoms. The discussion with them had greatly widened my horizon on the subject of cold atomic physics.

I had a fun time taking courses together with Chiao-Hsuan Wang, Amit Nag, Chunxiao Liu, Qin Liu and Renxiong Wang. The friendship with them will be something that I will always cherish. My days at University of Maryland would

not be as much fun without a whole bunch of friends, notably, Xiao Li, Xiaopeng Li, Ching-Kai Chiu, Edwin Barnes, Mehdi Kargarian, Johannes Hofmann, Valentin Stanev, Yang-Le Wu, Sriram Ganeshan, Yahya Alavirad, Yi-Hsieh Wang, Xunnong Xu, Junhyun Lee, Juraj Radic, Hilary Hurst, Andrew Allocca, Lance Boyer, Pallab Goswami, David Clarke, Yidan Wang, Yingyi Huang, Zach Raines, Yang Song and Aydin Keser.

This thesis would not have been possible without the support from the NSF-funded Physics Frontier Center at the Joint Quantum Institute (PFC@JQI). In particular, I am thankful to Professors Luis Orozco and William Phillips who have supported my research activities through PFC@JQI.

Last but not least, I owe most to my parents and my sister for their love and supports.

Table of Contents

List of Tables

List of Figures

List of Abbreviations

MZM	Majorana Zero Mode
nD	n-dimension(al)
ZB(C)P	Zero-Bias (Conductance) Peak
BTK	Blonder-Tinkham-Klapwijk
BCS	Bardeen-Cooper-Schrieffer
NS	Normal metal–Superconductor
SNS	Superconductor–Normal metal–Superconductor
SGS	Subharmonic Gap Structure
SC	Superconductor / Superconductivity
SF	Superfluid
SOC	Spin-orbit coupling / Spin-orbit-coupled
STM	Scanning Tunneling Microscope
BdG	Bogoliubov de-Gennes
SOCSW	Spin-Orbit-Coupled Superconducting wire
SOCFG	Spin-Orbit-Coupled Fermi Gases
MAR	Multiple Andreev Reflections
NN	Normal–Normal
NM	Normal Metal
KZ	Kibble-Zurek
LZ	Landau-Zener
ABS	Andreev Bound State
SRMD	Spin-Resolved Momentum Distribution
td-BdGE	time-dependent Bogoliubov-de Gennes Equation
TQPT	Topological Quantum Phase Transition
TSF	Topological Superfluid
pSC	p-wave superconductor
sSC	s-wave superconductor

Chapter 1

Introduction

In 1937, Ettore Majorana showed that the complex Dirac equation admits real solutions which describe a charge-neutral fermion being its own antiparticle [1]. This particle was later dubbed as the Majorana fermion, and its discovery has since influenced many areas of physics ranging from nuclear and particle physics to condensed matter physics. In the context of high energy physics, the proposition that neutrinos may be Majorana fermions has remained to date unsettled. In condensed matter physics, Majorana fermions can exist as quasiparticle excitations in superconductors. Since this quasiparticle excitation occurs as a zero-energy midgap excitation and is bound to defects [2], it is commonly referred to as the "Majorana zero mode" (MZM) or "Majorana bound state". This MZM can be found at the boundary of one-dimensional (1D) topological superconductors [3] or vortices in two-dimensional (2D) topological superconductor [4, 5].

The earliest proposals to realize MZMs in superconductors can be traced back to nearly two decades ago [3, 4, 5, 6, 7, 8, 9]. A necessary ingredient in these proposals is the exotic p-wave pairing potential. The progress in experiments using these systems, however, is hampered by the stringent experimental requirements. The recent proposals to realize the topological superconductor by combining the

conventional s-wave superconductor, magnetic interaction and spin-orbit coupling (SOC) [10, 11, 12, 13, 14, 15] has opened a new chapter in the development of the field. The most promising of these proposals involves proximity-inducing superconductivity in a spin-orbit-coupled semiconducting nanowire in the presence of a magnetic field [13, 14, 15]. By simply increasing the magnetic field strength above a critical value, the system can be tuned to the topological regime where the MZMs appear at the end of the nanowire. The simplicity of this setup has motivated several experimental groups to study such a topological superconductor [16, 17, 18, 19, 20, 21, 22, 23, 24]. The excitement in this subject has also resulted in a number of review and popular articles [25, 26, 27, 28, 29, 30, 31].

One of the key signatures of the MZM is the quantized value $2e^2/h$ of the differential conductance for tunneling into the nanowire at zero-bias voltage. This quantized conductance is due to perfect Andreev reflection facilitated by the MZM [32, 33, 34, 35, 36]. For a sufficiently high tunnel barrier, the conductance spectra will develop a zero-bias peak with this value. While recent experimental results clearly indicate the appearance of a zero-bias tunneling conductance peak upon tuning the system into the topological regime, the observed zero-bias conductance value is far below the quantized value.

In this thesis, we investigate in detail several signatures of MZMs in 1D topological superconductors, thereby suggesting improvement and directions that can be pursued for an unambiguous identification of the MZMs. In the introductory chapter, we start by giving an overview of MZMs. We then proceed to review two models of 1D topological superconductor which host the MZMs: (i) a spin-

less p-wave superconductor and (ii) a spin-split spin-orbit-coupled superconducting wire (SOCSW). Finally, we discuss several signatures of topological superconductor, namely, the zero-bias conductance of normal-metal–superconductor (NS) junctions, the gap-bias conductance of superconductor–normal-metal–superconductor (SNS) junctions and the zero-momentum gap-closing in the energy spectrum as the system is driven through the topological quantum phase transition (TQPT).

1.1 Overview of Majorana Zero Modes

In solid state systems, electrons and holes are the particle and antiparticle analogues in the high energy context. Since MZMs are their own antiparticles, it must then be equal superpositions of electrons and holes. Since the quasiparticle excitations in superconductors are superpositions of electrons and holes, this suggests that MZMs can exist as the mid-gap excitations in a superconductor with zero energy and charge. This fact follows from the particle-hole symmetry of the superconductor quasiparticle creation and annihilation operators, i.e.,

$$\gamma(E) = \gamma^{\dagger}(-E), \tag{1.1}$$

which implies that at the Fermi energy ($E = 0$ which is in the middle of the superconductor gap), $\gamma = \gamma^{\dagger}$ where $\gamma, \gamma^{\dagger}$ are creation and annihilation operators at zero energy (Majorana operators). The Majorana operators satisfy the following anticommutation relation

$$\{\gamma_n, \gamma_m\} = 2\delta_{nm}. \tag{1.2}$$

In addition, they also commute with the Hamiltonian:

$$[H, \gamma_n] = 0. \tag{1.3}$$

This relation implies that the presence of MZMs leads to ground state degeneracies, i.e., the states $|\mathrm{GS}\rangle$ and $\gamma_n |\mathrm{GS}\rangle$ are both the ground states. In general, a system with $2N$ MZMS $\gamma_1, \gamma_2, \ldots, \gamma_{2N}$ has 2^N degenerate ground states. This can be understood by first expressing the fermion operators c_n in terms of the Majorana operators, i.e.,

$$c_n = \frac{1}{2}\left(\gamma_{2n-1} + i\gamma_{2n}\right), \quad \text{for } n = 1, \cdots, N. \tag{1.4}$$

The operators c_n satisfy the usual fermionic anticommutation relation:

$$\left\{c_m, c_n^\dagger\right\} = \delta_{mn}, \tag{1.5}$$

$$\{c_m, c_n\} = 0. \tag{1.6}$$

Since there are N number operators $c_n^\dagger c_n = \frac{1}{2}\left(1 + i\gamma_{2n-1}\gamma_{2n}\right)$, where each of them can either assume a value of 0 and 1, this means that the ground state of the system is 2^N-fold degenerate.

These unpaired MZMs are topologically protected as they are localized states with an energy gap separating them from the excited states. This implies that any continuous deformation of the Hamiltonian that does not close the energy gap will not destroy the MZMs. The topological protection render the MZMs with

the capability for a fault-tolerant topological quantum computation, a quantum computational scheme which is robust against local noise [37].

1.2 Topological Superconductors

In this section, we study the systems which support the MZMs. We will call such systems as *topological* systems with MZM being the topological state. As discussed previously, MZM can exist as a zero-energy mode in superconductors. To realize these unpaired MZMs, spin degeneracy needs to be lifted in the superconductor. This necessitates either the use of exotic p-wave pairing potential or the combination of magnetic field and SOC for s-wave pairing potential. We will begin by studying the simplest model of topological superconductor, namely the spinless p-wave superconductor. Afterwards, we will proceed to discuss a more physically realistic model, namely a semiconducting nanowire placed in proximity to an s-wave superconductor in the presence of magnetic field.

1.2.1 1D Spinless p-wave Superconductor

In 2000, Alexei Kitaev proposed a simple model of topological superconductor, namely a 1D spinless p-wave superconductor [3]. The lattice Hamiltonian for this model is given by

$$H = -\mu_p \sum_{n=1}^{N} c_n^\dagger c_n - \sum_{n=1}^{N-1} \left(t c_n^\dagger c_{n+1} + \Delta_p e^{i\phi} c_n c_{n+1} + \text{h.c.} \right), \tag{1.7}$$

where $c_n^\dagger, c_n$ are the electron creation and annihilation operators at site n, respectively, μ_p is the p-wave superconductor chemical potential, $t \geq 0$ is the nearest-neighbor hopping, $\Delta_p e^{i\phi}$ is the p-wave pairing between adjacent sites, and h.c. denotes the Hermitian conjugation.

Let us now rewrite the above Hamiltonian by expressing the fermion creation and annihilation operators in terms of the Majorana operators, i.e.,

$$c_n = \frac{e^{-i\phi/2}}{2}\left(\gamma_{2n} + i\gamma_{2n-1}\right), \tag{1.8}$$

where γ_{2n-1} and γ_{2n} are the Majorana operators at the n^{th} site. In this basis, the Hamiltonian becomes

$$H = -\frac{\mu_p}{2}\sum_{n=1}^{N}\left(1 + i\gamma_{2n}\gamma_{2n-1}\right) - \frac{i}{2}\sum_{n=1}^{N-1}\left[\left(\Delta_p + t\right)\gamma_{2n}\gamma_{2n+1} + \left(\Delta_p - t\right)\gamma_{2n-1}\gamma_{2n+2}\right]. \tag{1.9}$$

The appearance of the MZMs in this Hamiltonian can be easily identified by working in two special limits. The first limit is when $\mu_p = 0$ and $t = \Delta_p \neq 0$ where the Hamiltonian becomes

$$H = -it\sum_{n=1}^{N-1}\gamma_{2n}\gamma_{2n+1}. \tag{1.10}$$

In this limit, the Majorana modes pair up between adjacent lattice sites except the Majorana modes at the end [see Fig. 1.1(a)]. By rewriting the Hamiltonian in terms

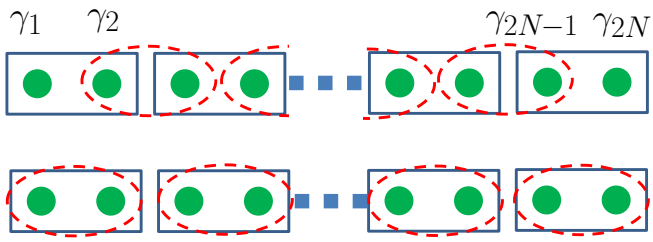

Figure 1.1: Schematic diagram of the Kitaev Model using Majorana representation [Eq. (1.7)] for different parameter regimes: (a) $\mu_p = 0$, $t = \Delta_p \neq 0$ (b) $\mu_p \neq 0$, $t = \Delta_p = 0$. The fermion at each site c_n is represented using two Majorana operators $\gamma_{2n-1,2n}$ (green disk).

of the fermion operator $\tilde{c}_n = \frac{1}{2}(\gamma_{2n+1} + i\gamma_{2n})$, we have

$$H = t \sum_{n=1}^{N-1} \left(\tilde{c}_n^\dagger \tilde{c}_n - \frac{1}{2} \right). \tag{1.11}$$

We can see from the above Hamiltonian that there is no energy needed to add the non-local fermion $f = \frac{1}{2}(\gamma_1 + i\gamma_{2N})$ into the system. This means that the system supports two zero-energy Majorana modes where the ground state of the system is two-fold degenerate, i.e., $|GS\rangle$ and $f^\dagger|GS\rangle$ are both the ground state of the system.

Even though in the above, we only deal with a specific value of parameters, the MZMs in this model persists as long as the bulk gap is finite. To understand this, let us rewrite the Hamiltonian [Eq. (1.7)] in the Bogoliubov-de Gennes (BdG) form as

$$H = \frac{1}{2} C^\dagger H_{\text{BdG}} C, \tag{1.12}$$

where $C = (c_1, \cdots, c_N, c_1^\dagger, \cdots, c_N^\dagger)^T$ is a column vector which contains the electron annihilation and creation operators at all sites. The BdG Hamiltonian H_{BdG} is a $2N \times 2N$ matrix and can be written more compactly using the Pauli matrices τ in

particle-hole space and position basis vector $|n\rangle$ as

$$H_{\mathrm{BdG}} = -\sum_n \mu_p \tau_z |n\rangle\langle n| - \sum_n [(t\tau_z - i\Delta_p \tau_y)|n\rangle\langle n+1| + \mathrm{h.c.}]. \tag{1.13}$$

The BdG Hamiltonian operates on the basis states $|n\rangle|\tau\rangle$ where $\tau = \pm 1$ denotes the electron and hole states, respectively. Note that in the above, we take the superconducting phase $\phi = 0$, which we are going to do for the remaining of this thesis. In this BdG form, we can see that the Hamiltonian respects the particle-hole symmetry, i.e., $\mathcal{P} H_{\mathrm{BdG}} \mathcal{P}^{-1}$ where the particle-hole operator is $\mathcal{P} = \tau_x \mathcal{K}$ with $\mathcal{K}$ being the complex conjugation operator.

Since the energy spectrum is particle-hole symmetric, moving the MZMs individually from zero energy is not allowed. For a chain which is sufficiently long that the coupling between the MZMs is small, the only way to split the MZMs into two non-degenerate state at finite energy is to close the bulk gap. The bulk spectrum is given by

$$E_{\mathrm{bulk}}(k) = \sqrt{(2t\cos k + \mu_p)^2 + \Delta_p^2 \sin^2 k}, \quad -\pi < k \leq \pi, \tag{1.14}$$

with the bulk gap closing at $\mu_p = \pm 2t$. Thus, in the parameter regime where $|\mu_p| < 2t$, the system is topological with MZMs at the end.

In the second limit where $\mu_p \neq 0$ and $t = \Delta_p = 0$, the Hamiltonian [Eq. (1.2.1)] becomes $H = -\mu_p \sum_{n=1}^{N} c_n^\dagger c_n$, where the Majoranas pair up at the same lattice site [see Fig. 1.1(b)]. In this limit, the system is topologically trivial with all the excitations having an energy of $\pm|\mu_p|$. The spectrum is gapped with no zero energy

state. So, the system is in the nontopological phase for $|\mu_p| > 2t$.

Since electrons carry a spin degree of freedom, the spinless p-wave pairing potential does not exist intrinsically in natural systems. However, it can be effectively realized in spinful systems by lifting the Kramer's degeneracy of the electrons. This idea has led to numerous proposals for realizing the topological superconductor in various hybrid structures with conventional s-wave superconductors [10, 11, 12, 13, 14, 15, 38, 39, 40, 41, 42, 43, 44, 45, 46, 47]. The most promising way of realizing the topological superconductor is by proximity-inducing superconductivity in a semiconducting nanowire in a magnetic field [11, 13, 14, 15]. In the following subsection, we are going to discuss about this setup in more detail.

1.2.2 Spin-Orbit-Coupled Superconducting Wire

In 2010, Lutchyn *et al.* [13] and Oreg *et al.* [14] made a proposal to realize a 1D topological superconductor by proximitizing a semiconducting nanowire with an s-wave superconductor in the presence of a magnetic field [see Fig. 1.2]. In the continuum limit, the Hamiltonian of this system can be written as

$$H_{\text{SOCSW}} = \int dx \Psi^\dagger \left(-\frac{\hbar^2 \partial_x^2}{2m} - \mu_0 - i\alpha\sigma_y\partial_x + V_Z\sigma_z \right) \Psi + \int dx \left(\Delta_0 \psi_\uparrow \psi_\downarrow + \text{h.c.} \right), \tag{1.15}$$

where $\Psi = \begin{pmatrix} \psi_\uparrow & \psi_\downarrow \end{pmatrix}^T$ is the vector of annihilation operators in spin space, m is the effective mass of electrons, μ_0 is the chemical potential of the nanowire, α is the SOC strength, $V_Z = g\mu_B B$ is the strength of spin splitting due to a magnetic field B which is applied perpendicular to the SOC, Δ_0 is the proximity-induced s-wave

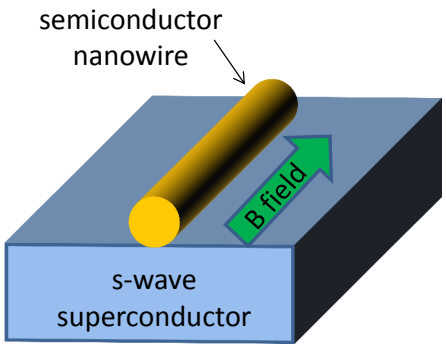

Figure 1.2: Schematic illustration of the SOCSW. A spin-orbit-coupled semiconducting nanowire is placed in proximity to an s-wave superconductor with a magnetic field applied parallel to the wire.

pairing potential, and h.c. denotes Hermitian conjugation.

The physics of this Hamiltonian can be understood by first looking at the energy spectrum of a spin-orbit-coupled Hamiltonian (i.e., Eq. (1.15) with $\Delta_0 = V_Z = 0$). The spin-orbit coupling term shifts the parabolic spectrum of the up and down spin along the positive and negative momentum direction, respectively, as depicted in Fig. 1.3(a). Applying a Zeeman field perpendicular to the SOC direction opens a gap in the spectrum at zero momentum [Fig. 1.3(b,c)]. Placing the chemical potential inside the gap makes the system effectively spinless. If a superconducting term is now induced in the wire, then the system will become a topological superconductor. This corresponds to the topological criterion [13, 14]:

$$|V_Z| > \sqrt{\mu_0^2 + |\Delta_0|^2}. \tag{1.16}$$

In the limit of strong Zeeman field ($V_Z \gg m\alpha^2/\hbar^2, \Delta_0$), the quasiparticle excitation spectrum of the SOCSW is split into two spin bands [see Fig. 1.3(c)].

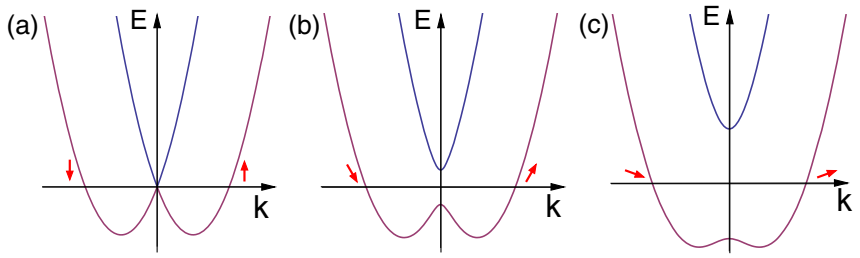

Figure 1.3: Energy spectrum of the SOCSW with different Zeeman field strength V_Z: (a) no Zeeman field, (b) small Zeeman field, and (c) large Zeeman field. Figure is adapted from Ref. [29].

In the normal state ($\Delta_0 = 0$) the spectrum is approximately given by $\epsilon_\pm(k) \approx \frac{\hbar^2 k^2}{2m} \pm |V_Z|$. Projecting the Hamiltonian [Eq. (1.15)] with $\mu_0 = 0$ into the lower occupied band gives the effective Hamiltonian [12, 13, 15]

$$H_{\text{eff}} = \int dx \left[\psi_-^\dagger \left(-\frac{\hbar^2 \partial_x^2}{2m} - |V_Z| \right) \psi_- + \frac{\alpha}{2\,|V_Z|} \left(\Delta_0 \psi_- \partial_x \psi_- + \text{h.c.} \right) \right], \tag{1.17}$$

where $\psi_-(\psi_-^\dagger)$ is the annihilation (creation) field operator for the lower band. This Hamiltonian is the continuum limit of the Kitaev chain Hamiltonian for the topological regime [Eq. (1.7)] with the identifications $\mu_p = |V_Z|$ and $\Delta_p = \alpha\Delta_0/(2|V_Z|)$.

1.3 Signatures of Topological Superconductivity

The simplest and most commonly employed method for detecting the MZM is tunneling spectroscopy. In the following, we give an overview of the conductance spectroscopy of NS [Sec. 1.3.1] and SNS junctions [Sec. 1.3.2] involving topological superconductors. Besides the tunneling spectroscopy, detecting the closing and reopening of the bulk gap as the system goes through the TQPT will also provide a

strong support for the appearance of the MZM in the system. We will review the TQPT in Sec. 1.4.

1.3.1 Zero-Bias Conductance of Normal Metal–Superconductor Junctions

1.3.1.1 Theory

To understand the conductance in an NS junction, let us first learn about how the charge in the normal metal is carried across to the superconductor. An electron incident from the normal metal to the superconductor can be either normal reflected as an electron, Andreev reflected as a hole, or transmitted into the superconductor [see Fig. 1.4]. However, for an incoming electron with energy E less than the superconducting gap Δ, the electron can be either normal reflected as an electron or Andreev reflected as a hole [see Fig. 1.4]. For a normal reflection process, there is no net charge transferred across the junction. However, for the Andreev reflection process, an electron is reflected as a hole, which creates a Cooper pair in the superconductor. This results in a net charge of $2e$ transferred across the junction. The Andreev reflection process can be viewed as a transmission process where the normal lead is separated into the electron and hole lead connected to the left and right side of the superconducting lead (as shown in Fig. 1.5). The differential conductance $G(V) = dI/dV$ is then given by

$$G(V) = 2G_0|r_{eh}(V)|^2, \tag{1.18}$$

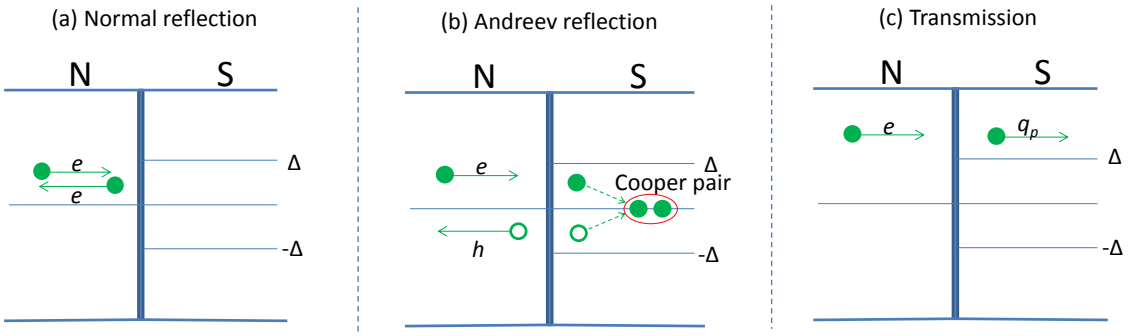

Figure 1.4: Schematic illustration of the scattering processes in an NS junction: (a) normal reflection, (b) Andreev reflection, and (c) quasiparticle transmission.

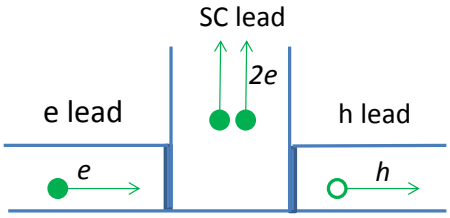

Figure 1.5: Andreev reflection process viewed as a transmisson from an "electron" lead to a "hole" lead.

where $G_0 = e^2/h$ is the conductance quantum and r_{eh} is the probability amplitude of the Andreev reflection process. The factor of 2 is due to the fact there is a net charge of $2e$ transferred by each Andreev reflection process.

The presence of MZMs necessarily changes the conductance value near zero energy, as it can mediate the Andreev reflection processes at zero energy. To see how the MZM changes the conductance value, we first note that the incoming ($\mathcal{J}_{\text{in}}$) and outgoing ($\mathcal{J}_{\text{out}}$) current amplitude is related through the reflection matrix r by

$$\mathcal{J}_{\text{out}} = r(V)\mathcal{J}_{\text{in}}. \tag{1.19}$$

The reflection matrix r is given by

$$r\left(V\right)=\left(\begin{array}{cc} r_{ee} & r_{eh} \\ r_{he} & r_{hh} \end{array}\right) \tag{1.20}$$

where r_{ee} and r_{he} are the normal and Andreev reflection amplitudes of an incoming electron, and r_{hh} and r_{eh} are the normal and Andreev reflection amplitudes of an incoming hole. Since the electron and hole current amplitudes are related by particle-hole symmetry, i.e., $\mathcal{J}_e = \mathcal{P} J_h$, this symmetry imposes the following relation on the reflection matrix

$$\tau_x r^*(-V)\tau_x = r(V), \tag{1.21}$$

and at zero energy we have

$$\tau_x r_0^* \tau_x = r_0, \tag{1.22}$$

where $r_0 \equiv r(V=0)$. Taking the determinant of Eq. (1.22), we have

$$\det r_0 = \det\left(\tau_x r_0^* \tau_x\right) = \det r_0^* = (\det r_0)^*, \tag{1.23}$$

which implies that $\det r_0 = \pm 1$ or

$$Q \equiv |r_{ee}|^2 - |r_{eh}|^2 = \pm 1. \tag{1.24}$$

The quantity Q which is known as the topological invariant quantity has a value of -1 and $+1$ for a topological and nontopological phase, respectively [3, 48]. Since

the electrons or holes cannot be transmitted into the superconductor at zero energy, the reflection matrix must be unitary, i.e., $r^\dagger r = 1$ which implies that

$$|r_{ee}|^2 + |r_{eh}|^2 = |r_{he}|^2 + |r_{hh}|^2 = 1. \tag{1.25}$$

Solving Eqs. (1.24) and (1.25), we have perfect normal reflections ($|r_{ee}| = 1$) for a nontopological phase and perfect Andreev reflections ($|r_{eh}| = 1$) for a topological phase at zero energy. So, the zero-bias conductance value is $2e^2/h$ in the presence of an MZM. We note that this quantized $2e^2/h$ zero-bias conductance value is a robust signature of an MZM which is independent of the details of the junction, e.g., the strength of the potential barrier at the junction interface [33, 34, 35, 36]. This follows from the fact that the above derivation follows only from the unitarity and particle-hole symmetric properties of the reflection matrix. This quantized conductance, however, is not robust against finite temperature [32, 35, 49, 50, 51].

1.3.1.2 Experiment

There has a been a number of experimental attempts to realize MZMs using the nanowire proposal [16, 17, 18, 19, 20, 21, 22, 23, 24]. The pioneering experimental work [16] was done by Kouwenhoven's group at Delft in 2012. In what follows, we will review this pioneering experimental work.

In the Delft experiment [see Fig. 1.6(a)], an InSb nanowire is deposited on the surface of a NbTiN superconductor. A normal (gold) electrode, placed in contact with the end of the nanowire, is used as the probe to measure the current. A tunnel

barrier between the normal lead and nanowire is created by depleting the electron density using a gate at the interface. A magnetic field is applied parallel to the surface of the superconducting surface.

Fig. 1.6(b) shows the differential conductance profile as the magnetic field is varied. We can see the appearance of zero-bias conductance peaks (ZBCPs) as the magnetic field is raised above a certain critical value. This provides a suggestive evidence for the appearance of MZMs in the system. Another piece of evidence for the Majorana physics is provided in Fig. 1.6(c,d), where the differential conductance is measured as the magnetic field direction is varied. Fig. 1.6(c) shows the differential conductance for the case when the magnetic field is applied along the surface of the substrate. When the magnetic field is applied parallel to the SOC direction, which corresponds to angle $= \frac{\pi}{2}, \frac{3\pi}{2}$ [see Fig. 1.6(c)], there is no ZBCP. The ZBCP becomes the most pronounced for angles $= 0$ and π, which corresponds to magnetic fields perpendicular to the SOC direction. For the case when the magnetic field is perpendicular to the substrate, the ZBCP is present for all angles.

Another feature of the conductance profile that is worth mentioning here is the "soft gap" feature, which refers to the finite conductances for voltages inside the superconducting gap [see Fig. 1.6(b)]. In Fig. 1.6(b), the superconducting gap is indicated by the green arrows. Since the topological protection of the MZMs is governed by the superconducting gap, it is essential to have a "hard gap", i.e., no subgap states in the conductance profile. Recent experiments [22, 23] have managed to obtain a harder gap in the conductance profile by having a better interfacial contact between the nanowire and superconductor.

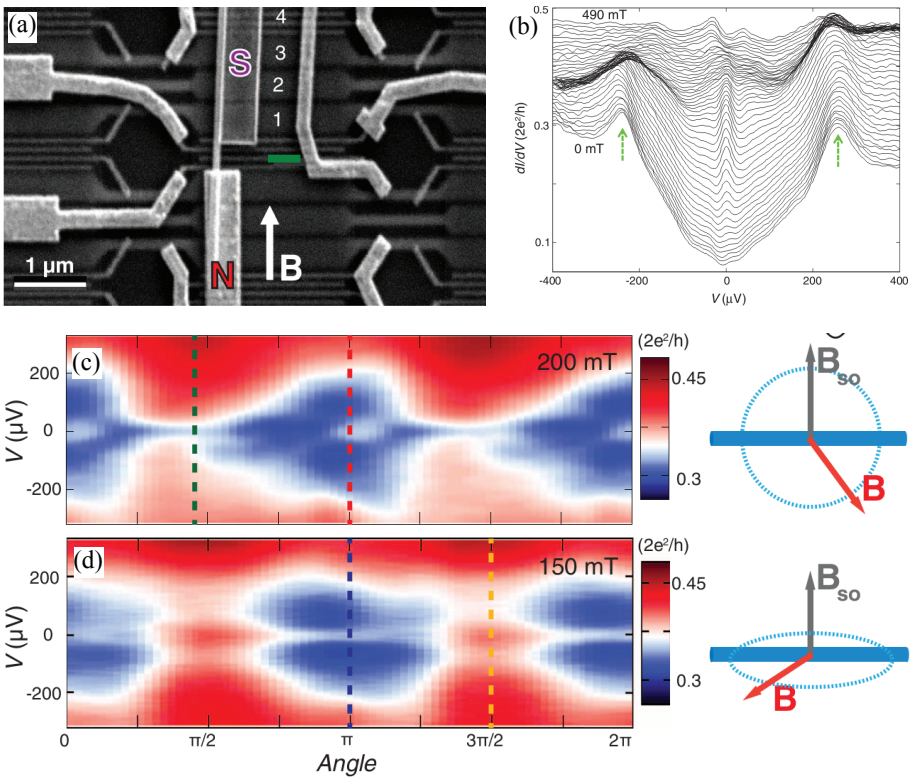

Figure 1.6: The Delft experiment on the semiconductor-superconductor heterostructure. (a) The scanning electron microscope image of the setup. A semiconducting InSb nanowire is placed in contact with normal (N) and superconducting (S) electrodes. A gate (colored green) is used to create a tunnel barrier in between the N and S electrodes. The wire's chemical potential is adjusted by varying the voltages of the gates numbered 1-4. (b) Differential conductance (dI/dV) versus bias voltage (V) for different magnetic fields strength ranging from 0 to 490 mT (in steps of 10 mT). The traces are offset for clarity, except the lowest trace (at zero magnetic field). (c) dI/dV versus V and the angle of the magnetic field, where Angle=$0, \pi$ corresponds to magnetic fields perpendicular to the SOC direction, and Angle=$\frac{\pi}{2}, \frac{3\pi}{2}$ corresponds to magnetic fields parallel to the SOC direction. (d) dI/dV versus V and the angle of the magnetic field, where the magnetic field is always perpendicular to the SOC direction. Figure is adapted from Ref. [16].

The ZBCPs measured in all of the nanowire experiments, however, are only about $0.1e^2/h$, which are significantly less than the canonical quantized value of $2e^2/h$. This deviation can be attributed partly to the thermal broadening in the normal-metal lead, which reduces the zero-bias conductance value and broadens its peak. To mitigate the effect of thermal broadening, one can use a superconducting lead instead of a normal lead in probing the MZM tunneling conductance. In a superconducting lead, the quasiparticle excitation is exponentially suppressed by the superconducting gap, i.e., $\exp(-\Delta_{\text{lead}}/T)$, which in turn suppresses the thermal broadening effect. In the following, we will look at the signature of MZMs in the conductance spectrum of an SNS junction.

1.3.2 Gap-Bias Conductance in SNS Junctions

1.3.2.1 Theory

In this subsection, we will investigate the signature of MZM in an SNS junction [See Fig. 1.7(a)]. For a conventional SNS junction without any subgap states, the conductance in the weak-tunneling limit (small junction transparency) develops two peaks at $eV = \pm 2\Delta_{\text{lead}}$ as shown in Fig. 1.7(b). These peaks arise due to direct tunneling of electrons from the occupied band of one superconductor to the empty band of the other superconductor [see Fig. 1.7(c)]. For SNS junctions with a zero energy state, e.g., MZM, there are two tunneling conductance peaks in the differential conductance (dI/dV) due to single Andreev reflections from the MZM [see Fig. 1.7(d)]. These peaks occur at the gap-bias voltages $eV = \pm\Delta_{\text{lead}}$

[see Fig. 1.7(b)], i.e., when the gap singularity of the probe lead aligns with the zero-energy state. In the case where the probe lead has a Bardeen-Cooper-Schrieffer (BCS) singularity and the zero-energy mode is an MZM, Peng *et al.* [52] found that the gap-bias conductance is quantized at

$$G_M = (4-\pi)\frac{2e^2}{h}. \tag{1.26}$$

Following Ref. [53], below we will give the derivation for the MZM quantized conductance value given in Eq. (1.26). To this end, let us first note that the current due to single Andreev reflection is given by

$$I = \frac{1}{2}2e\int \frac{dE}{2\pi\hbar}|A_{he}|^2[n_F(E-eV) - n_F(E+eV)], \tag{1.27}$$

where the charge 2e accounts for the fact that each Andreev reflection gives rise to a Cooper pair, $|A_{he}|$ is the probability of Andreev reflection, and the term $\mp eV$ in the Fermi function $n_F(E \mp eV)$ accounts for the fact that the electron and hole energies are shifted by eV relative to the Fermi energy. Since in the weak-tunneling limit, the probability of Andreev reflection is [54]

$$|A_{he}| = \frac{\Gamma_e\Gamma_h}{E^2 + \frac{1}{4}(\Gamma_e+\Gamma_h)^2}, \tag{1.28}$$

the current is then given by

$$I = e \int \frac{dE}{2\pi\hbar} \frac{\Gamma_e \Gamma_h}{E^2 + \frac{1}{4}(\Gamma_e + \Gamma_h)^2} [n_F(E - eV) - n_F(E + eV)]. \tag{1.29}$$

where the electron and hole tunneling rate Γ_e and Γ_h are proportional to the density of states in the lead. For a superconducting lead, $\Gamma_{e/h} = \tilde{\Gamma}_{e/h} \rho(E \mp eV)$ where $\tilde{\Gamma}_e = \tilde{\Gamma}_h = \Gamma$ for superconducting lead with a BCS singularity (i.e. $\sum_{\sigma=\uparrow,\downarrow} |u_\sigma|^2 = \sum_{\sigma=\uparrow,\downarrow} |v_\sigma|^2$ with u and v being the electron and hole component of the BdG superconducting wavefunction at the gap edge). The BCS density of states normalized by the normal-state density is given by $\rho(E) = \Theta(|E| - \Delta_{\text{lead}})|E|/\sqrt{E^2 - \Delta_{\text{lead}}^2}$.

For the voltages near the superconducting gap $eV \simeq \Delta_{\text{lead}}$, $n_F(E - eV) - n_F(E + eV) \simeq 1$ up to small corrections of the order of $\exp(-\Delta_{\text{lead}})/T$ which reflects the temperature insensitivity of the current measured using a superconducting lead. The current for these voltages is then given by

$$I = e \int_{-(eV - \Delta_{\text{lead}})}^{eV - \Delta_{\text{lead}}} \frac{dE}{2\pi\hbar} \frac{\Gamma^2 \rho(E - eV)\rho(E + eV)}{E^2 + \frac{1}{4}\Gamma^2 [\rho(E - eV) + \rho(E + eV)]^2}. \tag{1.30}$$

For small temperatures, the current is zero for $eV < \Delta_{\text{lead}}$. At the gap-bias voltage $\eta = eV - \Delta_{\text{lead}} \simeq 0$, the zero-energy bound state is aligned with the BCS singularity. For $|E| < \eta$, we have

$$\rho(E \pm eV) \simeq \sqrt{\Delta_{\text{lead}}/2(\eta \pm E)} \gg 1, \tag{1.31}$$

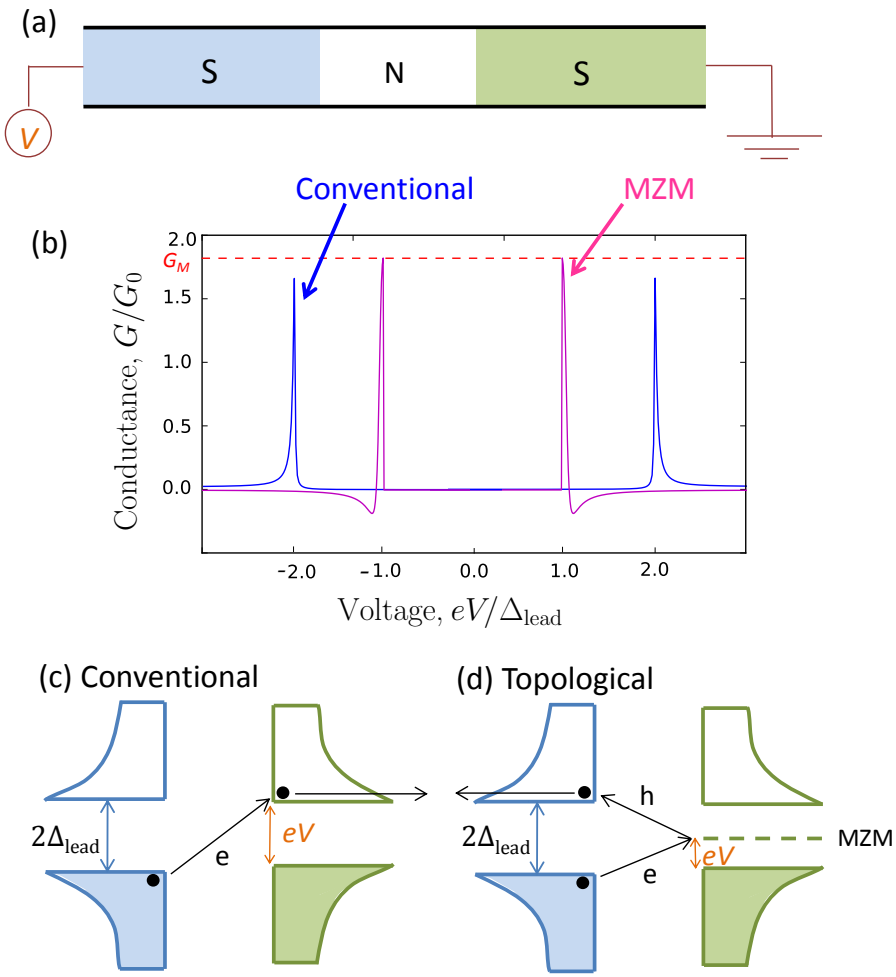

Figure 1.7: (a) Schematic illustration of a voltage-biased superconductor–normal-metal–superconductor (SNS) junction. (b) Tunneling peaks of a conventional and topological SNS junction. (c) Direct tunneling of electrons from the occupied band to the empty band. (d) Single Andreev reflection from MZM.

.

and the current becomes

$$I = \frac{4e}{h}\int_{-\eta}^{\eta} \frac{dE}{\sqrt{\eta^2 - E^2}} \frac{\omega_t^3}{E^2 + \omega_t^3 \left(\frac{1}{\sqrt{\eta - E}} + \frac{1}{\sqrt{\eta + E}}\right)^2}, \tag{1.32}$$

where the effective tunneling coupling $\omega_t = \frac{1}{2}(\Delta_{\text{lead}}\Gamma^2)^{1/3}$. Rescaling the integrand in Eq. (1.32), we have

$$I = \frac{4e}{h}\int_{-1}^{1} \frac{dx}{\sqrt{1 - x^2}} \frac{1}{x^2 \left(\frac{\eta}{\omega_t}\right)^3 + \left(\frac{1}{\sqrt{1-x}} + \frac{1}{\sqrt{1+x}}\right)^2} \tag{1.33}$$

for $\eta > 0$, with the limiting value

$$\frac{dI}{dV} = \begin{cases} 0, & \text{for } e|V| - \Delta_{\text{lead}} < 0 \\ \frac{2e^2}{h}(4 - \pi), & \text{for } e|V| - \Delta_{\text{lead}} = 0 \\ -\frac{2e^2}{h}\frac{\omega_t^3}{(e|V| - \Delta_{\text{lead}})^3} \times \text{const}, & \text{for } e|V| - \Delta_{\text{lead}} \gg \omega_t. \end{cases} \tag{1.34}$$

So, the conductance develops a step jump from 0 to $(4 - \pi)\frac{2e^2}{h}$ at $e|V| = \Delta_{\text{lead}}$.

1.3.2.2 Experiment

Besides the nanowire setup, chains of ferromagnetic atoms deposited on the surface of conventional s-wave superconductors [see Fig. 1.8] can also be utilized to realize the Kitaev chain and thereby realizing the MZMs [47, 46, 45, 44]. The first conductance measurement by Yazdani's group using a normal Scanning Tunneling Microscope (STM) tip on chains of Fe atoms on top of the Pb superconducting

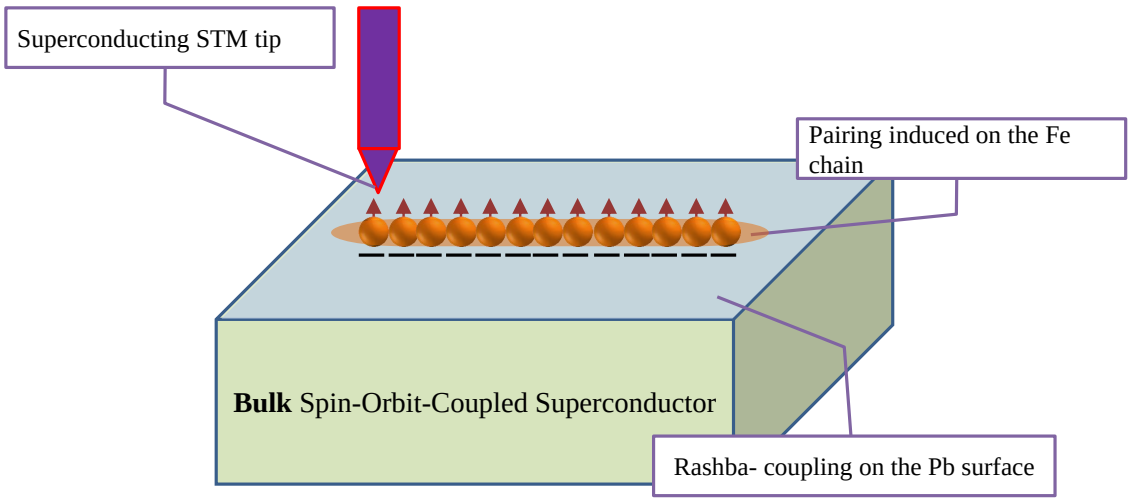

Figure 1.8: (a) Schematic illustration of chains of ferromagnetic Fe atoms deposited on a superconducting Pb surface. The conductance of the system is measured using an STM tip.

substrate showed the ZBCP localized at the end of the Fe atomic chain [55]. Recent experiment by the same group using a superconducting STM tip [see Fig. 1.9] shows gap-bias conductance peaks at the end of the Fe atomic chain [56]. These two measurements are suggestive indications of the existence of MZMs in this system, although the peak values measured are less than the canonical quantized values.

1.4 Gap Closing and Topological Quantum Phase Transition

Two phases are *topologically equivalent* if the Hamiltonians of the system can be continuously tranformed into one another. The TQPT is a quantum phase transition between two topologically inequivalent phases which is accompanied by a bulk gap closing. For a 1D superconducting Hamiltonian as discussed in this thesis, a TQPT is always accompanied by a zero-momentum gap closing. Therefore, de-

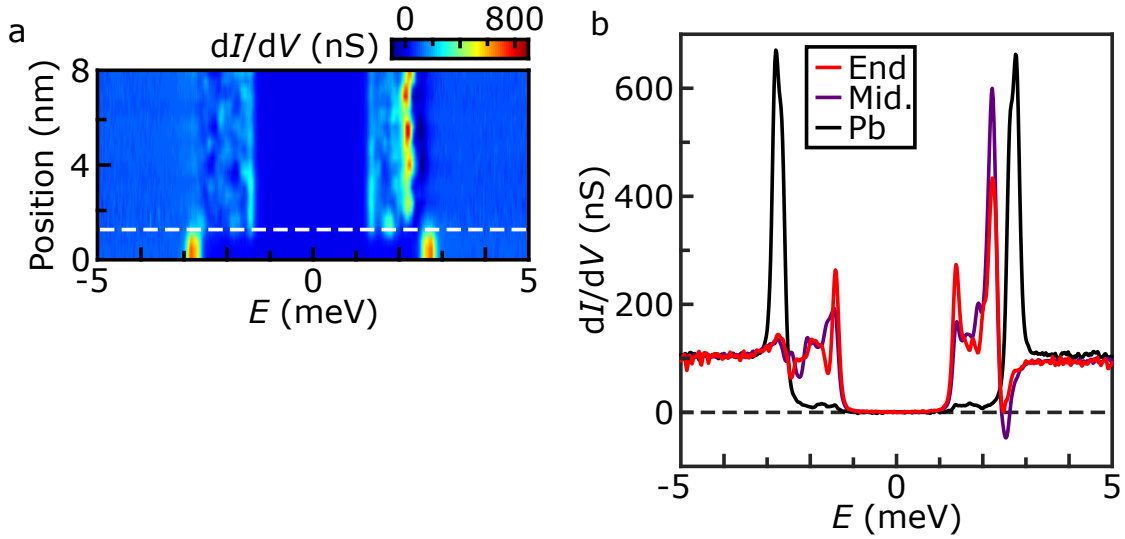

Figure 1.9: (a) Differential conductance measured along the Fe chain where the white dashed line denotes the chain end. Note the appearance of a conductance peak at the chain end at $e|V| = \Delta_{\text{lead}}$. (b) The conductance measured at the bare Pb surface (black) and at the end (red) and middle (purple) of the Fe atomic chain.

tecting the zero-momentum gap closing would provide a probe for the TQPT. In Chapter 4, we will discuss a dynamical scheme to detect the TQPT in ultracold atomic systems.

1.5 Outline of the Thesis

In this thesis, we investigate in detail several signatures of topological superconductivity. In Chapter 2, we study the transport properties of 1D NS junctions with topological superconductors across their topological transitions. Working within the Blonder-Tinkham-Klapwijk (BTK) formalism generalized for topological NS junctions, we analytically calculate the differential conductance for tunneling into two models of a topological superconductor: a spinless p-wave superconductor and a spin-orbit-coupled s-wave superconducting wire in a Zeeman field. It is

gratifying that our analytical model not only captures the MZM zero-bias conductance quantization and experimental soft-gap feature, but also yields an interesting prediction that despite being quantized in the topological regime, the zero-bias conductance only develops as a peak in the conductance spectra for sufficiently small junction transparencies, or for small and large spin-orbit coupling strength. The work in this chapter has led to the publication of Ref. [36].

In Chapter 3, we study the transport of various voltage-biased 1D SNS junctions with arbitrary junction transparency where the superconductor can be either nontopological or topological. We provide a comprehensive analysis of the zero-temperature dc current I and differential conductance dI/dV of the SNS junctions *with* or *without* the MZMs. We verify that in the tunneling limit (small junction transparencies), where only single Andreev reflections contribute to the current, the conductance for voltages below the s-wave superconducting lead gap Δ_s is zero, and there are two symmetric conductance peaks appearing at $eV = \pm\Delta_s$ with the quantized value $(4-\pi)2e^2/h$ due to resonant Andreev reflection from the MZM. However, when the junction transparency is not small, there is a finite conductance for $e|V| < \Delta_s$ arising from multiple Andreev reflections. The conductance at $eV = \pm\Delta_s$ in this case is no longer quantized. We further show that the MZM conductance peak probed using a superconducting lead without a BCS singularity has a non-universal value which decreases with decreasing junction transparency. In general, the conductance is particle-hole asymmetric except for sufficiently small transparencies. Moreover, we show that, for certain values of parameters, the tunneling conductance from a zero-energy conventional Andreev bound state (ABS)

can be made to mimic the conductance from a true Majorana mode. The work in this chapter has led to the publication of Refs. [57, 58].

In Chapter 4, we demonstrate that dynamical probes provide direct means of detecting the TQPT between conventional and topological phases. We propose a quench protocol which is particularly suited to study the short-lived topological phases in the ultracold atomic settings. Our protocol mitigates the heating effects due to spontaneous emission from off-resonantly excited atoms by preparing the systems in its long-lived non-topological phases and driving them into the topological phases and back. We apply this strategy to study the TQPT into a Majorana-carrying topological phase predicted in 1D spin-orbit-coupled Fermi gases (SOCFGs) with attractive interactions. The resulting spin-resolved momentum distribution, computed by self-consistently solving the time-dependent BdG equations, exhibits Kibble-Zurek (KZ) scaling and Stückelberg oscillations characteristic of the TQPT. We discuss parameter regimes where the TQPT is experimentally accessible. The work in this chapter has led to the publication of Ref. [59].

In Chapter 5 we present our conclusions and discuss the implication of our work for future experiments.

Chapter 2

Conductance Spectroscopy of Normal Metal–Topological Superconductor Junctions

A key signature of the MZMs is the quantized value $2e^2/h$ of the zero-bias differential conductance for the normal metal–topological superconductor junction. This quantized conductance, associated with perfect Andreev reflection, indicates the presence of a single localized MZM at the end of the topological superconductor [32, 33, 34, 35]. For a sufficiently high tunnel barrier, the conductance spectra have a zero-bias peak at $2e^2/h$. While experimental results clearly show the development of such a peak upon tuning the system, at a finite magnetic field, into the predicted topological regime, the value of the ZBCP is much less than the expected quantized value [16, 18, 19, 20, 21, 22, 23, 24].

The difficulty in interpreting the tunneling experiments has prompted numerous theoretical studies on the conductance of the nanowire-superconductor heterostructure, using both numerical [49, 60, 61, 62] and analytical techniques [63, 64]. Although the latter works consider highly idealized models of the system, they are nevertheless valuable as they give clear insight into the parametric dependence of the transport physics as well as its dependence on various physical properties of the experimental setup, which can then be applied to understand the more complicated

numerical studies. An important question concerns the change in the conductance as the system is tuned from the topologically trivial to the nontrivial regimes (e.g., by tuning the applied magnetic field in semiconductor-superconductor hybrid structures). Remarkably, this aspect of the physics has attracted relatively little attention using these analytic methods [64].

In this chapter we examine the conductance spectra of 1D NS junctions involving topological superconductors across their topological transition. We utilize the BTK formalism [65], which is commonly employed to study junctions with unconventional superconductors [66], to obtain analytic results for the tunneling conductance of two models of a topological superconductor junction: a junction between a spinless normal metal and a p-wave superconductor, and a junction between a spinful normal metal and a spin-orbit-coupled s-wave superconductor in a magnetic field. We note that the spinless p-wave superconductor can be regarded as an effective low-energy theory for the semiconductor nanowire, but this is inadequate for understanding the conductance spectroscopy of the device. Our analysis is analytical, and in particular we give explicit expressions for the zero-bias tunneling conductance at zero temperature, which clearly shows an abrupt change at the topological transition. Specifically, we find that in the topological regime, the zero-temperature zero-bias conductance is quantized at a value of $2e^2/h$ independent of the barrier strength Z, but the detailed structure (e.g., the width and the shape) of the quantized ZBCP is controlled by the barrier transparency and the magnitude of spin-orbit coupling. Our BTK theory for the topological NS junction also shows that a finite barrier transparency could lead to the experimentally observed soft gap which is

ubiquitous in semiconductor nanowire tunneling experiments [16, 19, 20, 21]. This chapter is based on Ref. [36] and the figures in this chapter are adapted from the same reference.

2.1 Normal Metal–Spinless *p*-wave Superconductor Junction

We begin by considering a 1D junction between a spinless normal metal (NM) and a spinless p-wave superconductor (pSC), which are located at $x \leq 0$ and $x \geq 0$, respectively [see Fig. 2.1]. Similar to the BTK model, here we model the potential barrier at the interface by a δ-function barrier of strength Z. The parameter Z controls the barrier transparency at the NS interface, and is the key parameter in the theory quantifying the tunneling conductance properties at the junction where a low (high) value of Z corresponds to a barrier with high (low) transparency at the NS interface. A microscopic evaluation of Z is typically difficult since the microscopic details of the junction are generally unknown, and so Z is treated as a free fitting parameter. The Hamiltonian in each region is written

$$H_j(x) = \frac{1}{2}\int dx \Psi_j^\dagger(x)\mathcal{H}_j(x)\Psi_j(x), \tag{2.1}$$

where $\Psi_j(x) = (\psi_j^\dagger(x), \psi_j(x))^{\mathrm{T}}$ are Nambu spinors and $\psi_j^\dagger(x)$ ($\psi_j(x)$) is the creation (annihilation) field operator in region $j = N$ (NM) and p (pSC). Assuming that the effective mass of the electron m is uniform throughout the system, the Bogoliubov-de

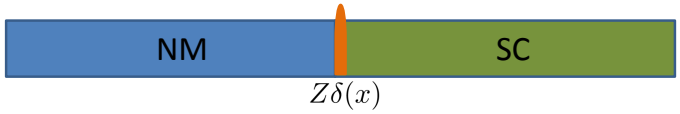

Figure 2.1: Schematic illustration of an NS junction with a delta-function barrier of strength Z.

Gennes (BdG) Hamiltonians are

$$\mathcal{H}_N(x) = \left(-\frac{\hbar^2\partial_x^2}{2m} - \mu_N\right)\tau_z, \tag{2.2a}$$

$$\mathcal{H}_p(x) = \left(-\frac{\hbar^2\partial_x^2}{2m} - \mu_p\right)\tau_z - i\Delta_p\partial_x\tau_x, \tag{2.2b}$$

where μ_N (μ_p) is the chemical potential of the NM (pSC), $\Delta_p \geq 0$ is the p-wave pairing potential, and $\tau_{x,y,z}$ are the Pauli matrices acting in the particle-hole space.

For notational simplicity, in the rest of this chapter we will work with units such that $\hbar$, μ_N, and $2m$ are all equal to unity. The energy spectra of the NM and pSC can be obtained by diagonalizing the BdG Hamiltonian in Eq. (2.2) and they are given by

$$\epsilon_{N,\pm}(k) = \pm(k^2 - 1) \tag{2.3a}$$

$$\epsilon_{p,\pm}(k) = \pm\sqrt{(k^2 - \mu_p)^2 + (\Delta_p k)^2}. \tag{2.3b}$$

The energy spectra of the pSC are plotted for different values of μ_p in Fig. 2.2. Note that the spectrum becomes gapless at $\mu_p = 0$ which marks the topological transition [4] between BCS-like weak pairing phase ($\mu_p > 0$) and the BEC-like strong pairing phase ($\mu_p < 0$) . In the former case, the positive energy spectrum

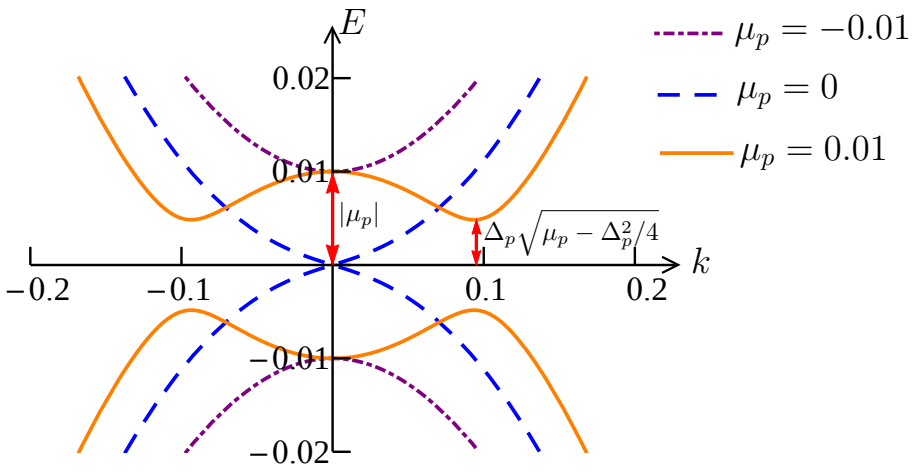

Figure 2.2: Typical energy spectra of the spinless pSC illustrating the nontopological ($\mu_p = -0.01$), transition ($\mu_p = 0$) and topological regimes ($\mu_p = 0.01$). For all curves we set $\Delta_p = 0.05$.

only develops the characteristic "double-well" BCS structure for $\mu_p > \Delta_p^2/2$, with minimum value $E_1 = \Delta_p\sqrt{\mu_p - \Delta_p^2/4}$ at $k = \pm\sqrt{\mu_p - \Delta_p^2/2}$, and a local maximum value $E_2 = \mu_p$ at $k = 0$.

We consider the scattering of an electron incoming from the NM into the pSC with energy E. The incident electron can be normal reflected as an electron, Andreev reflected as a hole, or transmitted into the pSC [see Fig. 2.3]. The scattering wave function is $\Phi(x) = \Phi_N(x)\Theta(-x) + \Phi_p(x)\Theta(x)$, where $\Theta(x)$ is the Heaviside step function and

$$\Phi_N(x) = \begin{pmatrix} 1 \\ a \end{pmatrix} e^{ix} + \begin{pmatrix} b \\ 0 \end{pmatrix} e^{-ix}, \tag{2.4a}$$

$$\Phi_p(x) = c \begin{pmatrix} \gamma_- \\ 1 \end{pmatrix} e^{ik_- x} + d \begin{pmatrix} \gamma_+ \\ 1 \end{pmatrix} e^{ik_+ x}, \tag{2.4b}$$

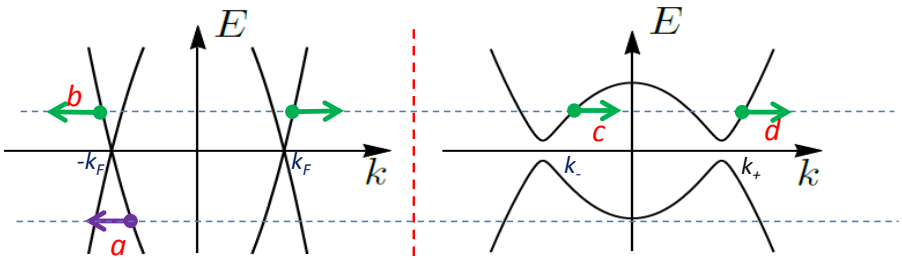

Figure 2.3: Schematic diagram of the scattering processes in an NS junction. The green circles denote electron and the purple circles denote holes. An incoming electron from the normal metal side can undergo Andreev reflection with amplitude a, normal reflection with amplitude b or transmission into the superconductors with amplitude c and d.

where a and b are the Andreev and normal reflection amplitudes, respectively, c and d are the quasiparticle transmission coefficients into the pSC, and

$$\gamma_{\pm} = \frac{E + k_{\pm}^2 - \mu_p}{\Delta_p k_{\pm}}. \tag{2.5}$$

Note that we approximate the wave vector of the electrons and holes in the NM by the Fermi momentum $k_F = \sqrt{2m\mu_N}/\hbar$, valid for $E \ll 1$. The momenta $k_{\pm}$ of the pSC wave function can be obtained by solving the following equation

$$E^2 = (k^2 - \mu_p)^2 + (\Delta_p k)^2 \,. \tag{2.6}$$

Depending on the energy E of the incoming electron and the chemical potential μ_p, the wave function in the pSC can either be evanescent with complex solutions of Eq. (2.6), or a propagating state corresponding to a real solution of Eq. (2.6) with positive group velocity. The solutions of Eq. (2.6) are grouped in Table 2.1.

μ_p	E	k_-, k_+
$\mu_p \leq \Delta_p^2/4$	$0 \leq E \leq E_2$ $E \geq E_2$	k_{I-}, k_{I+} k_{I+}, k_{R+}
$\Delta_p^2/4 \leq \mu_p \leq \Delta_p^2/2$	$0 \leq E \leq E_1$ $E_1 \leq E \leq E_2$ $E \geq E_2$	k_{C-}, k_{C+} k_{I-}, k_{I+} k_{I+}, k_{R+}
$\mu_p \geq \Delta_p^2/2$	$0 \leq E \leq E_1$ $E_1 \leq E \leq E_2$ $E \geq E_2$	k_{C-}, k_{C+} k_{R-}, k_{R+} k_{I+}, k_{R+}

Table 2.1: Various solutions of Eq. (2.6) for different values of chemical potential μ_p and energy E, where $E_1 = \Delta_p\sqrt{\mu_p - \Delta_p^2/4}$ and $E_2 = |\mu_p|$. The momentum of the propagating modes are denoted by $k_{R\pm}$, while that of evanescent modes are given by $k_{I\pm}$ and $k_{C\pm}$. They are given by $k_{R\pm} = \pm[(\mu_p - \Delta_p^2/2) \pm \sqrt{E^2 - E_1^2}]^{1/2}$, $k_{I\pm} = i[(\Delta_p^2/2 - \mu_p) \pm \sqrt{E^2 - E_1^2}]^{1/2}$ and $k_{C\pm} = \pm[(\mu_p - \Delta_p^2/2) \pm i\sqrt{E_1^2 - E^2}]^{1/2}$.

The wave functions satisfy the continuity and current conservation equations:

$$\Phi_p(x)|_{x=0^+} = \Phi_N(x)|_{x=0^-},$$

$$J_p\Phi_p(x)|_{x=0^+} - J_N\Phi_N(x)|_{x=0^-} = -2iZ\tau_z\Phi_N(0) \tag{2.7}$$

where the current operators are given by

$$J_N = -2i\partial_x\tau_z, \tag{2.8a}$$

$$J_p = -2i\partial_x\tau_z + \Delta_p\tau_x. \tag{2.8b}$$

Solving the boundary conditions, we obtain the Andreev ($a(E)$) and normal reflec-

tion coefficients ($b(E)$) as

$$a(E) = \frac{\Delta_p(\gamma_+ - \gamma_-) - 2(k_+ - k_-)}{\mathcal{D}_E}, \quad \text{and} \tag{2.9a}$$

$$b(E) = \frac{(2 - 2iZ - k_+ - k_- - \Omega)(\gamma_- - \gamma_+) + \frac{\Delta_p}{2}(k_+ - k_-)(\gamma_+\gamma_- + 1)}{\mathcal{D}_E}, \tag{2.9b}$$

where

$$\Omega = 1 + (Z - ik_-)(Z - ik_+) - \frac{\Delta_p^2}{4}, \tag{2.10a}$$

$$\mathcal{D}_E = \Omega(\gamma_- - \gamma_+) - \frac{\Delta_p}{2}(k_+ - k_-)(\gamma_+\gamma_- + 1) - (k_+ - k_-)(\gamma_- + \gamma_+). \tag{2.10b}$$

Within the BTK formalism [65] the zero-temperature differential conductance is given by

$$G_p(E) = G_0 \left(1 + |a(E)|^2 - |b(E)|^2\right), \tag{2.11}$$

where $G_0 = e^2/h$ is the conductance quantum. Although the general form of $G_p(E)$ is lengthy and unenlightening, relatively simple expressions can be found for the physically interesting case of zero bias, i.e., $E = 0$, which is provided in Table 2.2 for the three different regimes of μ_p. In particular, the zero-bias conductance displays a jump from $G_p(0) = 0$ in the trivial regime ($\mu_p < 0$) to $G_p(0) = 2$ in the topological regime ($\mu_p > 0$). The quantized conductance is characteristic of the topological state, and indicates perfect Andreev reflection [i.e., $|a(0)|^2 = 1$, and $|b(0)|^2 = 0$] at an interface supporting a Majorana mode [33, 34]. It is robust against the junction details, e.g., the barrier strength Z and p-wave pairing potential Δ_p.

At the transition point ($\mu_p = 0$) we find $G_p(0) \leq G_0$, where the exact conductance value is determined by Z and Δ_p.

	$\mu_p < 0$	$\mu_p = 0$	$\mu_p > 0$
$a(0)$	0	$-\dfrac{i\Delta_p}{(Z+\Delta_p/2)^2+1+\Delta_p}$	$-i$
$b(0)$	$-e^{i\varphi}$	$-\dfrac{(Z+\Delta_p/2)^2+1}{(Z+\Delta_p/2)^2+1+\Delta_p}e^{i\varphi}$	0
$\dfrac{G_p(0)}{G_0}$	0	$1-\dfrac{[(Z+\Delta_p/2)^2+1]^2-\Delta_p^2}{[(Z+\Delta_p/2)^2+1+\Delta_p]^2}$	2

Table 2.2: Explicit expressions for the zero-bias Andreev reflection coefficient $a(0)$, normal reflection coefficient $b(0)$, and differential conductance $G_p(0)$ for the spinless NM-pSC junction. The results are grouped into the three different regimes of μ_p: the nontopological phase ($\mu_p < 0$), the topological phase transition point ($\mu_p = 0$), and the topological phase ($\mu_p > 0$). The quantity φ is defined by $\sin\varphi = 2(Z + \sqrt{\Delta_p^2/4 - \mu_p})/[(Z + \sqrt{\Delta_p^2/4 - \mu_p})^2 + 1]$.

The conductance as a function of the energy is plotted in Figs. 2.4 and 2.5. In general, the tunneling conductance $G_p(E)$ decreases with increasing barrier strength Z, although in the topological regime the zero-bias conductance is robust against Z. Furthermore, it is interesting to note that in the topological regime, the width of the zero-bias peak decreases with Z but displays a nonmonotonic behavior with Δ_p: the width first increases as Δ_p increases, until a certain value of Δ_p, after which it decreases with increasing Δ_p. For $\mu_p \leq \Delta_p^2/2$, a singularity appears in the $G_p(E)$ curve at the gap edge $E_2 = |\mu_p|$. On the other hand, as shown in Fig. 2.5(a), two singularities are found in the conductance for $\mu_p > \Delta_p^2/2$, corresponding to the gap edge at $E_1 = \Delta_p\sqrt{\mu_p - \Delta_p^2/4}$ and the Van Hove singularity at $E_2 = \mu_p$.

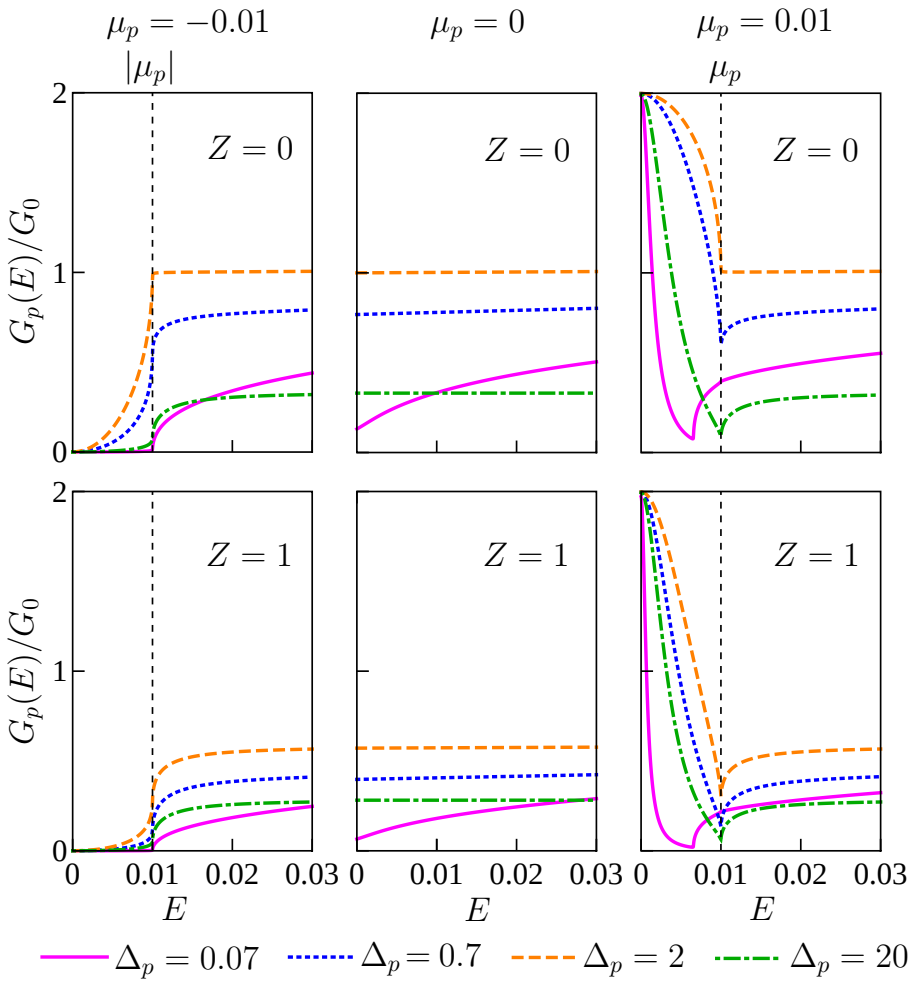

Figure 2.4: Plots of the tunneling conductance $G_p(E)$ with different pairing potential Δ_p and chemical potential μ_p for the spinless NM-pSC junction. We show typical results for the nontopological ($\mu_p < 0$, left column), transition ($\mu_p = 0$, middle column), and topological ($\mu_p > 0$, right column) regimes, and for barrier strength $Z = 0$ (top row) and $Z = 1$ (bottom row). The pairing potential values Δ_p are expressed in units of μ_N/k_F, while the chemical potential μ_p and energy E are given in units of μ_N.

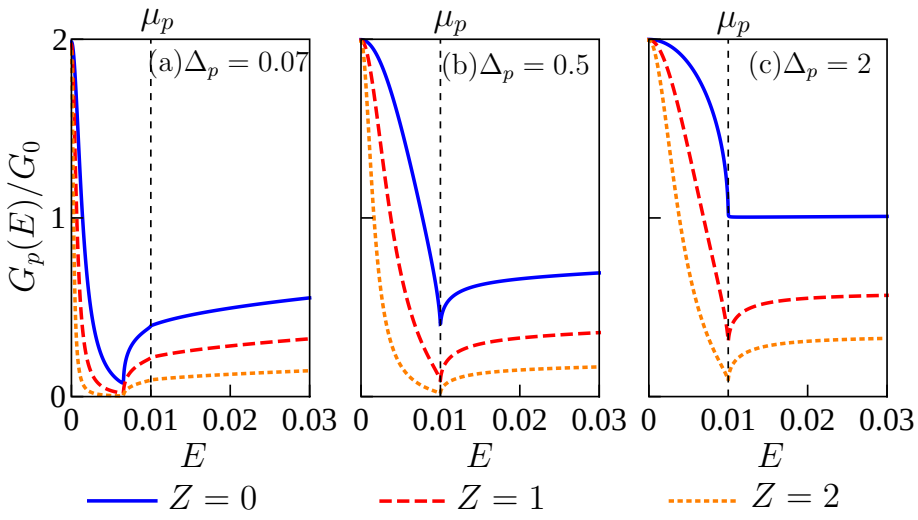

Figure 2.5: Plots of the tunneling conductance $G_p(E)$ with different barrier strength Z and the pairing potential Δ_p for the spinless NM-pSC junction in the topological regime. The pairing potential values Δ_p are expressed in units of μ_N/k_F while the chemical potential μ_p and energy E are given in units of μ_N. Note that the zero-bias conductance is quantized at $2G_0$ independent of the the junction details.

2.2 Normal Metal–Spin-Orbit-Coupled Superconducting Nanowire Junction

In this section we consider a 1D junction between a spinful normal metal (NM) and a spin-split spin-orbit-coupled superconducting wire (SOCSW) , which occupy the regions $x \leq 0$ and $x \geq 0$, respectively. Similar to Sec. 2.1, we model their interface at $x = 0$ by a δ-potential barrier of strength Z. The Hamiltonian in each region is written as

$$H_j(x) = \frac{1}{2}\int dx \overline{\Psi}_j^\dagger(x)\mathcal{H}_j\overline{\Psi}_j(x), \tag{2.12}$$

where

$$\overline{\Psi}_j(x) = (\psi_{j\uparrow}(x), \psi_{j\downarrow}(x), \psi_{j\downarrow}^\dagger(x), -\psi_{j\uparrow}^\dagger(x))^{\mathrm{T}}, \tag{2.13}$$

and $\psi^\dagger_{j\sigma}(x)$ $[\psi_{j\sigma}(x)]$ is the creation (annihilation) field operator of an electron with spin σ in region $j = N$ (NM) or S (SOCSW). Using the same unit convention as in the previous section, we write the BdG Hamiltonians of the NM and SOCSW as

$$\mathcal{H}_N = \left(-\partial_x^2 - 1\right)\tau_z, \tag{2.14a}$$

$$\mathcal{H}_S = -\partial_x^2\tau_z - i\alpha\partial_x\tau_z\sigma_z + V_Z\sigma_x + \Delta_0\tau_x, \tag{2.14b}$$

where $\sigma_{x,y,z}$ $(\tau_{x,y,z})$ are the Pauli matrices in spin (particle-hole) space, α is the strength of SOC, V_Z is the Zeeman field, and $\Delta_0 \geq 0$ is the proximity-induced s-wave pairing potential which is assumed to be real. We set the chemical potential of the SOCSW to be zero, and take uniform electron masses throughout the system.

The positive branches of the BdG spectrum of the SOCSW are given by

$$E_\pm = \left(k^4 + \alpha^2k^2 + \Delta_0^2 + V_Z^2 \pm 2\sqrt{k^4(\alpha^2k^2 + V_Z^2) + \Delta_0^2V_Z^2}\right)^{1/2}. \tag{2.15}$$

As shown in Fig. 2.6, the energy spectrum is gapped except for $V_Z = \Delta_0$. This value of V_Z marks the TQPT between the topologically trivial ($V_Z < \Delta_0$) and nontrivial phases ($V_Z > \Delta_0$) [11, 12, 13, 14]. Although Eq. (2.15) can be analytically solved for the momenta corresponding to a given energy E, the general expression is unwieldy. In what follows, therefore, we will instead work in the limits of a strong Zeeman field and strong SOC, where more compact results can be obtained.

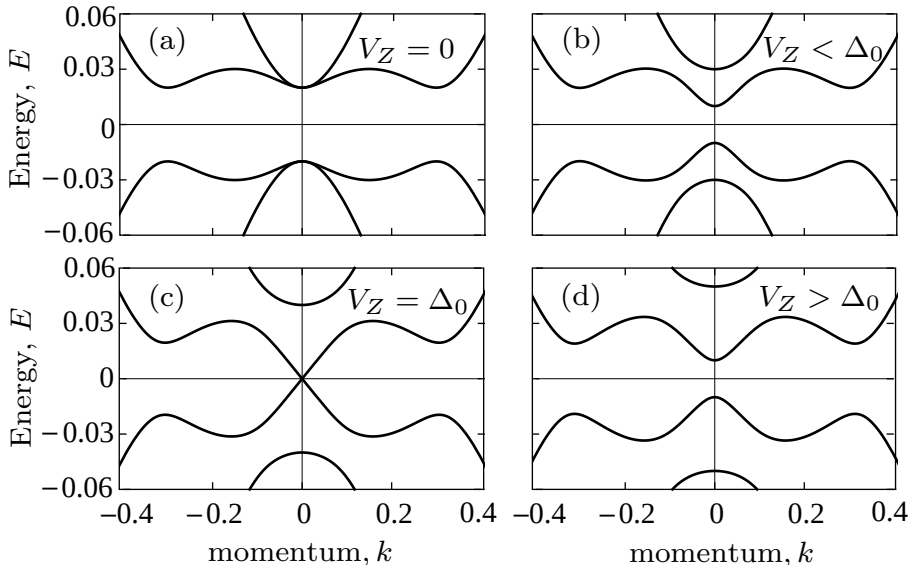

Figure 2.6: Energy spectrum of the SOCSW for different values of Zeeman potentials: (a) $V_Z = 0$ (nontopological), (b) $V_Z = 0.01$ (nontopological), (c) $V_Z = 0.02$ (transition), and (d) $V_Z = 0.03$ (topological). In all plots, we set $\alpha = 0.3$ and $\Delta_0 = 0.02$.

2.2.1 Strong Zeeman Splitting

In the limit of strong Zeeman splitting ($V_Z \gg \alpha$, Δ_0), the quasiparticle excitation spectrum of the SOCSW is split into two spin bands as shown in Fig. 2.7(a). In the normal state ($\Delta_0 = 0$) the spectrum is approximately given by $\epsilon_\pm(k) \approx k^2 \pm V_Z$. The system is essentially a half-metal, with only one spin-polarized band [$\epsilon_-(k)$] occupied. Projecting the full Hamiltonian into this band gives the effective Hamiltonian [12, 13, 15]

$$H'_S(k) = \sum_k \left\{ \epsilon_-(k)\psi^\dagger_{S-}(k)\psi_{S-}(k) + \left[\widetilde{\Delta}_-(k)\psi^\dagger_{S-}(k)\psi^\dagger_{S-}(-k) + \text{h.c.} \right] \right\}, \qquad (2.16)$$

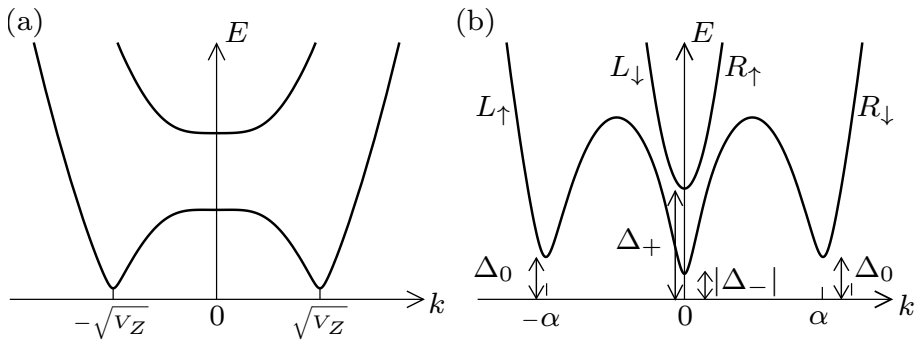

Figure 2.7: Energy spectrum of the SOCSW in the limits of (a) strong Zeeman field and (b) strong SOC. For clarity, only the positive energy branches of the spectrum are shown. In panel (b), the spectrum about the minima at $k = 0$ constitute the "interior" branches, while the spectrum about the minima at $k = \pm\alpha$ are the "exterior" branches. Note the different effective gaps for these branches, and the states contributing to the slowly varying left- and right-moving fields, $L_\sigma(x)$ and $R_\sigma(x)$, respectively.

where $\widetilde{\Delta}_-(k) \approx \alpha k \Delta_0 / V_Z$ is a p-wave pairing potential and $\psi_{S-}(\psi^\dagger_{S-})$ is the annihilation (creation) field operator for $\epsilon_-(k)$ band. The projected Hamiltonian is equivalent to the spinless pSC Hamiltonian $H_p(k)$ [Eq. (2.2)], with $\mu_p = V_Z$ and $\Delta_p = \alpha\Delta_0/V_Z$. If the Zeeman field is applied on both sides of the junction such that the NM is also fully spin polarized, then the low-energy sector is identical to the spinless NM-pSC junction, and the results obtained in Sec. 2.1 for the differential conductance directly apply.

2.2.2 Strong Spin-Orbit Coupling

In the case of strong SOC ($\alpha \gg V_Z, \Delta_0$), the BdG spectrum of the SOCSW is shown in Fig. (2.7)(b). In particular, we note that both the + and − spectra [Eq. (2.15)] have minima at $k = 0$ (the so-called interior branches), while the −

spectrum also has minima at $k = \pm\alpha$ (the exterior branches). For small energies $E \lesssim \Delta_0$, V_Z, we can linearize the Hamiltonian about these minima by using the ansatz for the field operators [67, 68]

$$\psi_{S\uparrow}(x) \approx R_\uparrow(x) + L_\uparrow(x)e^{-i\alpha x}, \tag{2.17a}$$

$$\psi_{S\downarrow}(x) \approx L_\downarrow(x) + R_\downarrow(x)e^{i\alpha x}, \tag{2.17b}$$

where $R_\sigma(x)$ and $L_\sigma(x)$ represent slowly-varying right- and left-moving fields, respectively; see Fig. (2.7)(b). Inserting this ansatz into the Hamiltonian [Eq. (2.14b)] and neglecting all "fast oscillating" terms (terms with phase factors $e^{\pm i\alpha x}$), we obtain effective Hamiltonians for the states near the interior and exterior branches. They are given by

$$\widetilde{H}_S^{(l)} = \frac{1}{2}\int dx \widetilde{\Psi}_S^{(l)}(x)^\dagger \widetilde{\mathcal{H}}_S^{(l)} \widetilde{\Psi}_S^{(l)}(x), \tag{2.18}$$

where $l = e, i$ denotes the exterior and interior branches, respectively, and the BdG Hamiltonians are written as

$$\widetilde{\mathcal{H}}_S^{(e)} = -i\alpha\tau_z\sigma_z\partial_x + \Delta_0\tau_x\,, \tag{2.19a}$$

$$\widetilde{\mathcal{H}}_S^{(i)} = -i\alpha\tau_z\sigma_z\partial_x + V_Z\sigma_x + \Delta_0\tau_x\,. \tag{2.19b}$$

The spinors for the interior and exterior branches are defined in terms of the slowly-varying field as

$$\widetilde{\Psi}_S^{(e)}(x) = (L_\uparrow(x), R_\downarrow(x), R_\downarrow^\dagger(x), -L_\uparrow^\dagger(x))^{\mathrm{T}},$$
$$\widetilde{\Psi}_S^{(i)}(x) = (R_\uparrow(x), L_\downarrow(x), L_\downarrow^\dagger(x), -R_\uparrow^\dagger(x))^{\mathrm{T}}. \tag{2.20}$$

We consider an electron with energy E and spin σ injected into the SOCSW from the NM. The wave function in the NM is given by

$$\Phi_{N\sigma}(x) = \begin{pmatrix} \delta_{\sigma\uparrow} \\ \delta_{\sigma\downarrow} \\ 0 \\ 0 \end{pmatrix} e^{ix} + \begin{pmatrix} b_{\sigma\uparrow} \\ b_{\sigma\downarrow} \\ 0 \\ 0 \end{pmatrix} e^{-ix} + \begin{pmatrix} 0 \\ 0 \\ a_{\sigma\downarrow} \\ a_{\sigma\uparrow} \end{pmatrix} e^{ix}, \tag{2.21}$$

where $\delta_{\sigma\sigma'}$ is the Kronecker symbol. The coefficients $a_{\sigma\sigma'}$ and $b_{\sigma\sigma'}$ are the amplitudes for Andreev and normal reflection, respectively. Note that due to the SOC in the SOCSW, both spin-flip and spin-preserving reflection processes are allowed. The wave function in the SOCSW is a superposition of solutions on the exterior and

interior branches

$$\Phi_{S\sigma}(x) = c_{\sigma 1}^{(i)} \begin{pmatrix} -u_- \\ \operatorname{sgn}(\Delta_-)v_- \\ -\operatorname{sgn}(\Delta_-)v_- \\ u_- \end{pmatrix} e^{ik_-^{(i)}x} + c_{\sigma 2}^{(i)} \begin{pmatrix} u_+ \\ v_+ \\ v_+ \\ u_+ \end{pmatrix} e^{ik_+^{(i)}x}$$
$$+ c_{\sigma 1}^{(e)} \begin{pmatrix} v_0 \\ 0 \\ u_0 \\ 0 \end{pmatrix} e^{i(k_0^{(e)}-\alpha)x} + c_{\sigma 2}^{(e)} \begin{pmatrix} 0 \\ u_0 \\ 0 \\ v_0 \end{pmatrix} e^{i(k_0^{(e)}+\alpha)x}, \tag{2.22}$$

where the first line on the right-hand side gives contributions from the interior branches, while the second line originates from the exterior branches. Note that the coefficients $c_{\sigma(1,2)}^{(i,e)}$ are the transmission coefficients into the SOCSW. The elements of the wave function are given by

$$u_\nu^2 = \begin{cases} \left(E + \sqrt{E^2 - \Delta_\nu^2}\right)/2E, & \text{for } E \geq |\Delta_\nu|, \\ \left(E + i\sqrt{\Delta_\nu^2 - E^2}\right)/2|\Delta_\nu|, & \text{for } 0 \leq E < |\Delta_\nu|, \end{cases} \tag{2.23}$$

and

$$v_\nu^2 + u_\nu^2 = \begin{cases} 1, & \text{for } E \geq |\Delta_\nu|, \\ E/|\Delta_\nu|, & \text{for } 0 \leq E < |\Delta_\nu|, \end{cases} \tag{2.24}$$

where $\nu = \pm, 0$, and $\Delta_\pm = \Delta_0 \pm V_Z$. The wave vectors appearing in Eq. (2.22) are $k_\pm^{(i)} = \sqrt{E^2 - \Delta_\pm^2}/\alpha$ for the interior branches, and $k_0^{(e)} = \sqrt{E^2 - \Delta_0^2}/\alpha$ for the exterior branches.

The wave functions satisfy the continuity and current conservation boundary conditions

$$\Phi_{S\sigma}(x)|_{x=0^+} = \Phi_{N\sigma}(x)|_{x=0^-}\,, \tag{2.25a}$$

$$J_S \Phi_{S\sigma}(x)|_{x=0^+} - J_N \Phi_{N\sigma}(x)|_{x=0^-} = -2iZ\tau_z \Phi_{N\sigma}(0), \tag{2.25b}$$

where the current operators are given by

$$J_N = -2i\partial_x \tau_z, \tag{2.26a}$$

$$J_S = -2i\partial_x \tau_z + \alpha \tau_z \sigma_z. \tag{2.26b}$$

In the limit of strong SOC ($\alpha \gg V_Z, \Delta_0$), we ignore terms proportional to $k_-^{(i)}$, $k_+^{(i)}$, $k_0^{(e)} \ll 1$ in the current conservation equation. Solving the boundary equations,

we obtain the Andreev (normal) reflection coefficients $a_{\sigma\sigma'}$ ($b_{\sigma\sigma'}$) as

$$
\begin{aligned}
a_{\uparrow\uparrow}(E) &= -\frac{\alpha u_0 v_0[u_- v_+ - \mathrm{sgn}(\Delta_-)u_+ v_-][1+(Z+i\frac{\alpha}{2})^2]}{\mathcal{D}_E^{(1)}\mathcal{D}_E^{(2)}}, && (2.27)\\
a_{\uparrow\downarrow}(E) &= \alpha u_0\left[\frac{v_+}{\mathcal{D}_E^{(1)}} + \mathrm{sgn}(\Delta_-)\frac{v_-}{\mathcal{D}_E^{(2)}}\right], && (2.28)\\
a_{\downarrow\uparrow}(E) &= \alpha v_0\left(\frac{u_+}{\mathcal{D}_E^{(1)}} + \frac{u_-}{\mathcal{D}_E^{(2)}}\right), && (2.29)\\
a_{\downarrow\downarrow}(E) &= -\frac{\alpha u_0 v_0\left[u_- v_+ - \mathrm{sgn}(\Delta_-)u_+ v_-\right]\left[1+(Z-i\frac{\alpha}{2})^2\right]}{\mathcal{D}_E^{(1)}\mathcal{D}_E^{(2)}}, && (2.30)\\
b_{\uparrow\uparrow}(E) &= b_{\downarrow\downarrow}(E)\\
&= -\frac{\left[(i+Z)^2+\left(\frac{\alpha}{2}\right)^2\right]}{\mathcal{D}_E^{(1)}\mathcal{D}_E^{(2)}}\times\\
&\quad \Big\{\mathrm{sgn}(\Delta_-)v_0^2 v_- v_+[Z^2+(\frac{\alpha}{2}-1)^2] + u_0^2 u_- u_+[Z^2+(1+\frac{\alpha}{2})^2]\\
&\quad -u_0 v_0[u_- v_+ + \mathrm{sgn}(\Delta_-)u_+ v_-][1+Z^2+(\frac{\alpha}{2})^2]\Big\}, && (2.31)\\
b_{\uparrow\downarrow}(E) &= \frac{\alpha u_0^2[u_- v_+ - \mathrm{sgn}(\Delta_-)u_+ v_-](1-iZ+\frac{\alpha}{2})^2}{\mathcal{D}_E^{(1)}\mathcal{D}_E^{(2)}}, && (2.32)\\
b_{\downarrow\uparrow}(E) &= \frac{\alpha v_0^2[u_- v_+ - \mathrm{sgn}(\Delta_-)u_+ v_-](-1+iZ+\frac{\alpha}{2})^2}{\mathcal{D}_E^{(1)}\mathcal{D}_E^{(2)}}, && (2.33)
\end{aligned}
$$

where

$$\mathcal{D}_E^{(1)} = u_0 u_+[Z^2+(\alpha/2+1)^2] - v_0 v_+[Z^2+(\alpha/2-1)^2], \quad (2.34a)$$

$$\mathcal{D}_E^{(2)} = u_0 u_-[Z^2+(\alpha/2+1)^2] - \mathrm{sgn}(\Delta_-)v_0 v_-[Z^2+(\alpha/2-1)^2]. \quad (2.34b)$$

The zero-temperature differential tunneling conductance $G_S(E)$ is calculated

	$V_Z < \Delta_0$	$V_Z = \Delta_0$	$V_Z > \Delta_0$
$a_{\uparrow\uparrow}(0)$	0	$\dfrac{\alpha[1+(Z+i\alpha/2)^2]}{D_1 D_2}$	$\dfrac{1+(Z+i\alpha/2)^2}{D_1}$
$a_{\uparrow\downarrow}(0)$	$-\dfrac{2i\alpha}{D_1}$	$-\dfrac{i\alpha}{D_1}$	$\dfrac{i}{2}-\dfrac{i\alpha}{D_1}$
$a_{\downarrow\uparrow}(0)$	$-\dfrac{2i\alpha}{D_1}$	$-i\alpha\left(\dfrac{1}{D_1}+\dfrac{1}{D_2}\right)$	$-\dfrac{i}{2}-\dfrac{i\alpha}{D_1}$
$a_{\downarrow\downarrow}(0)$	0	$\dfrac{\alpha[1+(Z-i\alpha/2)^2]}{D_1 D_2}$	$\dfrac{1+(Z-i\alpha/2)^2}{D_1}$
$b_{\uparrow\uparrow}(0)$	$\dfrac{2[(i+Z)^2+(\alpha/2)^2]}{D_1}$	$\dfrac{2[(i+Z)^2+(\alpha/2)^2][D_2-\alpha/2]}{D_1 D_2}$	$\dfrac{(i+Z)^2+(\alpha/2)^2}{D_1}$
$b_{\uparrow\downarrow}(0)$	0	$\dfrac{-i\alpha(1-iZ+\alpha/2)^2}{D_1 D_2}$	$\dfrac{-i(1-iZ+\alpha/2)^2}{D_1}$
$b_{\downarrow\uparrow}(0)$	0	$\dfrac{i\alpha(-1+iZ+\alpha/2)^2}{D_1 D_2}$	$\dfrac{i(-1+iZ+\alpha/2)^2}{D_1}$
$b_{\downarrow\downarrow}(0)$	$\dfrac{2[(i+Z)^2+(\alpha/2)^2]}{D_1}$	$\dfrac{2[(i+Z)^2+(\alpha/2)^2][D_2-\alpha/2]}{D_1 D_2}$	$\dfrac{(i+Z)^2+(\alpha/2)^2}{D_1}$
$\dfrac{G_S(0)}{G_0}$	$\dfrac{16\alpha^2}{D_1^2}$	$2\alpha\left(\dfrac{4}{D_1}-\dfrac{1}{D_2}\right)$	2

Table 2.3: Zero-bias values of the Andreev reflection coefficients $a_{\sigma\sigma'}(0)$, normal reflection coefficients $b_{\sigma\sigma'}(0)$, and differential conductance $G_S(0)$ in the strong SOC limit of the NM-SOCSW junction. The three columns give the values in the non-topological ($V_Z < \Delta_0$), transition ($V_Z = \Delta_0$) and topological ($V_Z > \Delta_0$) regimes. The terms $D_{1,2}$ are given by $D_1 = 2[1+Z^2+(\alpha/2)^2]$ and $D_2 = Z^2+(1+\alpha/2)^2$.

from the BTK formula

$$G_S(E) = G_0\left(2+\sum_{\sigma,\xi=\uparrow,\downarrow}\left\{|a_{\sigma\xi}(E)|^2-|b_{\sigma\xi}(E)|^2\right\}\right). \tag{2.35}$$

Although the general expression is complicated, compact forms for the reflection coefficients and the conductance at zero bias are presented in Table 2.3. As for the case the spinless NM-pSC junction studied in Sec. 2.1, the zero-bias conductance

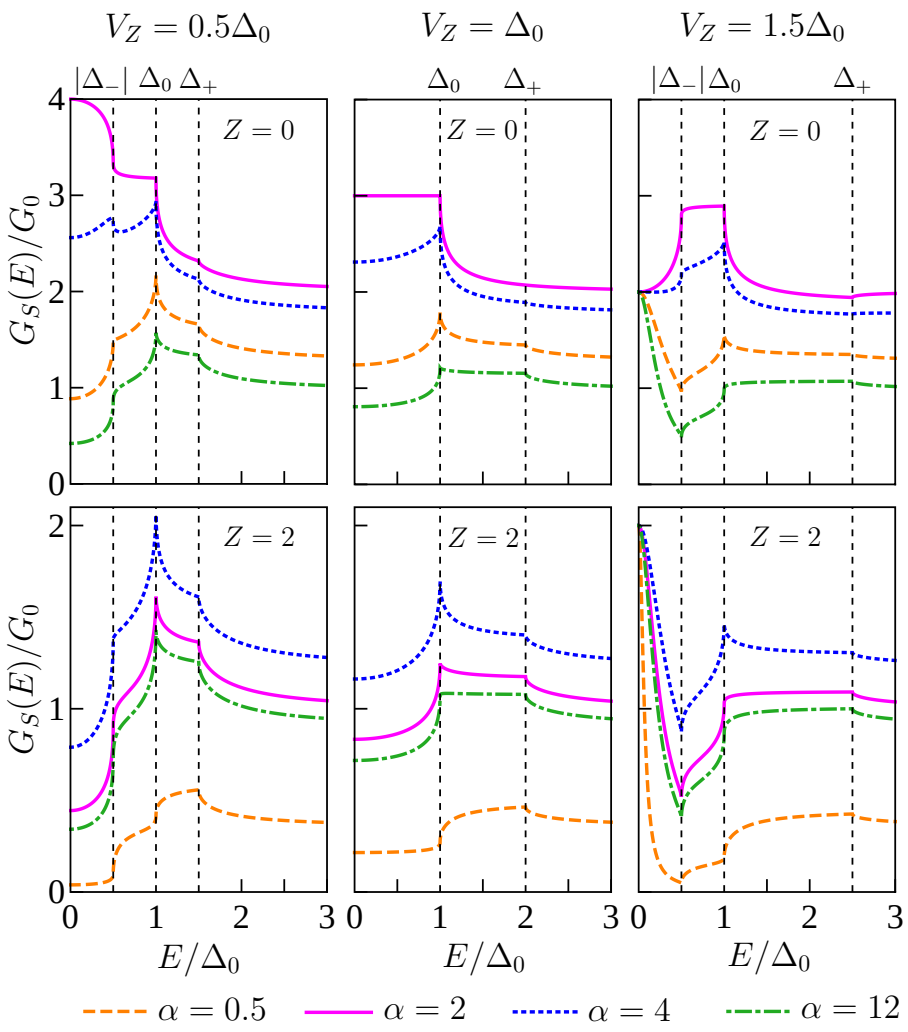

Figure 2.8: Plots of the tunneling conductance $G_S(E)$ of the NM-SOCSW junction in the strong SOC limit with different SOC strength α and Zeeman field V_Z. The results are plotted for the nontopological ($V_Z < \Delta_0$, left column), transition ($V_Z = 0$, middle column), and topological ($V_Z > \Delta_0$, right column) regimes, and for barrier strength $Z = 0$ (top row) and $Z = 2$ (bottom row). In all plots we set $\Delta_0 = 0.001$. The values of Δ_0 and V_Z are given in units of μ_N, while the values of α are expressed in units of μ_N/k_F.

$G_S(0)$ is discontinuous across the topological phase transition. In the topological regime ($V_Z > \Delta_0$) the zero-bias conductance takes the quantized value $G_S(0) = 2G_0$. This implies that the Andreev reflection coefficients in Eq. (2.35) exactly cancel the normal reflection coefficients; moreover, from Table 2.3 it can be verified that

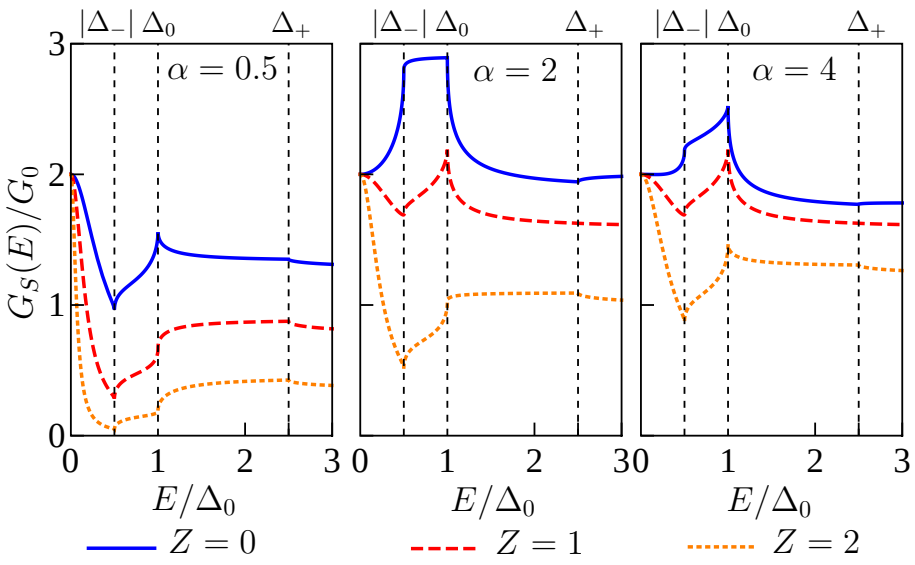

Figure 2.9: Plots of the tunneling conductance $G_S(E)$ of the NM-SOCSW junction in the topological regime for the strong SOC limit with different potential barrier strength Z and spin-orbit coupling strength α. We set $\Delta_0 = 0.001$ and $V_Z = 1.5\Delta_0$. The values of Δ_0 and V_Z are given in units of μ_N, while the values of α are expressed in units of μ_N/k_F. Note that in the topological regime, the zero-bias conductance is quantized at $2G_0$ independent of the junction details.

$\sum_{\sigma,\xi} |a_{\sigma\xi}(0)|^2 = \sum_{\sigma,\xi} |b_{\sigma\xi}(0)|^2 = 1$. This can be understood in terms of the existence of a single Majorana mode at the interface which couples to one of the two channels in the normal region [33, 69]. While there is perfect Andreev reflection in this channel, in the other channel we have perfect normal reflection. In the nontopological regime, on the other hand, $G_S(0)$ takes on nonuniversal values and is dependent upon Z and α. In particular, the zero-bias conductance in the nontopological phase can strongly exceed the quantized value in the topological state: for the gapped nontopological state ($V_Z < \Delta_0$) and at the topological transition point ($V_Z = \Delta_0$), we find the maximum values $G_S(0) = 4$ and $G_S(0) = 3$, respectively, which are realized for $Z = 0$ and $\alpha = 2$.

We plot the calculated conductance as a function of energy in Figs. 2.8 and 2.9. In the former we show examples of the conductance spectra in the nontopological, transition, and topological regimes, while the latter explores more fully the variation of the conductance spectra in the topological state away from zero bias. The conductance spectra show a much more complicated structure than those in the spinless NM-pSC junction, reflecting the presence of three distinct gaps (Δ_+, $|\Delta_-|$, Δ_0) in the strong SOC limit of the SOCSW. Indeed, at the energy corresponding to each gap we observe a nonanalyticity in the conductance spectrum. Although there is considerable variation in the conductance spectrum as a function of energy, a number of trends can be discerned: increasing Z tends to suppress the conductance, the energy variation of the conductance is nonmonotonic in general with cusplike structures at specific energies, and the energy variation of the conductance is stronger near zero energy for larger values of Z. While the conductance at first tends to be enhanced by increasing the SOC, the conductance eventually goes through a maximum before monotonically decreasing. Similarly, the SOC increases the width of the zero-bias peak in the topological regime, but beyond a certain SOC strength it decreases again. The basic finding is that, other than the universal quantized Majorana peak at zero energy, the tunneling conductance shows interesting and nontrivial dependence on Z and E in the topological phase. In particular, an interesting conclusion of our theory is that the zero-bias conductance could be quantized in the topological phase for small values of Z without developing a peak in the tunneling conductance at all.

Note that the above discussion holds true also for the case where the Zeeman

coupling in the normal lead or the chemical potential μ_S of the SOCSW are nonzero. For the case where $|\Delta_-| < \Delta_0$, the zero-bias peak formed in the topological regime is within an energy range of $|\Delta_-|$. Since the topological gap $|\Delta_-| = |V_Z - \sqrt{\Delta_0^2 + \mu_S^2}|$ decreases with the absolute value of the chemical potential $|\mu_S|$, the width of the zero-bias peak decreases with $|\mu_S|$.

2.3 Conclusion

Using the BTK formalism we have analytically studied the zero-temperature tunneling conductance spectra of NS junctions involving topological superconductors. Finite temperature effects within this formalism simply lead to thermal broadening of the zero-temperature conductance and can be included in the theory numerically by introducing an integration over the Fermi function. As in the BTK paper [65], the finite-voltage conductances are found to depend on the strength of the barrier at the interface, which is parameterized by the dimensionless parameter Z. Specifically, we have examined a spinless NM-pSC junction and a spinful NM-SOCSW junction, paying particular attention to the change in the zero-bias conductance across the topological phase transition. We explicitly demonstrate that the zero-temperature zero-bias conductance is quantized at a value of $2e^2/h$ in the topological regime, in agreement with effective models of these systems based on a single Majorana mode coupled to a normal channel. Despite this quantization at zero voltage, the zero-bias conductance only develops a peak (or a local maximum) as a function of voltage for barriers with sufficiently large Z parameter,

or for small and large SOC strength. These parameters also control the width of this peak. In the nontopological regime, on the other hand, the conductance takes nonuniversal values depending upon the details of the system. In both cases the conductance spectrum away from zero bias shows considerable variation with the details of the junction. Our calculated BTK conductance also shows that the conductance is finite inside the superconducting gap region because of the finite barrier transparency, providing a possible mechanism for the observed "soft gap" feature in the experimental studies [16, 18, 19, 20, 21]. This effect is qualitatively similar to the "inverse proximity effect" at the NS interface arising from the finite barrier at the interface as discussed in Ref. [70], although other possible physical mechanisms for the soft gap behavior have also been proposed [71]. We mention finally that our theory is for a single NS junction which effectively assumes the existence of only a single Majorana mode at the NS interface (with the other Majorana being located infinitely far away) and thus Majorana splitting [72, 73, 74, 75] due to the wave function overlap between two Majorana modes is not germane to our theory.

Chapter 3

Transport Spectroscopy of Superconductor–Normal Metal–Superconductor Junctions

In the previous chapter, we have shown that the quantized $2e^2/h$ zero-temperature zero-bias conductance of a normal-metal–topological superconductor junction is a robust signature of the MZM. In the weak-tunneling limit (small junction transparency), the zero-bias conductance develops as a peak in the conductance spectra. While the ZBCP have been carefully shown in the experiment to correspond to the topological regime, the observed zero-bias conductance is still far below the expected quantized value. This deviation can be attributed at least in part to thermal broadening in the normal metal lead which in turn broadens the zero-bias peak and reduces its maximum conductance value. To mitigate the effect of thermal broadening, one can use a superconducting lead instead of a normal lead in probing the MZM tunneling conductance. In a superconducting lead, the quasiparticle excitation is exponentially suppressed by the superconducting gap $\sim \exp(-\Delta_{\text{lead}}/T)$ which in turn suppresses the thermal broadening effect.

In this chapter, we study the transport of various voltage-biased 1D SNS

junctions with arbitrary junction transparency where the superconductor can be either nontopological or topological. In particular, we consider two models for the topological superconductors: (i) a spinful p-wave superconductor and (ii) a spin-split spin-orbit-coupled s-wave superconductor. We provide a comprehensive analysis of the zero-temperature dc current I and differential conductance dI/dV of the SNS junctions with or without the MZMs. The presence of the MZM necessarily gives rise to two tunneling conductance peaks: each at the voltage $eV = \pm\Delta_{\text{lead}}$, i.e., the voltage at which the lead superconducting gap edge aligns with the MZM. For the case where the superconducting probe lead has a BCS singularity (where $\sum_{\sigma=\uparrow,\downarrow} |u_\sigma|^2 = \sum_{\sigma=\uparrow,\downarrow} |v_\sigma|^2$ at the gap edge with u and v being the electron and hole component of the superconducting wavefunction at the gap edge), e.g. an s-wave superconductor or a spin-orbit coupled superconducting nanowire with no magnetic field, the tunneling conductance peaks appearing at $eV = \pm\Delta_{\text{lead}}$ are quantized at a value $(4-\pi)2e^2/h$, independent of the junction transparency, due to resonant Andreev reflection from the MZM. In the tunneling limit (small junction transparencies) where only single Andreev reflections contribute to the current, the conductance for voltages below the superconducting lead gap Δ_{lead} is zero. However, when the junction transparency is not small, there is a finite conductance for $e|V| < \Delta_{\text{lead}}$ arising from multiple Andreev reflections (MAR). The conductance at $eV = \pm\Delta_{\text{lead}}$ in this case is no longer quantized.

Moreover, we find that the MZM conductance peak probed using a superconductor lead without a BCS singularity has a non-universal value which decreases with decreasing junction transparency. We further show that, for certain values

of parameters, the tunneling conductance from a zero-energy Andreev bound state (ABS) can resemble the conductance from a true Majorana mode. For non-zero Andreev bound states, the conductance peak shifts away from the gap-bias voltage $eV = \pm\Delta_{\text{lead}}$ towards a larger voltage value by the ABS energy.

In this chapter, we study theoretically the dc current-voltage ($I - V$) relation and differential conductance ($G = dI/dV$) spectra of 1D SNS junctions involving two models of topological superconductors, i.e., the spinful p-wave superconductor (pSC) and the spin-orbit coupled s-wave superconducting wire (SOCSW). More specifically, we consider various combinations of the junctions where the superconductors can be either in the topological or nontopological regime. This chapter is based on Refs. [57, 58] and the figures in this chapter are adapted from the same references.

3.1 Scattering Matrix Formalism

We begin by modeling the SNS junction by two semi-infinite superconducting leads connected by a normal region with a delta-function barrier of strength Z [see Fig. 3.1(a)]. The normal region is assumed to be infinitesimally short with large chemical potential such that the propagating modes in this region have constant group velocity independent of its energy. Quasiparticles can be injected from the left or right superconducting lead which become electrons or holes (depending on their energy) when they enter the normal region. Due to the voltage bias, these electrons (holes) will then gain (lose) an energy of eV as it is accelerated from the

left (right) to the right (left). As a result, after each Andreev reflection at the NS interface, an incoming electron with an energy E will be reflected as a hole back into the same region with an energy $E + 2eV$. The quasiparticle retroreflects repeatedly inside the normal region until it gains enough energy to be transmitted into the superconductors [Fig. 3.1(b)]. This mechanism is termed the multiple Andreev reflections (MAR) [76, 77, 78].

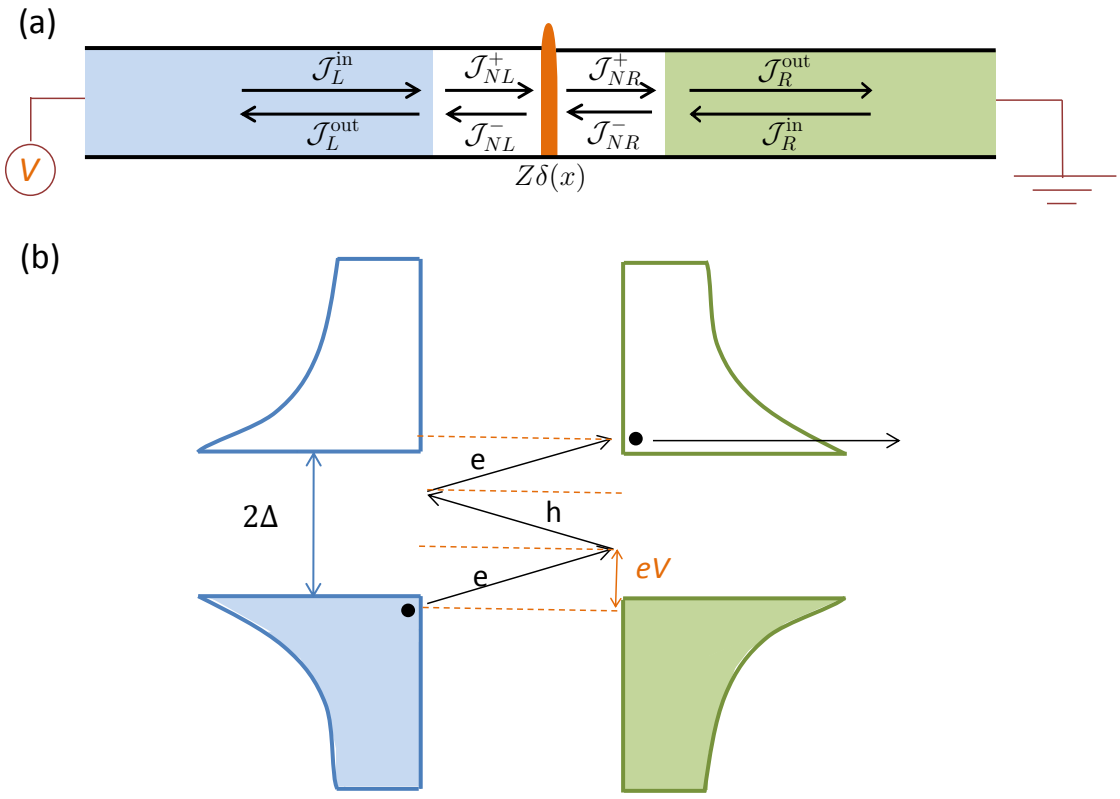

Figure 3.1: (a) Schematic diagram of a superconductor–normal metal–superconductor (SNS) junction with a delta-function potential barrier of strength Z. (b) Multiple Andreev reflections.

The scattering processes in the SNS junction can be split into three regions: (i) left NS interface, (ii) tunnel barrier and (iii) right NS interface. It can be written

in terms of the scattering matrices as

$$\begin{pmatrix} \mathcal{J}^{\text{out}}_{L,\nu}(E_n) \\ \mathcal{J}^{+}_{NL,\nu}(E_n) \end{pmatrix} = S_L(E_n) \begin{pmatrix} \mathcal{J}^{\text{in}}_{L,\nu}(E_n)\delta_{n0}\delta_{\nu,\rightarrow} \\ \mathcal{J}^{-}_{NL,\nu}(E_n) \end{pmatrix}, \tag{3.1a}$$

$$\begin{pmatrix} \mathcal{J}^{-}_{NL,\nu}(E_n) \\ \mathcal{J}^{+}_{NR,\nu}(E_n) \end{pmatrix} = \sum_{n'} S_N(E_n, E_{n'}) \begin{pmatrix} \mathcal{J}^{+}_{NL,\nu}(E_{n'}) \\ \mathcal{J}^{-}_{NR,\nu}(E_{n'}) \end{pmatrix}, \tag{3.1b}$$

$$\begin{pmatrix} \mathcal{J}^{\text{out}}_{R,\nu}(E_n) \\ \mathcal{J}^{-}_{NR,\nu}(E_n) \end{pmatrix} = S_R(E_n) \begin{pmatrix} \mathcal{J}^{\text{in}}_{R,\nu}(E_n)\delta_{n0}\delta_{\nu,\leftarrow} \\ \mathcal{J}^{+}_{NR,\nu}(E_n) \end{pmatrix}, \tag{3.1c}$$

where $E_n = E + neV$ is the energy of the propagating modes with n being an integer, $\mathcal{J}^{\rho}_{\ell,\nu} = (j^{e,\uparrow,\rho}_{\ell,\nu}, j^{e,\downarrow,\rho}_{\ell,\nu}, j^{h,\uparrow,\rho}_{\ell,\nu}, j^{h,\downarrow,\rho}_{\ell,\nu})^{\mathrm{T}}$ is the current amplitude vector for region $\ell = L$ (left superconductor), NL (normal region to the left of the tunnel barrier), NR (normal region to the right of the tunnel barrier) and R (right superconductor) with $\rho = +/-$ and $\rho =$ in/out being the right/left-moving modes and incoming/outgoing modes indices, respectively, and $\nu = \rightleftarrows$ denoting whether the incoming quasiparticle is from the left or right superconductor. We note that the scattering matrix formalism presented above is completely general and can be utilized to study the transport properties of any kind of SNS junctions. Moreover, it can be easily interfaced with the numerical transport package Kwant [79] which can be used to calculate the scattering matrices of the left (S_L) and right (S_R) NS interfaces [36, 65]. For details on the numerical simulation, please refer to Appendix A.

The scattering matrix $S_N(E_n, E'_n)$ in Eq. (3.1)(b) incorporates the scattering processes at the tunnel barrier and the increase (decrease) of the electron (hole)

energy by eV each time the electron (hole) passes from the left to the right. In terms of the electron (S_N^e) and hole (S_N^h) component, it can be written as

$$S_N(E_n, E_{n'}) = S_N^e(E_n, E_{n'}) \otimes \sigma_0 \otimes \tau_+ + S_N^h(E_n, E_{n'}) \otimes \sigma_0 \otimes \tau_-, \tag{3.2}$$

where σ_0 is the identity matrix in the spin subspace, $\tau_\pm = \tau_x \pm i\tau_y$ are the Pauli matrices in the particle-hole subspace. The scattering matrices S_N^e and S_N^h are given by

$$S_N^e(E_n, E_{n'}) = \begin{pmatrix} r\delta_{n,n'} & t\delta_{n,n'+1} \\ t\delta_{n,n'-1} & r\delta_{n,n'} \end{pmatrix}, \tag{3.3a}$$

$$S_N^h(E_n, E_{n'}) = \begin{pmatrix} r^*\delta_{n,n'} & t^*\delta_{n,n'-1} \\ t^*\delta_{n,n'+1} & r^*\delta_{n,n'} \end{pmatrix}, \tag{3.3b}$$

where $r = -iZ/(1+iZ)$ and $t = 1/(1+iZ)$ are the reflection and transmission coefficients, respectively, with the amplitudes depending on the delta-function barrier strength Z. We change the junction transparency in the simulation by tuning Z. Since sharp changes of parameters across the junction, such as the mismatch in the Fermi level, spin-orbit coupling, p-wave pairing potential etc., also effectively create barriers for the current, we use a parameter-independent quantity G_N to characterize the junction transparency, where G_N is the normalized conductance of the SNS junction at high voltages (in the unit of $G_0 = e^2/h$) which is the conductance of the corresponding normal-normal (NN) junction.

Solving the coupled linear equations [Eq. (3.1)], we obtain the current am-

plitudes $\mathcal{J}^{\rho}_{\ell,\nu}$. The total current can be calculated by adding up the contribution from the left- and right-moving modes of the electrons and holes for the incoming quasiparticles from the left and right superconductors, i.e.,

$$I_\nu(V) = \frac{2e}{h}\int_{-\infty}^{0} dE \mathrm{Tr}\left(\sum_n \rho_z \tau_z J_{NL,\nu}(E_n) J^{\dagger}_{NL,\nu}(E_n)\right), \tag{3.4}$$

where

$$J_{NL,\nu} = (j^{e,\uparrow,+}_{NL,\nu}, j^{e,\downarrow,+}_{NL,\nu}, j^{h,\uparrow,+}_{NL,\nu}, j^{h,\downarrow,+}_{NL,\nu}, j^{e,\uparrow,-}_{NL,\nu}, j^{e,\downarrow,-}_{NL,\nu}, j^{h,\uparrow,-}_{NL,\nu}, j^{h,\downarrow,-}_{NL,\nu})^{\mathrm{T}} \tag{3.5}$$

is the current amplitude vector in the normal region to the left of the barrier. As is proven in Appendix B, the current is non-negative for positive V. The differential conductance ($G = dI/dV$) can be computed by directly differentiating the current I with respect to the voltage V. In general, the differential conductance is particle-hole asymmetric except for sufficiently small transparencies.

In this chapter, we apply the above scattering matrix formalism to calculate the conductance for the junctions of (i) the spinful pSC, and (ii) the SOCSW. We will explore different combination of the junctions where none, one or both of the superconductors are topological and compute the zero-temperature dc current-voltage relation and differential conductance for these junctions.

3.2 Subharmonic Gap Structure

In general, for SNS junctions with asymmetric gap ($\Delta_L \neq \Delta_R$), where $\Delta_{L,R}$ are the superconducting gap of the left and right superconductors, when the junc-

tion transparency is not small there will be nonanalyticities in the I-V curve or conductance [76, 77, 78] at specific voltages, which is termed the "subharmonic gap structure" (SGS). The sharp change in the conductance happens at voltages at which there is a change in the number of Andreev reflections required to transfer charge from the occupied to the empty band. For the incoming quasiparticles from the left superconductor, the number of Andreev reflections changes when [see Fig. 3.2(a) and (b)]

$$e|V| = \frac{\Delta_L}{n}, \quad n \geq 1, \tag{3.6}$$

and

$$e|V| = \frac{\Delta_L + \Delta_R}{2n-1}, \quad 1 \leq n \leq \frac{\Delta_R}{\Delta_R - \Delta_L}, \tag{3.7}$$

and for the incoming quasiparticles from the right superconductor, this change happens at voltages [see Fig. 3.2(c) and (d)]

$$e|V| = \frac{\Delta_L + \Delta_R}{2n-1}, \quad 1 \leq n \leq \frac{\Delta_R}{\Delta_R - \Delta_L}, \tag{3.8}$$

and

$$e|V| = \frac{\Delta_R}{n}, \quad 1 \leq n \leq \frac{\Delta_R}{\Delta_R - \Delta_L}. \tag{3.9}$$

Without loss of generality, in the above we assume $\Delta_R > \Delta_L$. The range of n in Eqs. (3.6)-(3.9) gives the voltage range for "strong" SGS, where all Andreev reflections happen inside the superconducting gap. The SGS that happens outside this range of n is termed the "weak" SGS because the Andreev reflections that happen outside the gap are generally small in amplitude.

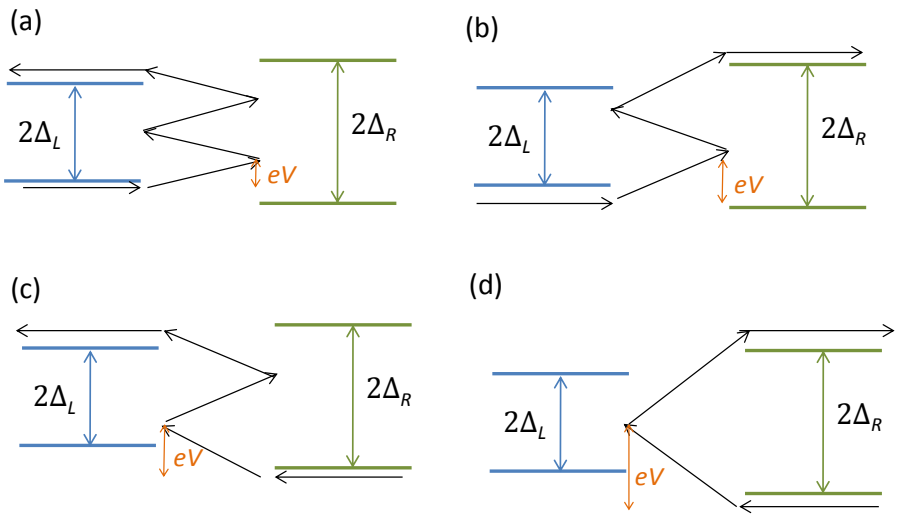

Figure 3.2: Various MAR paths contributing to the SGS. The MAR paths for a right-moving incoming quasiparticles are given in (a) and (b) which correspond to the voltages given in Eqs. (3.6) and (3.7). The MAR paths for a left-moving incoming quasiparticles are given in (c) and (d) which correspond to the voltages given in Eqs. (3.8) and (3.9).

Table 3.1: Voltages at which the subharmonic gap structure appears for an asymmetric SNS junction.

SGS voltage $e\|V\|$	Range of n
Δ_L/n	$n \geq 1$
$(\Delta_L + \Delta_R)/(2n-1)$	$n \geq 1$
Δ_R/n	$n \geq 1$

The SGS (including both "strong" and "weak") happens at the voltages given in Table 3.1 (Refs. [80, 81]) where for spectrum with multiple gaps, $\Delta_{L,R}$ refer to each value of the superconducting gaps in the left and right superconductors. In general, the SGS is not apparent for near-perfect transparency junction and becomes sharper in the intermediate range of transparencies. Decreasing the transparency further into the tunneling limit will diminish the SGS at small voltages.

3.3 Spinful p-wave Superconductor Junctions

In this section, we consider the junctions between an s-wave superconductor (sSC) and a pSC and the junctions between two pSCs where the pSC can be in the nontopological or topological regime. Using the BdG form, we can write the Hamiltonian of the system as

$$H_j(x) = \frac{1}{2}\int dx \Psi_j^\dagger(x)\mathcal{H}_j\Psi_j(x), \tag{3.10}$$

where $\Psi_j(x) = \left(\psi_{j\uparrow}(x), \psi_{j\downarrow}(x), \psi_{j\downarrow}^\dagger(x), -\psi_{j\downarrow}^\dagger(x)\right)^{\mathrm{T}}$ are Nambu spinors with $\psi_{j\sigma}^\dagger(x)$ and $\psi_{j\sigma}(x)$ being the creation and annihilation operators of an electron of spin σ for the superconductor of type $j = s, p$ (s-wave or p-wave). The BdG Hamiltonian of the sSC and pSC are given by

$$\mathcal{H}_s = \left(-\frac{\hbar^2\partial_x^2}{2m} - \mu_s\right)\tau_z + \Delta_s\tau_x, \tag{3.11a}$$

$$\mathcal{H}_p = \left(-\frac{\hbar^2\partial_x^2}{2m} - \mu_p\right)\tau_z + V_Z\sigma_z - i\Delta_p\partial_x\tau_x\sigma_x, \tag{3.11b}$$

respectively. Here, m is the electron effective mass (which we set to be $m = 0.015m_e$ throughout where m_e is the bare electron mass), μ_s and μ_p are the chemical potentials of the sSC and pSC, V_Z is the Zeeman field, Δ_s and Δ_p are the sSC and pSC pairing potentials, and $\tau_{x,y,z}$ ($\sigma_{x,y,z}$) are Pauli matrices acting in the particle-hole (spin) subspace. The effective chemical potential in each spin channel of the pSC ($\mu_p \pm V_Z$) determines whether that channel is topological or not. The channel is topological if the chemical potential is positive, otherwise it is non-topological [3, 4].

The spinful pSC can have zero, one or two topological channels depending on the values of V_Z and μ_p, i.e.,

(a) $|V_Z| < |\mu_p|$ and $\mu_p < 0$, no topological channel,

(b) $|V_Z| > \mu_p$ and $\mu_p > 0$, one topological channel,

(c) $|V_Z| < \mu_p$ and $\mu_p > 0$, two topological channels.

Throughout this chapter, we denote the pSC in the three different regimes as p_i, where $i = 0, 1, 2$, refers to the number of the topological channels in the pSC. Since the spinful pSC is essentially made up of two uncoupled spinless pSCs, the spectrum of the spinful pSC then consists of the spectrum of two spinless pSCs [see Sec. 2.1] with effective chemical potential $\mu_p \pm V_Z$ as shown in Fig. 3.3. In the following we will denote the smallest gap in the spectrum of the p_i-SC by Δ_{p_i}.

3.3.1 sNp_0 junction

Let us begin by considering the s-wave superconductor–normal metal–p_0 superconductor (sNp_0) junction. The p_0-SC is a spinful p-wave superconductor with no topological channel where it has negative chemical potential ($\mu_p < 0$) and Zeeman field $|V_Z| < |\mu_p|$. Its spectrum has a gap at $k = 0$ with a value $|\mu_p| \pm |V_Z|$ with the smallest gap being $\Delta_{p_0} = |\mu_p| - |V_Z|$ [3, 4, 36] as shown in Fig. 3.3. In general, the current and conductance for the SNS junction involving p_0-SC, e.g., the sNp_0 junction discussed here, increase with the p_0-SC pairing potential Δ_p. Since the p_0-SC is essentially an insulator and the Andreev reflection amplitude in an Np_0 junction is small, the current for junctions involving p_0-SC is generally small and the SGS is

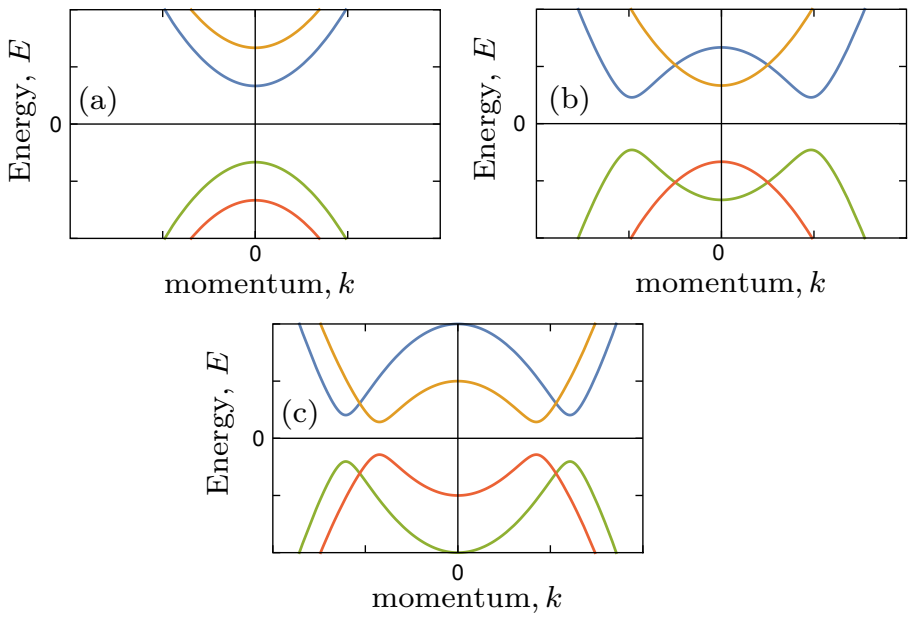

Figure 3.3: Energy spectrum of a spinful pSC for different parameter regimes: (a) $|V_Z| < |\mu_p|$ and $\mu_p < 0$ (p_0-SC with no topological channel), (b) $|V_Z| > \mu_p$ and $\mu_p > 0$ (p_1-SC with one topological channel), (c) $|V_Z| < \mu_p$ and $\mu_p > 0$ (p_2-SC with two topological channels).

strongly suppressed as can be seen in Fig. 3.4. At high voltages ($|V| \gg \Delta_s, \Delta_{p_0}$), the conductance approaches the conductance G_N of the corresponding NN junction (which we define as the junction transparency throughout this chapter). The current and conductance decrease with decreasing junction transparency G_N as can be seen in Fig. 3.4. In the weak tunneling or small transparency limit where MAR is suppressed, the current starts to flow only when the voltage is greater than $e|V| = \Delta_s + \Delta_{p_0}$, i.e., the voltage where the superconducting gap edges of both sSC and p_0-SC line up.

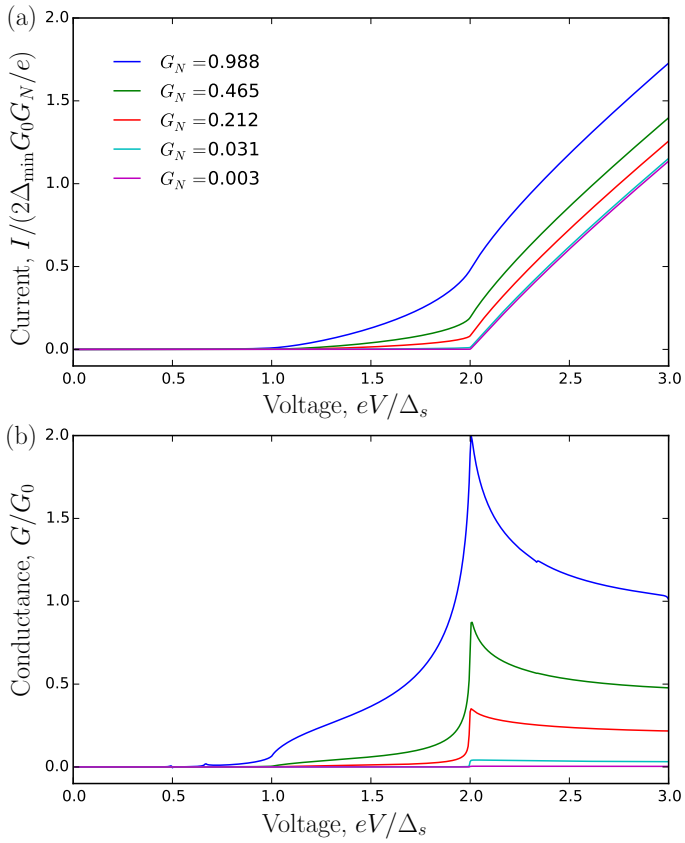

Figure 3.4: Plots of (a) dc current I and (b) normalized differential conductance G/G_0 versus bias voltage V for an sNp_0 junction with various values of transparencies G_N. The parameters used for the sSC are $\mu_s = 20$ K and $\Delta_s = 0.01$ K. The parameters used for the p_0-SC are $\mu_p = -0.01$ K, $V_Z = 0$ K, $\Delta_p = 0.2$ eVÅ, where the smallest gap is $\Delta_{p_0} = 0.01$ K. The smallest gap in the junction is $\Delta_{\min} = 0.01$ K.

3.3.2 sNp_1 junction

The p_1-SC has one topological channel with a pair of MZM: one at each end. The energy spectrum of the p_1-SC is given in Fig. 3.3(b). The plots of the current and conductance for the sNp_1 junction in the limit of large and small Zeeman field are plotted against the bias voltage in Figs. 3.5 and 3.6, respectively. In the large Zeeman limit $[(|V_Z| - \mu_p) \gtrsim \mu_p]$, the p_1-SC is essentially a spinless topological pSC [3, 4].

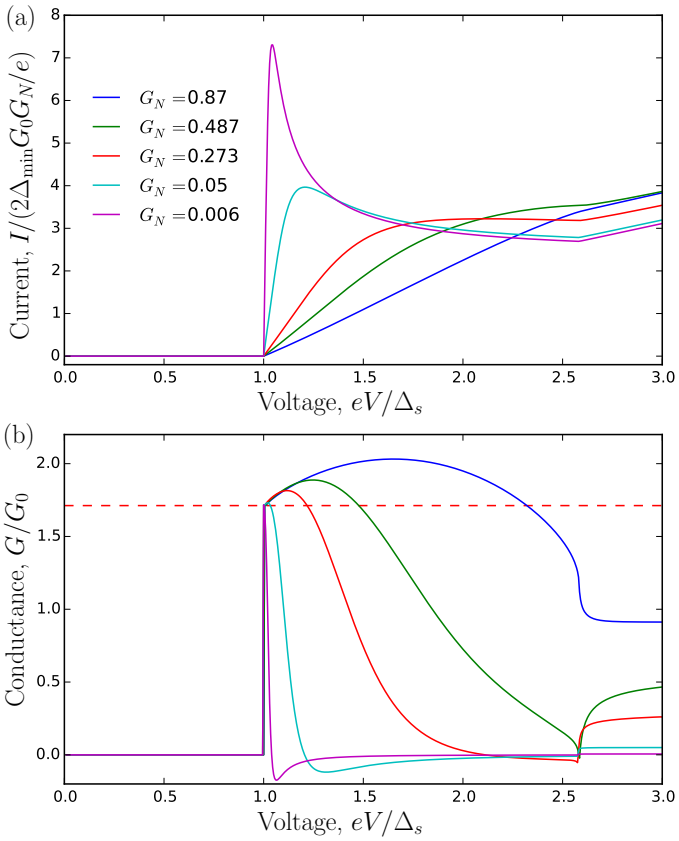

Figure 3.5: Plots of (a) dc current I and (b) normalized differential conductance G/G_0 versus bias voltage V for an sNp_1 junction with various values of transparencies G_N in the limit of large Zeeman field ($V_Z = 2\mu_p$). The red dashed line $[G_M = (4-\pi)2e^2/h]$ is the conductance value due to single Andreev reflections from the MZM. The parameters used for the sSC are $\mu_s = 200$ K and $\Delta_s = 2.5$ K. The parameters used for the p_1-SC are $\mu_p = 20$ K, $V_Z = 40$ K, $\Delta_p = 0.0785$ eVÅ, where the smallest gap is $\Delta_{p_1} = 4$ K. The smallest gap in the junction is $\Delta_{\min} = 2.5$ K.

In this limit, MAR are totally suppressed and only single Andreev reflections are allowed for the sNp_1 junction because the sSC allows only spin-singlet Andreev reflections while the spinless pSC allows only spin-triplet Andreev reflections. This results in a step jump in the conductance from zero to the quantized value $G_M = (4-\pi)2e^2/h$ at the threshold voltage $e|V| = \Delta_s$ [52, 57, 82] as shown in Fig. 3.4(b). The quantized value G_M corresponds to the conductance due to single Andreev

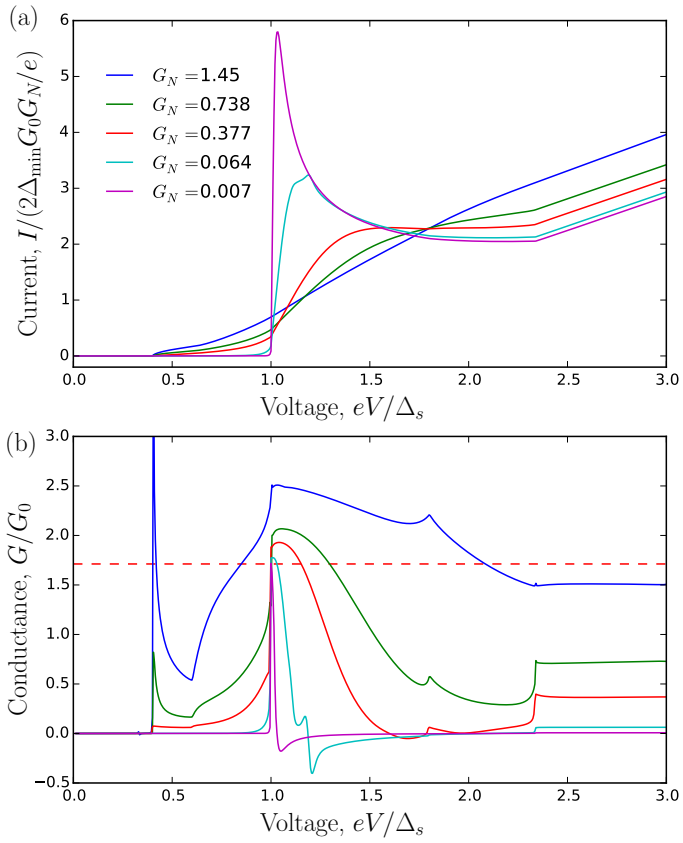

Figure 3.6: Plots of (a) dc current I and (b) normalized differential conductance G/G_0 versus bias voltage V for an sNp_1 junction with various values of transparencies G_N in the limit of small Zeeman field ($V_Z = 1.1\mu_p$). The red dashed line $[G_M = (4-\pi)2e^2/h]$ is the conductance value due to single Andreev reflections from the MZM. The parameters used for the sSC are $\mu_s = 200$ K and $\Delta_s = 2.5$ K. The parameters used for the p_1-SC are $\mu_p = 20$ K, $V_Z = 22$ K, $\Delta_p = 0.0785$ eVÅ, where the gaps are 2 K and 3.4 K with the smallest gap for the p_1-SC being $\Delta_{p_1} = 2$ K. The smallest gap in the junction is $\Delta_{\min} = 2$ K.

reflections from the MZM which happen at the voltage when the BCS singularity and MZM are aligned. In this large Zeeman limit, since MAR are suppressed the quantized value G_M is robust against the junction transparency. The conductance, in general, decreases with decreasing junction transparency and for sufficiently small transparency, the conductance can become negative for voltages near the threshold

voltage $e|V| = \Delta_s$. Our results for the sNp_1 junction in the large Zeeman limit, calculated using the scattering matrix formalism, are similar to those of the s-wave superconductor–normal metal–spinless p-wave superconductor junctions calculated using the Green's function formalism [82]. Recently, the conductance of the spinless p-wave superconductor has been measured using the s-wave superconducting tip in the STM experiment [56]. In the limit of small Zeeman field [$(|V_Z| - \mu_p) \ll \mu_p$] where the junction transparency is not small, MAR are allowed. As a result, there is a finite current and conductance with SGS below the threshold voltage $e|V| = \Delta_s$. However, the current and conductance near zero voltage are zero due to the difference in the Andreev reflection spin-selectivity of the sSC and MZM, i.e., the sSC allows spin-singlet Andreev reflections and the MZM favors spin-triplet Andreev reflections [63, 69]. In this limit, due to MAR the conductance at the voltage $e|V| = \Delta_s$ is no longer robust against increasing junction transparency. The current and conductance generally decrease with decreasing junction transparency. For sufficiently small transparency where only single Andreev reflections are allowed, $G(e|V| = \Delta_s) = G_M$ independent of the junction transparency .

3.3.3 sNp_2 junction

The p_2-SC has two topological channels with two MZMs at each end. The energy spectrum for the p_2-SC is shown in Fig. 3.3(c). The current and conductance plots for the sNp_2 junction are depicted in Fig. 3.7. In the tunneling limit, the conductance for the sNp_2 junction develops a step jump from 0 to $2G_M$ at

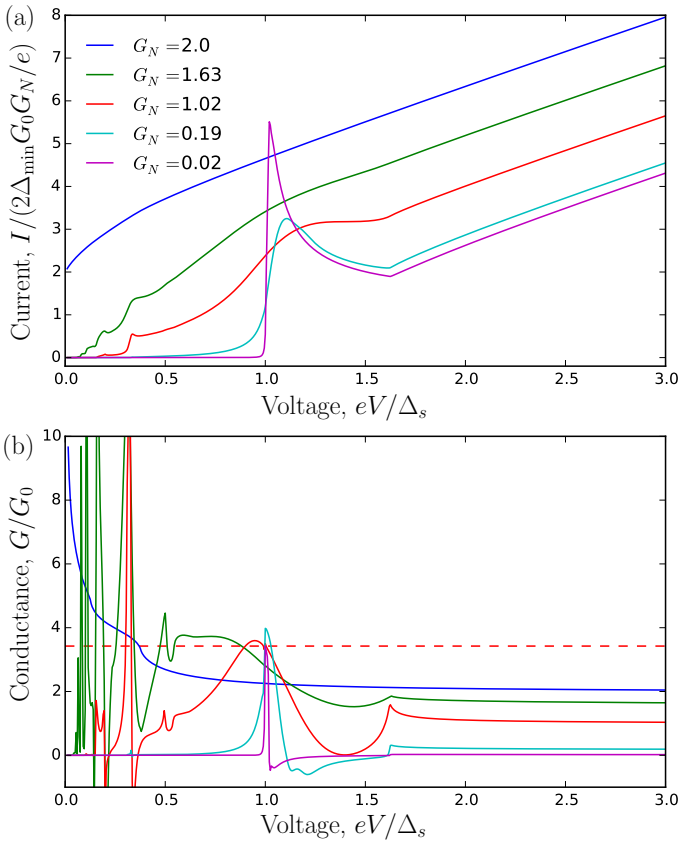

Figure 3.7: Plots of (a) dc current I and (b) normalized differential conductance G/G_0 versus bias voltage V for an sNp_2 junction with various values of transparencies G_N. The red dashed line $[2G_M = (4-\pi)4e^2/h]$ is the conductance value due to single Andreev reflections from two MZMs. The parameters used for the sSC are $\mu_s = 20$ K and $\Delta_s = 0.01$ K. The parameters used for the p_2-SC are $\mu_p = 20$ K, $V_Z = 0$ K, $\Delta_p = 2 \times 10^{-4}$ eVÅ, where the gap is $\Delta_{p_2} = 6.3 \times 10^{-3}$ K. The smallest gap in the junction is $\Delta_{\min} = \Delta_{p_2} = 6.3 \times 10^{-3}$ K.

the threshold voltage $e|V| = \Delta_s$ due to single Andreev reflections from the Majorana Kramers pair with each single Andreev reflection from the MZM contributing a conductance of G_M. For large or intermediate transparencies, due to MAR the conductance at $e|V| = \Delta_s$ is no longer quantized at $2G_M$ and there is an SGS in the current and conductance profile. In contrast to the sNp_1 junction where the current and conductance is zero near zero voltage, when the transparency is not small the

current and conductance for the sNp_2 junction is non-zero near zero voltage. This is because unlike the case of the sNp_1 junction where there is only one MZM which facilitates the spin-triplet Andreev reflections in one spin channel, there are two MZMs in sNp_2 junctions facilitating Andreev reflections in two different spin channels. As a result, the MAR are not suppressed near zero voltage. The SGS associated with MAR develops at specific voltages as given in Table 3.1. Similar to the conventional s-wave superconductor–normal–s-wave superconductor junction [76, 80, 81], in the perfectly transparent limit ($G_N = 2$), the current at small voltages for the sNp_2 junction asymptotically approaches

$$I(V \to 0) = \frac{4e\,\Delta_{\min}}{h}, \tag{3.12}$$

which corresponds to the transfer of a charge of $2e$ across the junction where $\Delta_{\min} = \min(\Delta_s, \Delta_{p_2})$ is the smallest gap in the junction.

3.3.4 p_2Np_2 junction

For the p_2Np_2 junction, both superconductors have two topological channels with two MZMs at each end. The plots of the current and conductance for this junction are depicted in Fig. 3.8. In the perfectly transparent limit ($G_N = 2$), the current at small voltages asymptotically approaches $I(V \to 0) = 4e\Delta_{\min}/h$, where $\Delta_{\min}$ is the smallest gap in the junction. This asymptote value of the dc current is the same as the value obtained for the conventional s-wave-normal-s-wave superconductor junction [76, 80, 81]. As $V \to 0$, the current in the p_2Np_2 junction

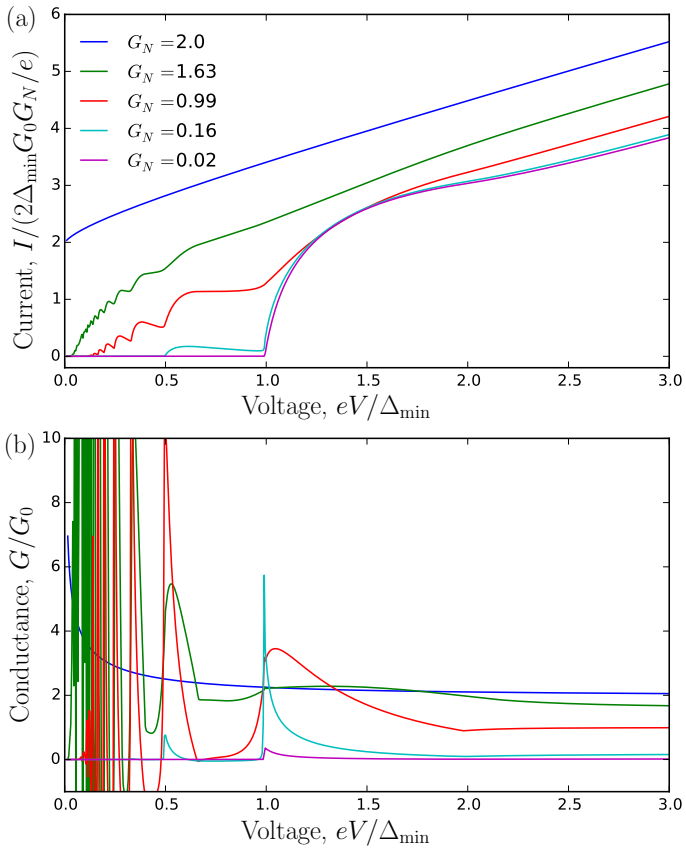

Figure 3.8: Plots of (a) dc current I and (b) normalized differential conductance G/G_0 versus bias voltage V for a p_2Np_2 junction with various values of transparencies G_N. The parameters used for both p_2-SCs are $\mu_p = 20$ K, $V_Z = 0$ K, $\Delta_p = 2 \times 10^{-4}$ eVÅ, where the gap is $\Delta_{p_2} = 6.3 \times 10^{-3}$ K. The smallest gap in the junction is $\Delta_{\min} = 6.3 \times 10^{-3}$ K.

is transferred via a Majorana Kramers pair where each of the MZMs transfers a charge of unit e giving a total charge of $2e$, the same total amount of charge as that carried by a Cooper pair. As a result, the current $I(V \to 0)$ is the same as that for the conventional SNS junction [76, 81, 83]. For not-perfectly transparent junctions ($G_N \neq 2$), the dc current approaches zero as the voltage approaches zero.

The SGS associated with the MAR develops at specific voltages given in Table 3.1 where for the p_2Np_2 junction with symmetric gaps, the voltage is $|V| =$

Δ_{p_2}/en ($n = 1, 2, 3, \cdots$) (see Fig. 3.8). The SGS is suppressed in the tunneling limit and the current becomes non-zero only when the voltage is above the threshold voltage $|V| = \Delta_{p_2}/e$, i.e., when the quasiparticles have sufficient energy to undergo single Andreev reflections from the MZM. This is contrary to the case of the junction between two-nontopological superconductors where the tunneling current can flow only when the voltage is above $|V| = 2\Delta/e$, i.e., when the gap edge of the unoccupied band lines up with that of the occupied band. Since the p_2-SC does not have a BCS singularity, the conductance at $|V| = \Delta_{p_2}/e$ in the tunneling limit is not quantized at G_M. Instead, it has a nonuniversal value which decreases with decreasing junction transparency.

3.3.5 p_2Np_1 junction

For the p_2Np_1 junction in the perfectly transparent limit ($G_N = 1$), the current near zero voltage approaches $I(V \to 0) = 2e\Delta_{\min}/h$, which is half of the current for the p_2Np_2 or s-wave superconductor$-$normal metal$-$$s$-wave superconductor junction. The reason is that the p_1-SC has only one MZM which can transfer a charge in the unit of e in one spin channel. The SGS appears at voltages given in Table 3.1. Since the p_2Np_1 junction considered here has asymmetric gap, the current and conductance in the weak-tunneling limit develop jumps at the voltages $|V| = \Delta_{p_1}/e$ and $|V| = \Delta_{p_2}/e$ which correspond to the conductances due to single Andreev reflections from the MZM in the p_2-SC and p_1-SC, respectively. The conductance values at these jumps have non-universal values which decrease with the junction

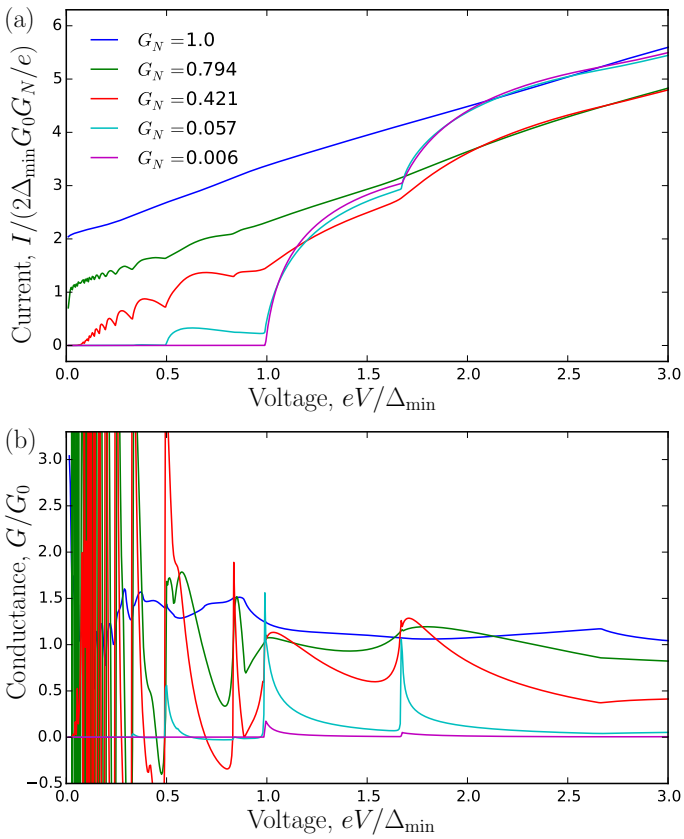

Figure 3.9: Plots of (a) dc current I and (b) normalized differential conductance G/G_0 versus bias voltage V for a p_2Np_1 junction with various values of transparencies G_N. The parameters used for the p_1-SC are $\mu_p = 20$ K, $\Delta_p = 2 \times 10^{-4}$ eVÅ, and $V_Z = 40$ K where the gap is $\Delta_{p_1} = 0.011$ K. The parameters for the p_2-SC are $\mu_p = 20$ K, $\Delta_p = 2 \times 10^{-4}$ eVÅ, $V_Z = 0$ K, where the gap is $\Delta_{p_2} = 6.3 \times 10^{-3}$ K. The smallest gap in the junction is $\Delta_{\min} = 6.3 \times 10^{-3}$ K.

transparency.

3.3.6 p_1Np_1 junction

Fig. 3.10 displays the current and conductance plots for a p_1Np_1 junction. Similar to the p_2Np_1 junction, for a perfectly transparent p_1Np_1 junction ($G_N = 1$) the current at small voltages asymptotically approaches $I(V \to 0) = 2e\Delta_{\min}/h$. This is due to the fact that a charge of e is transferred between the MZMs on both

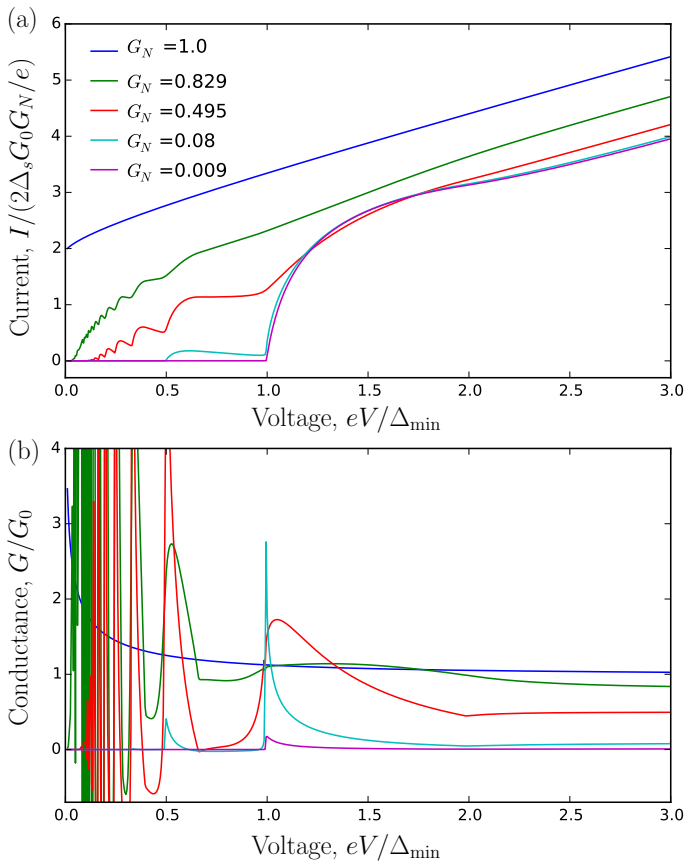

Figure 3.10: Plots of (a) dc current I and (b) normalized differential conductance G/G_0 versus bias voltage V for a p_1Np_1 junction with various values of transparencies G_N. The parameters used for both p_1-SCs are $\mu_p = 20$ K, $\Delta_p = 2 \times 10^{-4}$ eVÅ, and $V_Z = 40$ K where the gap is $\Delta_{p_1} = 0.011$ K. The smallest gap in the junction is $\Delta_{\min} = \Delta_{p_1} = 0.011$ K.

sides of the junction. For a symmetric p_1Np_1 as considered here, the SGS develops at voltages $|V| = \Delta_{p_1}/ne$. In the weak-tunneling limit, there is a step jump in the conductance at $|V| = \Delta_{p_1}/e$ to a non-universal value which decreases as the junction transparency decreases.

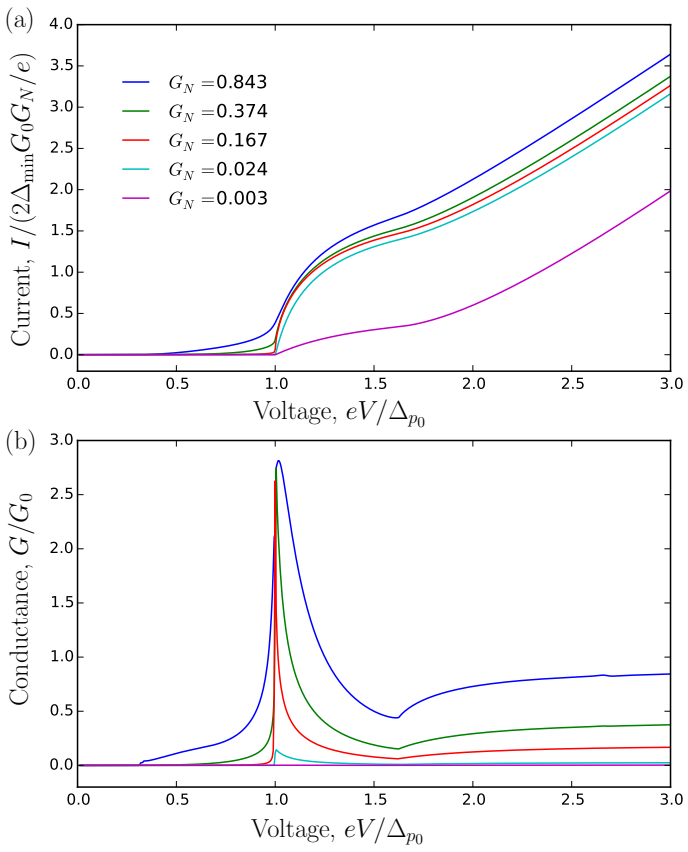

Figure 3.11: Plots of (a) dc current I and (b) normalized differential conductance G/G_0 versus bias voltage V for a p_0Np_2 junction with various values of transparencies G_N. The parameters used for the p_0-SC are $\mu_p = -0.01$ K, $V_Z = 0$ K, $\Delta_p = 0.2$ eVÅ, where the gap is $\Delta_{p_0} = 0.01$ K. The parameters used for the p_2-SC are $\mu_p = 20$ K, $V_Z = 0$ K, $\Delta_p = 2\times10^{-4}$ eVÅ, where the gap is $\Delta_{p_2} = 6.3\times10^{-3}$ K. The smallest gap in the junction is $\Delta_{\min} = 6.3 \times 10^{-3}$ K.

3.3.7 p_0Np_2 junction

The current and conductance plots for the p_0Np_2 junction are given in Fig. 3.11. The MAR peaks for this junction are suppressed since p_0 is essentially an insulator. There is a conductance peak at $|V| = \Delta_{p_0}/e$ which corresponds to single Andreev reflections from the MZMs. However, unlike the case of the sNp_2 junction, the tunneling conductance at the threshold voltage $|V| = \Delta_{p_0}/e$ assumes a non-quantized

value which decreases with decreasing junction transparency. We note that the MZM tunneling conductance quantization $G_M = (4-\pi)2e^2/h$ holds only if the superconducting probe has a BCS singularity (as derived in Sec. 1.3.2.1).

3.3.8 p_0Np_1 junction

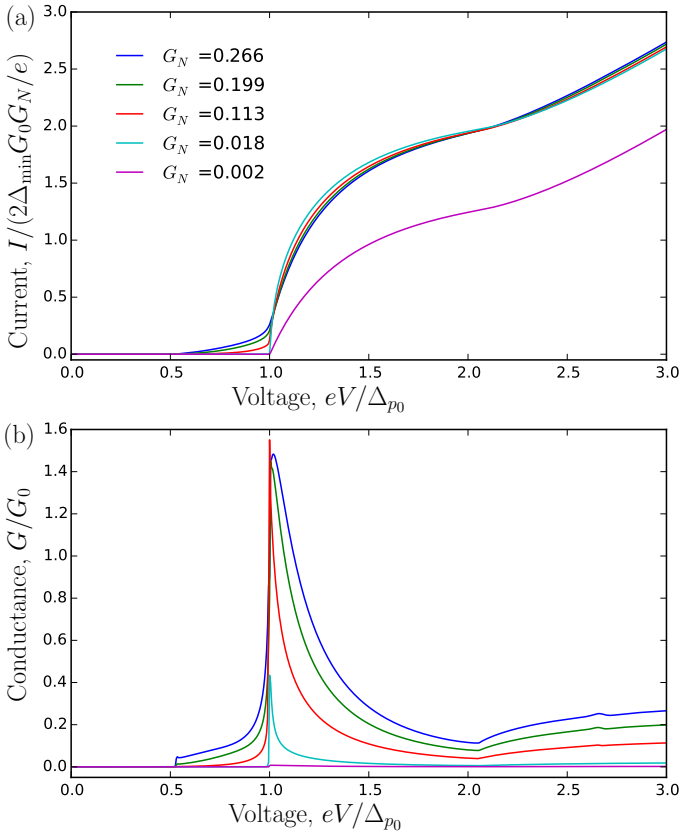

Figure 3.12: Plots of (a) dc current I and (b) normalized differential conductance G/G_0 versus bias voltage V for a p_0Np_1 junction with various values of transparencies G_N. The parameters used for the p_0-SC are $\mu_p = -0.01$ K, $V_Z = 0$ K, $\Delta_p = 0.2$ eVÅ, where the gap is $\Delta_{p_0} = 0.01$ K. The parameters used for the p_1-SC are $\mu_p = 20$ K, $V_Z = 40$ K, $\Delta_p = 2 \times 10^{-4}$ eVÅ, where the gap is $\Delta_{p_1} = 0.011$ K. The smallest gap in the junction is $\Delta_{\min} = 0.01$ K.

The current and conductance plots for the p_0Np_1 junction are given in Fig. 3.12. The conductance for this junction looks similar to those of the p_0Np_2 junction. The

MAR peaks for this junction are suppressed and in the tunneling limit, the conductance has a step jump at the threshold voltage $e|V| = \Delta_{p_0}$ to a non-quantized value which decreases with decreasing junction transparency.

3.3.9 p_0Np_0 junction

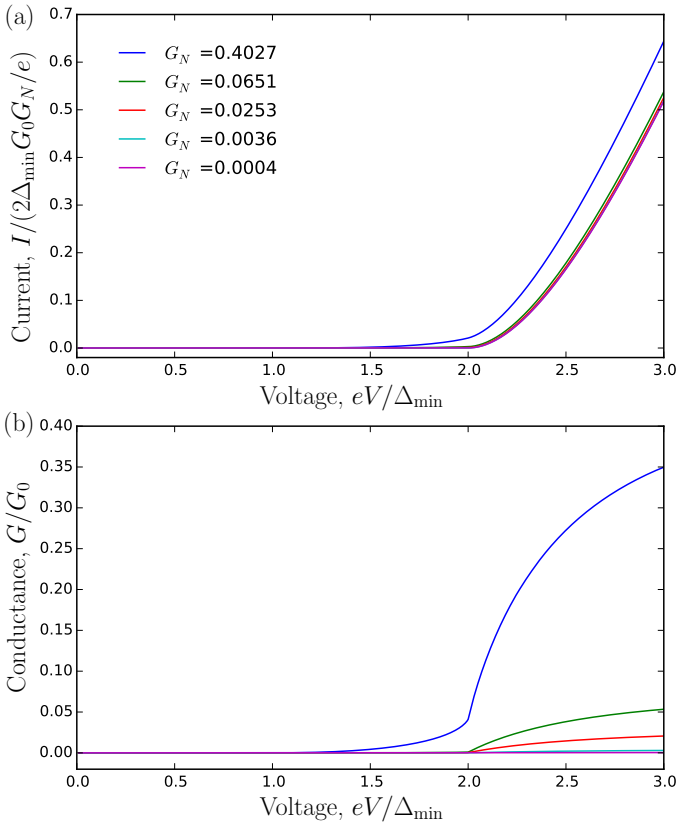

Figure 3.13: Plots of (a) dc current I and (b) normalized differential conductance G/G_0 versus bias voltage V for a p_0Np_0 junction with various values of transparencies G_N. The parameters used for both p_0-SCs are $\mu_p = -0.01$ K, $V_Z = 0$ K, $\Delta_p = 0.2$ eVÅ, where the gap is $\Delta_{p_0} = 0.01$ K. The smallest gap in the junction is $\Delta_{\min} = 0.01$ K.

For the p_0Np_0 junction, the plots of the current and conductance versus the bias voltage are displayed in Fig. 3.13. Since the p_0Np_0 junction is essentially a

junction between two insulators, the current and conductance for this junction are generally small and the MAR peaks are strongly suppressed. In the limit of small transparencies, the current and conductance for a symmetric p_0Np_0 junction have a jump to a non-zero value at $e|V| = 2\Delta_{p_0}$, i.e., when the density-of-state singularity of the occupied band of one p_0-SC is aligned with the singularity of the empty band of the other p_0-SC.

3.4 Spin-Orbit-Coupled Superconducting Wire Junctions

The BdG Hamiltonian for the SOCSW is

$$\mathcal{H}_{\text{SOCSW}} = \left(-\frac{\hbar^2\partial_x^2}{2m} - \mu_0\right)\tau_z - i\alpha\partial_x\tau_z\sigma_y + V_Z\sigma_x + \Delta_0\tau_x, \tag{3.13}$$

where μ_0 is the chemical potential of the nanowire, α is the strength of the SOC, V_Z is the Zeeman field, and Δ_0 is the proximity-induced s-wave pairing potential. The Hamiltonian above is written in the same basis as that in Eq. (3.10). The SOCSW can be tuned from the nontopological to the topological regime by simply changing the Zeeman field V_Z or chemical potential μ_0. The critical value $V_Z = \sqrt{\mu_0^2 + \Delta_0^2}$ marks the TQPT between the topologically trivial ($V_Z < \sqrt{\mu_0^2 + \Delta_0^2}$) and topologically nontrivial phase ($V_Z > \sqrt{\mu_0^2 + \Delta_0^2}$). In the topological regime, there is one MZM at each end of the nanowire. The BdG spectrum of the SOCSW is given in Fig. 3.14. In what follows, we are going to denote the minimum gap in the SOCSW spectrum by Δ_{SOCSW}. Now, let us look at the current and conductance of several SNS junctions between two SOCSWs where the SOCSW can be either in

the nontopological or topological regime.

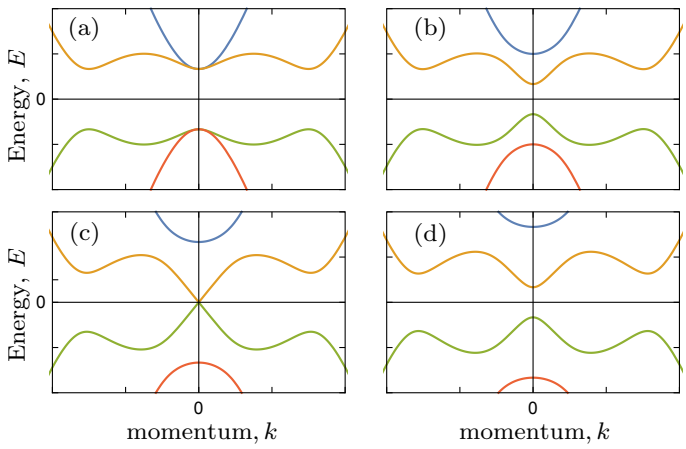

Figure 3.14: Energy spectrum of SOCSW for different parameter regimes: (a) $V_Z = 0$ (nontopological), (b) $V_Z < \sqrt{\mu_0^2 + \Delta_0^2}$ (nontopological), (c) $V_Z = \sqrt{\mu_0^2 + \Delta_0^2}$ (transition), (d) $V_Z > \sqrt{\mu_0^2 + \Delta_0^2}$ (topological).

3.4.1 Nontopological–Nontopological SOCSW Junction

In this subsection, we consider the junction between two SOCSWs where both of them are in the nontopological regime (i.e., $V_Z < \sqrt{\mu_0^2 + \Delta_0^2}$). As shown in Fig. 3.15, the current and conductance of this junction with no Zeeman field ($V_Z = 0$) is the same as that of an s-wave superconductor–normal metal–s-wave superconductor junction [76, 80, 81]. The SGS for the symmetric nontopological–nontopological SOCSW junction occurs at voltages $|V| = 2\Delta_{\mathrm{SOCSW}}^{\mathrm{nontopo}}/ne$ where $n = 1, 2, 3, \cdots$. For a perfectly transparent junction ($G_N = 2$), the current at small voltages approaches the value

$$I(V \to 0) = \frac{4e\Delta_{\mathrm{min}}}{h}. \tag{3.14}$$

In the limit of small transparency the current and conductance develop a step jump at $|V| = 2\Delta_{\mathrm{SOCSW}}^{\mathrm{nontopo}}/e$ for junctions with symmetric gaps.

Fig. 3.16 shows the current and conductance for the nontopological–nontopological SOCSW junction in the presence of Zeeman field. Increasing the Zeeman field smooths out the SGS. In the limit of small transparencies, the conductance has a smooth rise from zero instead of a step jump at the threshold voltage.

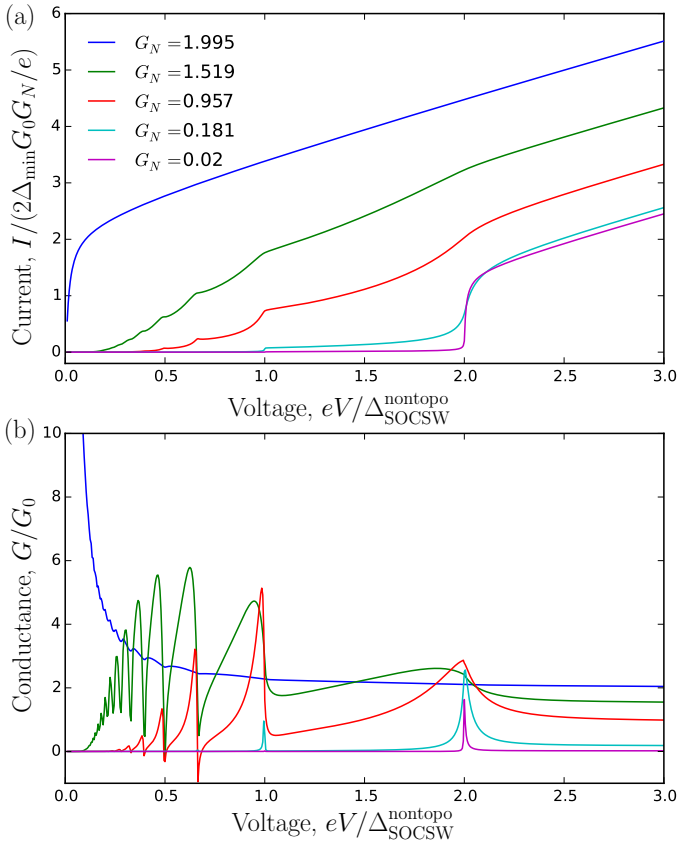

Figure 3.15: Plots of (a) dc current I and (b) normalized differential conductance G/G_0 versus bias voltage V for a nontopological–nontopological SOCSW junction with various values of transparencies G_N and no Zeeman field. The parameters used for both SOCSWs are $\mu_0 = 0$ K, $V_Z = 0$ K, $\Delta_0 = 0.01$ K, $\alpha = 0.5$ eVÅ, where the gap is $\Delta_{\mathrm{SOCSW}}^{\mathrm{nontopo}} = 0.01$ K. The smallest gap in the junction is $\Delta_{\mathrm{min}} = 0.01$ K.

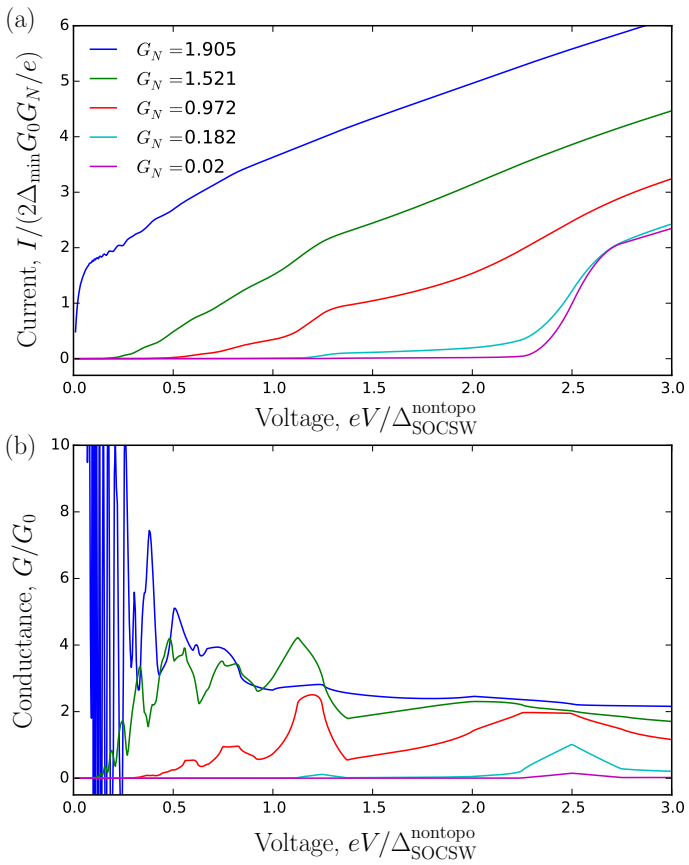

Figure 3.16: Plots of (a) dc current I and (b) normalized differential conductance G/G_0 versus bias voltage V for a nontopological–nontopological SOCSW junction with various values of transparencies G_N and finite Zeeman field. The parameters used for both SOCSWs are $\mu_0 = 0$ K, $V_Z = 0.002$ K, $\Delta_0 = 0.01$ K, $\alpha = 0.5$ eVÅ, where the gap is $\Delta^{\rm nontopo}_{\rm SOCSW} = 0.008$ K. The smallest gap in the junction is $\Delta_{\rm min} = 0.008$ K.

3.4.2 Nontopological–Topological SOCSW junction

Here, we consider the junction between a nontopological and a topological SOCSW. The current and conductance for this junction are given in Figs. 3.17-3.19. Let us first consider the case of the junction with the nontopological SOCSW having no Zeeman field where the energy spectrum for this nontopological SOCSW has the minimum gap at the Fermi momentum with a BCS singularity [as shown

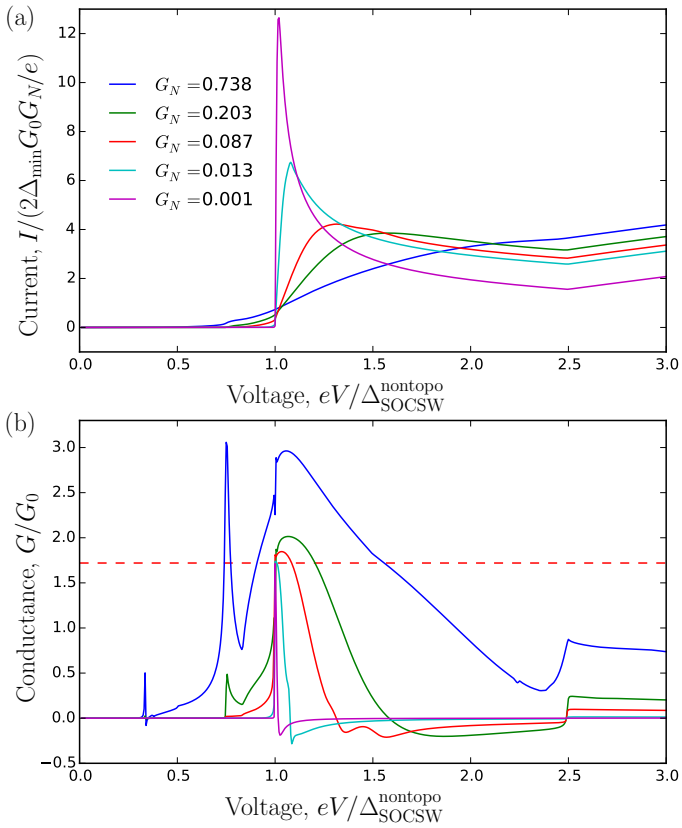

Figure 3.17: Plots of (a) dc current I and (b) normalized differential conductance G/G_0 versus bias voltage V for a nontopological–topological SOCSW junction with various values of transparencies G_N. The red dashed line [$G_M = (4-\pi)2e^2/h$] is the conductance value due to single Andreev reflections from the MZM. The nontopological SOCSW is not subjected to any Zeeman field and the topological superconductor has a small Zeeman field. The parameters used for the nontopological SOCSW are $\mu_0 = 0$ K, $V_Z = 0$ K, $\Delta_0 = 0.5$ K, $\alpha = 0.5$ eVÅ where $\Delta^{\rm nontopo}_{\rm SOCSW} = 0.5$ K. The parameters used for the topological SOCSW are $\mu_0 = 0$ K, $V_Z = 15.0$ K, $\Delta_0 = 10.0$ K, $\alpha = 0.05$ eVÅ, where the gap is $\Delta^{\rm topo}_{\rm SOCSW} = 0.75$ K. The smallest gap in the junction is $\Delta_{\rm min} = 0.5$ K.

in Fig. 3.14(a)]. For this case, the the conductance in the tunneling limit for this junction develops a step jump from 0 to $G_M = (4-\pi)2e^2/h$ at the gap-bias voltage $e|V| = \Delta^{\rm nontopo}_{\rm SOCSW}$ similar to the case of sNp_1 junction (as shown in Figs. 3.17 and 3.18). This quantized value G_M is due to single Andreev reflections from the MZM

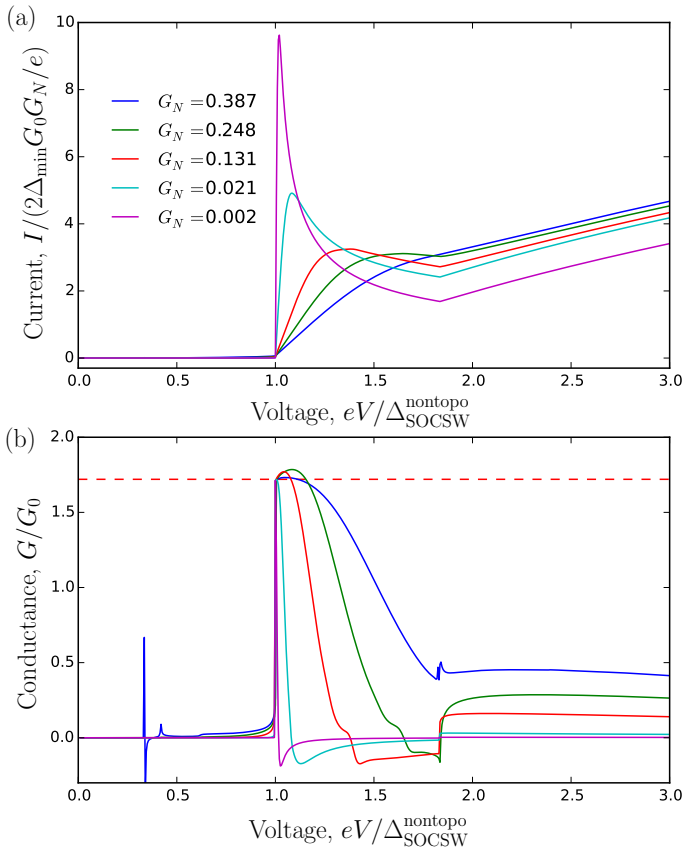

Figure 3.18: Plots of (a) dc current I and (b) normalized differential conductance G/G_0 versus bias voltage V for a nontopological–topological SOCSW junction with various values of transparencies G_N. The red dashed line [$G_M = (4-\pi)2e^2/h$] is the conductance value due to single Andreev reflections from the MZM. The nontopological SOCSW is not subjected to any Zeeman field and the topological superconductor has a large Zeeman field. The parameters used for the nontopological SOCSW are $\mu_0 = 0$ K, $V_Z = 0$ K, $\Delta_0 = 0.5$ K, $\alpha = 0.5$ eVÅ where $\Delta_{\rm SOCSW}^{\rm nontopo} = 0.5$ K. The parameters used for the topological SOCSW are $\mu_0 = 0$ K, $V_Z = 60.0$ K, $\Delta_0 = 10.0$ K, $\alpha = 0.05$ eVÅ, where the gap is $\Delta_{\rm SOCSW}^{\rm topo} = 0.42$ K. The smallest gap in the junction is $\Delta_{\min} = 0.42$ K.

of an electron coming from the gap edge with BCS singularity. In the limit where the Zeeman field in the topological SOCSW is small, for intermediate and large transparencies, there are MAR peaks and the conductance below the voltage $e|V| = \Delta_{\rm SOCSW}^{\rm nontopo}$ is nonzero except for small voltages (see Fig. 3.17). Near zero voltage, the

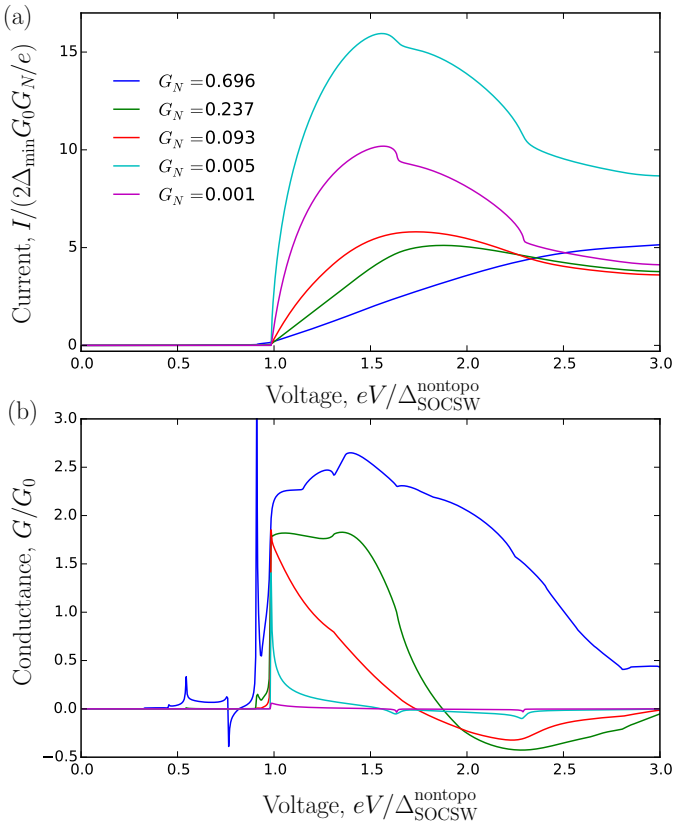

Figure 3.19: Plots of (a) dc current I and (b) normalized differential conductance G/G_0 versus bias voltage V for a nontopological–topological SOCSW junction with various values of transparencies G_N. The nontopological SOCSW has a finite Zeeman field and the topological superconductor has a small Zeeman field. The parameters used for the nontopological SOCSW are $\mu_0 = 0$ K, $V_Z = 0.2$ K, $\Delta_0 = 0.5$ K, $\alpha = 0.5$ eVÅ where $\Delta_{\rm SOCSW}^{\rm nontopo} = 0.3$ K. The parameters used for the topological SOCSW are $\mu_0 = 0$ K, $V_Z = 15.0$ K, $\Delta_0 = 10.0$ K, $\alpha = 0.05$ eVÅ, where the gap is $\Delta_{\rm SOCSW}^{\rm topo} = 0.75$ K. The smallest gap in the junction is $\Delta_{\rm min} = 0.3$ K. Inset: The zoom-in version of the conductance near $eV = \Delta_{\rm SOCSW}^{\rm nontopo}$.

current and conductance vanish due to the difference in the Andreev-reflection spin selectivity of the SOCSW and the MZM. In the limit of large Zeeman field in the topological SOCSW where MAR are suppressed and single Andreev reflections are allowed, the conductance for this junction develops a step jump from 0 to $G_M = (4 - \pi)2e^2/h$ independent of the junction transparency. We note that this result

is similar to the case where the nontopological SOCSW is replaced by an s-wave superconductor [57].

For the case where there is Zeeman field in the nontopological superconductor, the gap edge of the superconductor no longer has the BCS singularity. As a result, the MZM tunneling conductance measured using this nontopological superconductor will *not* be quantized at G_M for the gap-bias voltage $e|V| = \Delta_{\mathrm{SOCSW}}^{\mathrm{nontopo}}$. Instead, the tunneling conductance assumes a non-universal value which decreases with decreasing junction transparency as shown in Fig. 3.19.

3.4.3 Topological–Topological SOCSW junction

The current and conductance plots for a topological–topological SOCSW junction are shown in Fig. 3.20. Our results, calculated using the scattering matrix formalism, for this junction is the same as the results calculated using the Green's function method [84]. Similar to the p_1Np_1 junction, in the limit of perfect transparency ($G_N = 1$), the current for a topological–topological SOCSW junction asymptotically approaches

$$I(V \to 0) = 2e\Delta_{\mathrm{min}}/h, \tag{3.15}$$

which is half the value of the current in the conventional SNS junction. The SGS for this junction happens at voltages $|V| = \Delta_{\mathrm{min}}/ne$. In the weak tunneling limit, there is a step jump in the conductance at $|V| = \Delta_{\mathrm{min}}/e$. We note, however, that the conductance at the voltage $|V| = \Delta_{\mathrm{min}}/e$ is not quantized at $G_M = (4-\pi)2e^2/h$.

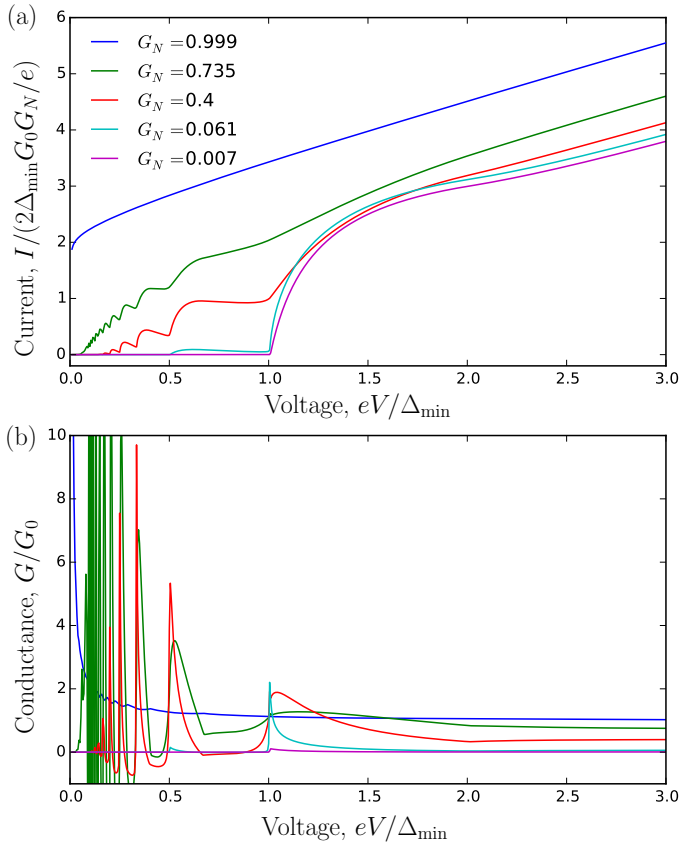

Figure 3.20: Plots of (a) dc current I and (b) normalized differential conductance G/G_0 versus bias voltage V for a topological–topological SOCSW junction with various values of transparencies G_N. The parameters used for both SOCSWs are $\mu_0 = 0$ K, $V_Z = 15$ K, $\Delta_0 = 1.17$ K, $\alpha = 0.05$ eVÅ, where the gap is $\Delta^{\text{topo}}_{\text{SOCSW}} = 0.01$ K. The smallest gap in the junction is $\Delta_{\min} = 0.01$ K.

3.5 Andreev Bound States

Let us compare the conductance of an MZM with that of an ABS. In particular, here we consider the ABS that may arise in the SOCSW model with a finite topological region and a semi-infinite nontopological region as shown in the right side of the SNS junction in Fig. 3.21(a). This model can happen naturally in an SOCSW with varying chemical potential where the chemical potential varies from the topological regime to the non-topological regime resulting in the domain walls

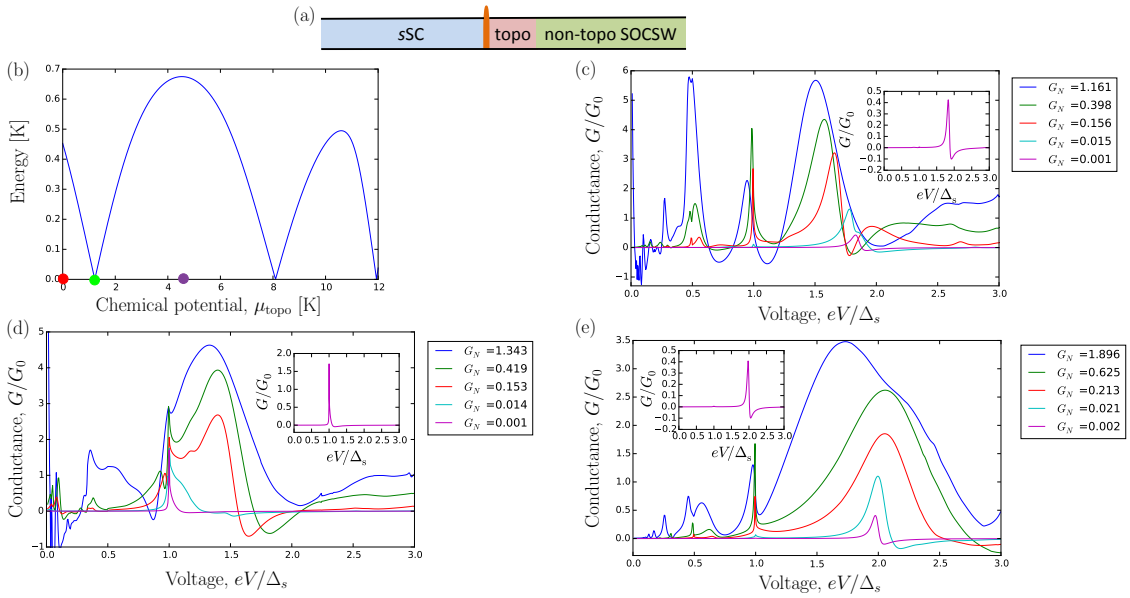

Figure 3.21: (a) Schematic diagram of an sSC–SOCSW junction with a pair of ABS (one at each end of the topological region). The chemical potential of the topological and nontopological regions are $|\mu_{\rm topo}| < \sqrt{V_Z^2 - \Delta_0^2}$ and $|\mu_{\rm nontopo}| > \sqrt{V_Z^2 - \Delta_0^2}$, respectively. The parameters used for the sSC are $\mu_s = 50$ K, and $\Delta_s = 0.67$ K. The SOCSW parameters are $\mu_{\rm nontopo} = 211.18$ K, $V_Z = 15$ K, $\Delta_0 = 10$ K, $\alpha = 0.05$ eVÅ, and length of the topological region, $L_{\rm topo} = 0.6$ μm. We use a dissipation term $i\Gamma\tau_0 \otimes \sigma_0$ in the BdG Hamiltonian of both the left and right superconductors with a dissipation strength $\Gamma = 0.05$K to broaden the Van Hove singularity. (b) The energy of the Andreev bound state closest to zero energy versus the chemical potential $\mu_{\rm topo}$ in the topological region. The red, green and purple dots indicate the value of the topological chemical potential used in (c),(d), and (e), respectively. Normalized differential conductance G/G_0 for the SOCSW for several chemical potential values in the topological region: (c) $\mu_{\rm topo} = 0$ K, (d) $\mu_{\rm topo} = 1.697$ K, and (e) $\mu_{\rm topo} = 4.5$ K. Inset: the ABS conductance in the weak tunneling limit which is the conductance for the smallest transparency in the main plot.

between the topological and non-topological regions [85]. The ABSs can be found at the end of the topological region. For simplicity, here we consider a step jump in the chemical potential in going from the topologically nontrivial ($|\mu_0| < \sqrt{V_Z^2 - \Delta_0^2}$) to the topologically trivial value ($|\mu_0| > \sqrt{V_Z^2 - \Delta_0^2}$) keeping all the other parameters in these two regions to be the same. The ABS closest to zero energy in this model has its energy oscillating with the chemical potential in the topological region as shown in Fig. 3.21(b) where the zero-energy ABS can be found at specific values of parameters [74].

Let us look at the conductance of this SOCSW model measured using an s-wave superconducting lead. To calculate the conductance, we first introduce a dissipation term $-i\Gamma\tau_0 \otimes \sigma_0$ into the BdG Hamiltonian. The dissipation term is used to broaden the van Hove singularity of the BdG spectrum so that we do not need to use a very fine energy grid in the numerical calculation. This dissipation term has been used in Refs. [86, 87] to calculate conductance in topological NS junctions, though for different reasons. Our using a dissipation here could either be physically motivated as in Ref. [87] or simply a technical artifice in handling the van Hove singularity. Figs. 3.21(c)-(e) show the conductance of the SOCSW calculated for several chemical potential values in the topological region with all other parameters being the same. The conductance for the zero-energy ABS may resemble the MZM tunneling conductance, i.e., it has a sharp rise at the voltage $e|V| = \Delta_s$ to a peak with a value near $G_M = (4-\pi)2e^2/h$ (see the inset in Fig. 3.21(d) or Ref. [57]). For non-zero energy ABS, the ABS tunneling conductance peak shifts away from the threshold voltage $e|V| = \Delta_s$ (where Δ_s is the s-wave superconducting gap) towards

a larger voltage value by the ABS energy normalized by the tunnel coupling between the lead and the system [see Fig. 3.21(c) and (e)].

3.6 Conclusion

In this chapter, we have calculated the zero-temperature dc current and conductance in various 1D voltage-biased SNS junctions involving topological and nontopological superconductors, considering both ideal spinful p-wave and realistic spin-orbit-coupled s-wave superconducting wires. For junctions with small transparencies, the presence of an MZM gives rise to a jump in the current and conductance at the gap-bias voltage $e|V| = \Delta_{\text{lead}}$ where the superconducting gap edge is aligned with the MZM. If the superconducting lead has a BCS singularity at the gap edge then the tunneling conductance at the gap-bias voltage takes the value $G_M = (4-\pi)2e^2/h$ due to a single Andreev reflection from the MZM. However, this quantization no longer holds if the superconducting lead gap edge does not have the BCS singularity, e.g., p-wave superconductor or SOCSW with finite magnetic field. For SNS junctions where both of the superconductors are topological (i.e., with one or two MZMs at each end), there is SGS in the I-V curve or conductance profile due to MAR. However, for nontopological–topological superconductor junctions where the topological superconductor has only one MZM at each end, the SGS at small voltages is suppressed due to the mismatch in Andreev reflection spin-selectivity of the superconducting lead and the MZM.

In contrast to the conventional SNS junction where Cooper pairs are trans-

ferred across the junction with a charge of $2e$, for the topological SNS junction, the charge is transferred via the MZM in the units of e. As a result, for a perfectly transparent junction with an MZM at each end, the MZM contributes to a near zero-voltage current $I(V \to 0) = 2e\Delta_{\min}/h$ where $\Delta_{\min}$ is the smallest gap in the junction. We note that this MZM near-zero voltage current is by no means universal or quantized because of the generic presence of the gap $\Delta_{\min}$ which surely varies from junction to junction. The same is also true for the case where there are two MZMs on one side and one MZM on the other side. This near zero-voltage dc current is half of the value for the conventional s-wave superconductor–normal–s-wave superconductor junction. However, for the case where there are two MZMs on both sides of the junction, the near zero-voltage current is $I(V \to 0) = 4e\Delta_{\min}/h$ because each MZM can exchange a charge of e between each other. For the case where there is a conventional s-wave superconductor on one side and one MZM on the other side of the junction, the current is zero because of the difference in the Andreev-reflection spin selectivity of the s-wave superconductor and MZM, i.e., the s-wave superconductor allows only opposite-spin Andreev reflections and MZM favors equal-spin Andreev reflections. However, for the junction between a conventional s-wave superconductor and a Majorana Kramers pair the near-zero current for a perfect transparent junction is not zero but it is $I(V \to 0) = 4e\Delta_{\min}/h$. This is due to the fact that the MZM pair can facilitate Andreev reflections in both spin channels.

We also calculated the conductance with an ABS in the SOCSW model arising from a finite topological and a semi-infinite non-topological region. For this junction,

the energy of the ABS closest to zero energy oscillates with the chemical potential in the topological region. For the parameters where the ABS is at zero energy, the tunneling conductance may resemble that of Majorana, i.e., it has a step jump to a value G_M at the gap-bias voltage $e|V| = \Delta_{\text{lead}}$. However, when the energy of the ABS is non-zero, the conductance peak shifts away from the gap-bias voltage towards a larger voltage value by the ABS energy.

Chapter 4

Gap Closing and Topological Quantum Phase Transition

Besides conductance spectroscopy, detecting the collapse and reopening of the bulk gap as the Zeeman field is varied will also provide a strong signature for the TQPT which marks the beginning of the topological phase. In this chapter, we will propose a dynamical scheme to detect the TQPT which is particularly suited for cold atomic systems. This chapter is based on Ref. [59] and the figures in this chapter are adapted from the same reference.

We begin by reviewing the Raman scheme used to realize the SOC in ultracold atomic settings. We then proceed to discuss our "dip-in dip-out" protocol to detect the TQPT. In this protocol, the system is first prepared in its long-lived conventional phases and then driven into the topological phases and back. We will apply this scheme to the 1D spin-orbit-coupled Fermi gases (SOCFGs) with attractive interactions whose Hamiltonian is the same as that of SOCSW [see Eq. (3.13)]. Finally, we show that the Stuckelberg oscillation and Kibble-Zurek (KZ) scaling of the excitation's momentum distribution after the quench protocol can serve as a robust signature of the TQPT.

4.1 Raman-Induced Spin-Orbit Coupling

The SOC, which associates a particle's momentum to its spin, can be engineered in ultracold atoms by using the two-photon Raman process [88, 89, 90, 91, 92]. This Raman scattering couples two internal states of an atom (which are denoted here by pseudospin $|\uparrow\rangle$ and $|\downarrow\rangle$) to the motion of the atom via the absorption of a photon from one laser beam and a stimulated reemission into another laser beam [see Fig. 4.1]. For a counter-propagating laser beam where each photon carries a momentum of $k_r = h/\lambda_r$, this process imparts a momentum of $2\hbar k_r$ to the atom when its state is changed from one pseudospin to the other and an opposite momentum when the state is changed in the reverse way. In this way, this Raman process effectively generates the SOC term, which is an essential ingredient for realizing the topological phases.

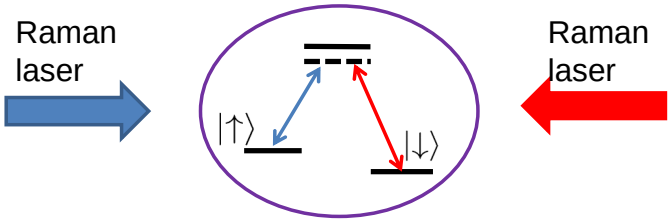

Figure 4.1: Schematic diagram of Raman-induced spin-orbit coupling: a pair of counter-propagating laser couples together two internal atomic states which are here labeled by $|\uparrow\rangle$ and $|\downarrow\rangle$.

This scheme was first used by Spielman's group to engineer the SOC in ^{87}Rb Bose-Einsten condensates [93]. It was subsequently implemented in the ^{6}Li [94] and ^{40}K [95] Fermi gases. This Raman scheme, however, suffers from the heating effect due to off-resonant light scattering, i.e., the spontaneous emission. As a result, the

topological phases realized using this scheme have short lifetimes.

4.2 Dip-in Dip-out Protocol

We propose a dynamical solution to the problem of studying the short-lived topological phase by starting the system in its long-lived nontopological phase and driving it into the topological phase and back. The rapid nature of this process obviates heating; this is expected to make our proposal easily implementable in experiments. The process involves crossing the TQPT between the phases, which supports gapless excitations. Driving through the gapless phase transition produces excitations in the gapped phase via the Landau-Zener (LZ) transitions [96, 97] with a defect density that demonstrates KZ scaling [98, 99, 100, 101, 102, 103, 104, 105, 106, 107]. More interestingly, our dip-in-dip-out strategy, where the system is driven through the phase transition and back, leads to the Stückelberg interference phenomenon [108, 109] between the two LZ transitions, which in turn results in oscillations of the momentum and energy distribution of the excitations with the ramp rate. In many cases the unique ramp-rate dependence of the excitations' momentum distributions can be measured via standard time-of-flight techniques. This provides an experimentally viable test for the dynamical fingerprints of TQPT, whose equilibrium properties would otherwise be hard to access.

While this general idea applies to many phase transitions in ultracold bosonic and fermionic systems [105, 110, 111, 112], we focus on phase transitions whose dynamical properties are well understood [112, 113, 114, 115, 116, 117, 118, 119, 120,

121, 122, 123]. In particular, we apply this idea to the 1D topological superfluids (TSFs) [113, 114, 115] in systems of ultracold atoms which host the Majorana modes.

4.3 Time-Dependent Bogoliubov-de Gennes Equation

We study 1D fermionic atoms with SOC and attractive s-wave interactions. The SOC is generated by a pair of counterpropagating Raman lasers (see Fig. 4.1), with recoil wave vector k_r, energy $E_r = \hbar^2 k_r^2/2m$, and characteristic time scale $t_r = \hbar/E_r$, giving the SOC strength $\alpha = \hbar^2 k_r/m$. These lasers couple two hyperfine atomic states representing the pseudospins $\sigma = \uparrow, \downarrow$ (for example, $|\uparrow\rangle \equiv |f = 9/2, m_F = -7/2\rangle$ and $|\downarrow\rangle \equiv |f = 9/2, m_F = -9/2\rangle$ in ^{40}K atoms [124]). The transverse Zeeman potential strength $V_Z = \Omega_{\mathrm{R}}/2$, set by the Raman coupling strength [93], is varied in time to drive the TQPT. Here we consider varying Ω_{R} linearly from 0 to $\Omega_{\mathrm{R}f}$ in a time t_{ramp}, and back in the same time: a piecewise linear ramp protocol of duration $2t_{\mathrm{ramp}}$ [see blue curve in Fig. 4.2(a)]. Because our protocol starts with Raman lasers off ($\Omega_{\mathrm{R}} = 0$), it is straightforward to experimentally realize a long-lived conventional superfluid (SF) as the initial state [125]; as we will see below, t_{ramp} is much less than the system's lifetime (either limited by the spontaneous emission of the Raman lasers or inelastic scattering from the Feshbach resonances).

Written in the Nambu basis $\Psi_k(t) = (\psi_{k\uparrow}(t), \psi_{k\downarrow}(t), \psi^\dagger_{-k\downarrow}(t), -\psi^\dagger_{-k\uparrow}(t))^\top$, the system's Hamiltonian is $H(t) = \frac{1}{2}\int dk \Psi_k(t)^\dagger \mathcal{H}_{\mathrm{BdG},k}(t)\Psi_k(t)$, where $\psi_{k\sigma}(\psi^\dagger_{k\sigma})$ denote the annihilation (creation) operators for fermions with momentum k and spin σ.

The BdG Hamiltonian is

$$\mathcal{H}_{\mathrm{BdG},k}(t) = \xi_k(t)\tau_z + \alpha k \tau_z \sigma_z + \frac{\Omega_{\mathrm{R}}(t)}{2}\sigma_x + \Delta(t)\tau_x, \tag{4.1}$$

where $\boldsymbol{\sigma}$ and $\boldsymbol{\tau}$ are vectors of Pauli operators acting on spin and particle-hole space, respectively. Here, $\xi_k(t) = \hbar^2 k^2/2m - \mu(t)$ combines the kinetic energy and the chemical potential $\mu(t)$, which is determined self-consistently to keep the number of atoms fixed.

The mean-field pairing potential

$$\Delta(t)e^{i\vartheta(t)} = g_{1\mathrm{D}} \int \langle \psi_{k\uparrow}(t)\psi_{-k\downarrow}(t)\rangle dk \tag{4.2}$$

is also self-consistently determined, where $\langle \dots \rangle$ denotes averaging with respect to the initial thermal distribution. The attractive effective 1D coupling constant $g_{1\mathrm{D}} < 0$ can be controlled by Feshbach tuning the three-dimensional (3D) scattering length [126, 127, 128]. In Eq. (4.1), we used the transformed basis where $\psi_{k\sigma}(t) \to \psi_{k\sigma}(t)\exp[i\vartheta(t)/2]$, giving a real pairing potential: $\Delta(t)\exp[i\vartheta(t)] \to \Delta(t)$.

The instantaneous quasiparticle excitation spectrum of the BdG Hamiltonian [see Fig. 3.14] consists of four bands, $E_{n,k} = \mathrm{sgn}(n)\epsilon_{(-1)^n,k}$, where $n = \pm 1, \pm 2$ and

$$\begin{aligned} \epsilon^2_{\pm,k}(t) &= \frac{\Omega_{\mathrm{R}}(t)^2}{4} + \Delta(t)^2 + \xi_k(t)^2 + \alpha^2 k^2 \\ &\quad \pm 2\sqrt{\xi_k(t)^2\left[\alpha^2 k^2 + \frac{\Omega_{\mathrm{R}}(t)^2}{4}\right] + \Delta(t)^2\frac{\Omega_{\mathrm{R}}(t)^2}{4}}. \end{aligned} \tag{4.3}$$

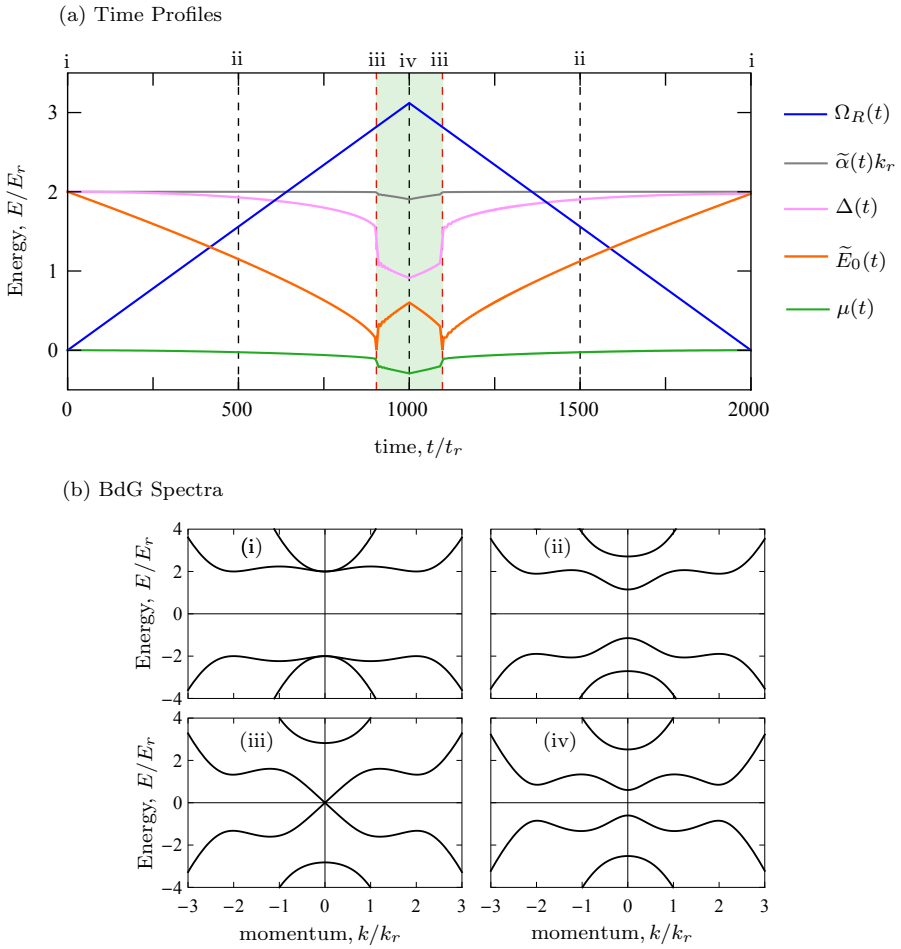

Figure 4.2: (a) Time profiles of $\Omega_{\mathrm{R}}(t)$, $\widetilde{\alpha}(t)k_r$, $\Delta(t)$, $\widetilde{E}_0(t)$, and $\mu(t)$ for $t_{\mathrm{ramp}} = 1000t_r$. The dashed lines denote the times whose instantaneous band diagrams are plotted in (b). The red dashed lines mark the critical times when TQPT happens, and the shaded region corresponds to the topological regime. Plots are obtained from numerically solving the td-BdGE [Eq. (4.12)] self-consistently [Eqs. (4.13a) and (4.13b)] with initial parameters: $\Omega_{\mathrm{R}}(0) = 0$, $\Delta(0) = 2E_r$ and $\mu(0) = 0$ for SOC strength $\alpha = 2E_r/k_r$ and $t_{\mathrm{ramp}} = 1000t_r$. (b) Quasiparticle spectra at different Zeeman potentials Ω_{R}. From top to bottom, the energy bands are labeled by $E_{2,k}, E_{1,k}, E_{-1,k}$, and $E_{-2,k}$. The parameters are as follows: (i) $\Omega_{\mathrm{R}} = 0$, $\Delta = 2E_r$, $\mu = 0$, (ii) $\Omega_{\mathrm{R}} = 1.56E_r$, $\Delta = 1.93E_r$, $\mu = -0.02E_r$, (iii) $\Omega_{\mathrm{R}} = 2.8E_r$, $\Delta = 1.4E_r$, $\mu = -0.14E_r$, and (iv) $\Omega_{\mathrm{R}} = 3.12E_r$, $\Delta = 0.91E_r$, $\mu = -0.3E_r$.

Since $\mathcal{H}_{\mathrm{BdG},k}$ respects particle-hole symmetry, the spectrum is symmetric around $E = 0$. As shown in Fig. 4.2(b), the instantaneous energy spectrum is gapped for

$k \neq 0$; however, for $k = 0$ the gap closes when $\epsilon_{-,0}(t) = \Omega_{\rm R}(t)/2 - \sqrt{\Delta(t)^2 + \mu(t)^2} = 0$. Such a gap closing without change in the symmetry of the ground state (which remains SF for all $\Omega_{\rm R}$) signifies a TQPT between topological $[\epsilon_{-,0}(t) > 0]$ and conventional SF phases $[\epsilon_{-,0}(t) < 0]$. For $\Omega_{\rm R} = 0$, the positive and negative bands are doubly degenerate at $k = 0$; any nonzero $\Omega_{\rm R}$ lifts this degeneracy.

To study the dynamics around the TQPT, we propose to prepare conventional SFs $[\epsilon_{-,0}(t) < 0]$ at nonzero temperature T. We then drive the system through the TQPT by changing $\Omega_{\rm R}$ according to our ramp protocol with $\Omega_{{\rm R}f} > 2\sqrt{\Delta_f^2 + \mu_f^2}$ (where the subscript f denotes the quantities at time $t = t_{\rm ramp}$) such that the ramp crosses the TQPT (see Fig. 4.2).

4.3.1 Analytical Results

We first analytically study the dynamics, considering the simple case of slow ramps at $T = 0$. In this limit, excitations occur near $k = 0$ and at the transition times $t = t_{c(1,2)}$, given by the roots of $\Omega_{\rm R}(t_c) = 2\sqrt{\Delta(t_c)^2 + \mu(t_c)^2}$, where the Fermi gas changes from conventional to topological SF and vice versa. For $\hbar^2 k^2/2m \ll \alpha k$, we approximate

$$\mathcal{H}_{{\rm BdG},k}(t) \approx \alpha k \tau_z \sigma_z - \mu(t)\tau_z + \frac{\Omega_{\rm R}(t)}{2}\sigma_x + \Delta(t)\tau_x. \tag{4.4}$$

In this limit, excitations occur only between the $E_{1,k}$ and $E_{-1,k}$ bands [see Fig. 4.2(b)]. At $k = 0$, the eigenenergies are $\pm\widetilde{E}_0(t)$, where $\widetilde{E}_0(t) = |\sqrt{\Delta(t)^2 + \mu(t)^2} - \Omega_{\rm R}(t)/2|$

with eigenstates

$$\widetilde{\phi}_0^+(t) = \begin{pmatrix} \cos\frac{\theta(t)}{2} \\ \\ \sin\frac{\theta(t)}{2} \end{pmatrix} \otimes \frac{1}{\sqrt{2}} \begin{pmatrix} 1 \\ \\ 1 \end{pmatrix}, \tag{4.5a}$$

$$\widetilde{\phi}_0^-(t) = \begin{pmatrix} -\sin\frac{\theta(t)}{2} \\ \\ \cos\frac{\theta(t)}{2} \end{pmatrix} \otimes \frac{1}{\sqrt{2}} \begin{pmatrix} 1 \\ \\ -1 \end{pmatrix}, \tag{4.5b}$$

where $\widetilde{\phi}_0^{\pm}(t)$ corresponds to positive and negative bands [with pseudospin $|\pm\rangle \equiv (|\uparrow\rangle \pm |\downarrow\rangle)/\sqrt{2}$] and $\cos\theta(t) \equiv \mu(t)/\sqrt{\Delta(t)^2 + \mu(t)^2}$. In the subspace of these eigenstates, the effective low-energy Hamiltonian near $k = 0$ is

$$\widetilde{\mathcal{H}}_{\mathrm{BdG},k}(t) \;\; = \;\; \widetilde{\alpha}(t) k \eta_x + \widetilde{E}_0(t) \eta_z, \tag{4.6}$$

where $\widetilde{\alpha}(t) = \alpha \sin\theta(t)$, $\eta_x = \widetilde{\phi}_0^+(t)[\widetilde{\phi}_0^-(t)]^\dagger + \mathrm{H.c.}$, $\eta_z = \widetilde{\phi}_0^+(t)[\widetilde{\phi}_0^+(t)]^\dagger - \widetilde{\phi}_0^-(t)[\widetilde{\phi}_0^-(t)]^\dagger$, and $2\eta_y = -i[\eta_z, \eta_x]$. Equation (4.6) is a two-parameter driven Hamiltonian [129] with instantaneous energy eigenvalues $\pm\widetilde{E}_k(t)$, where $\widetilde{E}_k(t) = \sqrt{\widetilde{E}_0(t)^2 + \widetilde{\alpha}(t)^2 k^2}$.

We analyze the dynamics of the TQPT using $\widetilde{\mathcal{H}}_{\mathrm{BdG},k}(t)$, where the single-particle state of the system at time t is given by

$$\widetilde{\phi}_k(t) = b_k^+(t) \begin{pmatrix} w_k^+(t) \\ \\ \mathrm{sgn}(k) w_k^-(t) \end{pmatrix} + b_k^-(t) \begin{pmatrix} -\mathrm{sgn}(k) w_k^-(t) \\ \\ w_k^+(t) \end{pmatrix}, \tag{4.7}$$

with the initial conditions $b_k^+(0) = 0$ and $b_k^-(0) = 1$. These two-component vectors

are expressed in the basis $\widetilde{\phi}_0^{\pm}$ with $w_k^{\pm}(t) = \sqrt{[1 \pm \widetilde{E}_0(t)/\widetilde{E}_k(t)]/2}$. The Schrödinger equation for the system then leads to

$$i\hbar\partial_t \mathbf{b}_k(t) = \widetilde{\mathcal{H}}_{\mathrm{BdG},k}(t)\mathbf{b}_k(t), \tag{4.8}$$

where $\mathbf{b}_k(t) = (b_k^+(t), b_k^-(t))^\top$.

We make further analytical progress by ignoring the self-consistency condition so that the system can be treated as a collection of two-level systems for each $(k, -k)$ pair and use the adiabatic-impulse approximation [109, 130, 131, 132, 133] that describes such periodic dynamics accurately for low frequency and/or large amplitude drives. Within this approximation, excitations are produced only near the critical gap-closing times $t_{c(1,2)}$ when the system enters the impulse regime; otherwise, the dynamics occur adiabatically in each band and the system accumulates a dynamical phase $U(t_f, t_i) = \exp[-i\eta_z \int_{t_i}^{t_f} dt\widetilde{E}_k(t)/\hbar]$. In the former regime, near the gap-closing times $t_{c(1,2)}$, excitations are produced and the evolution operator is [109]

$$N = \sqrt{1-p_k}[i\sin(\varphi_{\mathrm{S},k}) - \eta_z\cos(\varphi_{\mathrm{S},k})] - i\eta_y\sqrt{p_k}, \tag{4.9}$$

where $p_k = \exp(-2\pi\delta_k)$ is the probability of excitation formation in each passage through the critical point [96, 97] with $\delta_k = (\alpha k)^2/(2\hbar|d\widetilde{E}_0(t)/dt|_{t_c})$, and $\varphi_{\mathrm{S},k} = \pi/4 + \delta_k(\ln\delta_k - 1) + \arg\Gamma(1 - i\delta_k)$ is the Stokes phase originating from the interference of the parts of the system wave function in the instantaneous ground and excited states at $t = t_{c(1,2)}$ with $\arg\Gamma(1-i\delta_k)$ being the argument of the gamma

function [134]. These results give the probability of defect formation

$$P_k^{\mathrm{ex}} = 4p_k(1-p_k)\sin^2\Phi_{\mathrm{St},k} \tag{4.10}$$

at $t = 2t_{\mathrm{ramp}}$, where $\Phi_{\mathrm{St},k} = \zeta_{2k}+\varphi_{\mathrm{S},k}$ is the Stückelberg phase and $\zeta_{2k} = \int_{t_{c1}}^{t_{c2}} dt\widetilde{E}_k(t)/\hbar$ is the dynamical phase factor accumulated during passage between the two crossings of the gap-closing points [109, 132]. Since the excitations occur near $k \sim 0$ where the $E_{\pm 1,k}$ band approximately corresponds to pseudospin $|\pm\rangle$ (along the x direction), P_k^{ex} is directly related to changes in the SRMD $\delta n_{k\pm}$ measured along the pseudospin x direction. Furthermore, within these approximations, $|d\widetilde{E}_0(t)/dt|_{t_{c(1,2)}} = \Omega_{\mathrm{R}f}/(2t_{\mathrm{ramp}})$, and it can be shown that P_k^{ex} is a function of $k\sqrt{t_{\mathrm{ramp}}}$ only (see Appendix C for the derivation). Thus, the integrated change of the SRMD $\delta\widetilde{n}_{\pm} = \int dk\delta n_{k\pm}$ displays KZ scaling $\sim \sqrt{t_{\mathrm{ramp}}}$ of defect density for a system dynamically evolved through the TQPT.

4.3.2 Numerical Results

We now show that these properties persist even when the self-consistency conditions for $\Delta(t)$ and $\mu(t)$ are imposed, as well as at nonzero T (see Fig. 4.3).

We solve for the dynamics of the single-particle density matrix

$$\rho_k^{ab}(t) = \langle \Psi_k^{\dagger a}(t)\Psi_k^b(t)\rangle \tag{4.11}$$

self-consistently and at finite initial temperature, where a, b denote the indices of

elements in the Nambu basis. The density matrix obeys the equation of motion [Eq. (4.1)]

$$i\hbar\partial_t\rho_k(t) = [\mathcal{H}_{\mathrm{BdG},k}(t), \rho_k(t)], \tag{4.12}$$

subject to the self-consistency conditions (see Appendix D for the derivation)

$$\Delta(t) = \frac{g_{1\mathrm{D}}}{4}\int dk \mathrm{Tr}(\rho_k(t)\tau_x), \tag{4.13a}$$

$$\mu(t) = \frac{g_{1\mathrm{D}}}{4\Delta(t)}\int dk \mathrm{Tr}\left(\rho_k(t)\Lambda_k(t)\right), \tag{4.13b}$$

where $\Lambda_k(t) = \left(\hbar^2k^2/2m + \alpha k\sigma_z\right)\tau_x - \Delta(t)\tau_z$. Our system begins in the thermal state

$$\rho_k(t) = \sum_{\substack{n \\ E_{n,k}(0)<0}} f_{n,k}\chi_{n,k}(t)\chi^\dagger_{n,k}(t) + (1-f_{n,k})\widetilde{\chi}_{n,-k}(t)\widetilde{\chi}^\dagger_{n,-k}(t), \tag{4.14}$$

where $f_{n,k} = [\exp(E_{n,k}(0)/k_\mathrm{B}T)+1]^{-1}$ is the Fermi function of the initial Hamiltonian, and k_B is Boltzmann's constant. The wave function $\chi_{n,k}(t)$ with its particle-hole conjugate $\widetilde{\chi}_{n,k}(t) = \tau_y\sigma_y\chi^*_{-n,-k}(t)$ begins as eigenfunctions of the initial Hamiltonian and evolves according to $i\hbar\partial_t\chi_{n,k}(t) = \mathcal{H}_{\mathrm{BdG},k}(t)\chi_{n,k}(t)$. Figure 4.2(a) shows the resulting time profiles of the pairing potential and chemical potential obtained from solving the td-BdGE (see Appendix E for remarks on the numerical simulation).

We numerically solved the td-BdGE for the change in the SRMD

$$\delta n_{k\pm} = \mathrm{Tr}\left([\rho_k(2t_{\mathrm{ramp}}) - \rho_k(0)] \left[\left(\frac{1+\tau_z}{2} \right) \otimes \left(\frac{1 \pm \sigma_x}{2} \right) \right] \right). \tag{4.15}$$

Figure 4.3 shows that δn_{k-} still exhibits Stückelberg oscillations even with inclusion of the self-consistency conditions and at $T > 0$. Furthermore, for $t_{\mathrm{ramp}} \gg \hbar/\Delta_f$, we still see $\delta n_{k\pm} \sim k\sqrt{t_{\mathrm{ramp}}}$ (see Appendix F for an explicit demonstration of the scaling), and the integrated change in SRMD $\delta\widetilde{n}_{\pm} = \int dk \delta n_{k\pm}$ therefore scales with $\sqrt{t_{\mathrm{ramp}}}$, thus, showing the robustness of such interference phenomenon in the present system. We verified that these features appear only if $\Omega_{\mathrm{R}f} > 2\sqrt{\Delta_f^2 + \mu_f^2}$, where the ramp takes the system through the TQPT; thus both the KZ scaling and the presence of Stückelberg oscillations mark the TQPT. In our calculation, we ignored the effect of phase fluctuation as this effect can be suppressed by coupling an array of 1D SOCFGs [135, 136, 137, 138].

The parameters used for the plots in Fig. 4.3 are realistic for 1D SOCFG experiments. For experiments with ^{40}K, the Raman laser beams, coupling the $|\uparrow\rangle \equiv |9/2, -7/2\rangle$ and $|\downarrow\rangle \equiv |9/2, -9/2\rangle$ states, have laser wavelength $\lambda_r = 768.86$ nm, giving the recoil energy $E_r = h \times 8.445$ kHz, and time $t_r = \hbar/E_r \approx 20$ μs [124]. The single-body decay time due to photons scattering from the Raman lasers is about 60 ms [124], and the lifetime owing to three-body recombination is about 200 ms [141]. We consider SOCFGs with Fermi energy $E_{\mathrm{F}} = E_r$. The 1D Fermi gas criterion is satisfied when $E_{\mathrm{F}} < \hbar\omega_\perp$; for the lateral trapping frequency $\omega_\perp/2\pi = 5 \times 10^4$ Hz, which corresponds to characteristic harmonic oscillator length $d_\perp = \sqrt{\hbar/m\omega_\perp} \approx$

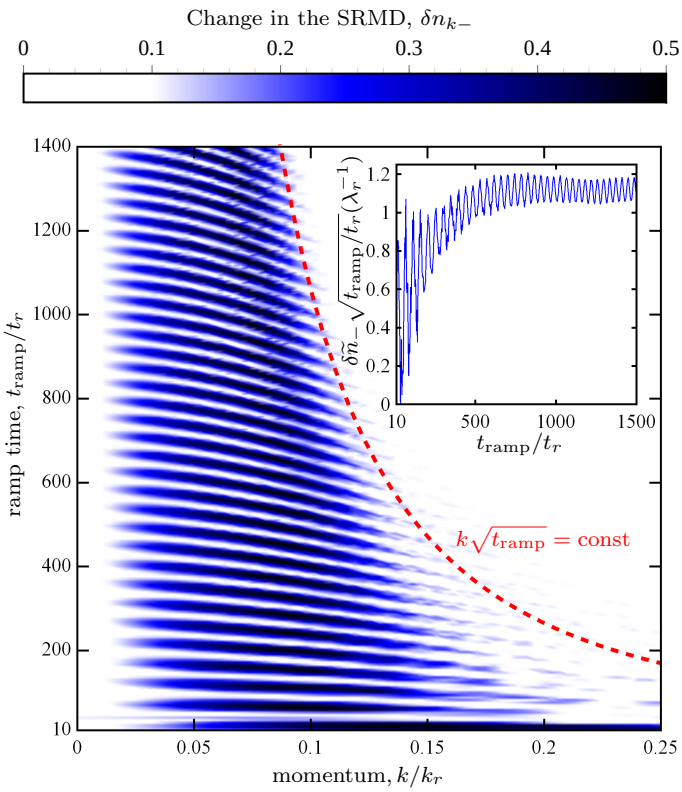

Figure 4.3: Change in the SRMD δn_{k-} for spin $|-\rangle = (|\uparrow\rangle - |\downarrow\rangle)/\sqrt{2}$ as a function of $t_{\rm ramp}/t_r$ and k/k_r. For large $t_{\rm ramp}$, the width of the oscillation envelopes scales with $1/\sqrt{t_{\rm ramp}}$ as shown by the red dashed line. δn_{k-} is symmetric with respect to $k = 0$; thus, for illustration purposes, we only plot δn_{k-} for $k \geq 0$. Note that $\delta n_{k+} = -\delta n_{k-}$. Inset: Integrated change in SRMD $\delta\widetilde{n}_- = \int dk \delta n_{k-}$ as a function of $t_{\rm ramp}/t_r$ exhibiting oscillations, with the amplitude of the oscillations at large $t_{\rm ramp}$ scaling like $\sqrt{t_{\rm ramp}}$, as can be read off directly from the y axis. The plots are obtained by numerically solving Eq. (4.12) self-consistently [Eqs. (4.13a) and (4.13b)] with initial conditions $\mu(0) = 0$, $\Delta(0) = 2E_r$, and $\Omega_{\rm R}(0) = 0$ for a temperature $k_{\rm B}T = 0.1E_{\rm F}$ (which is below the critical temperature $T_c = 0.19T_{\rm F}$ [139, 140]), SOC strength $\alpha = 2E_r/k_r$, and $\Omega_{{\rm R}f} = 3.12E_r$.

$1345a_0$, where a_0 is the Bohr radius; the parameters used in the calculation for the plots in Fig. 4.3 correspond to linear density $\widetilde{n} \approx 5\ \mu\text{m}^{-1}$ and 1D interaction strength $g_{\rm 1D} \approx -0.73E_r\lambda_r$ (or 3D scattering length $a_{\rm 3D} \approx -2870a_0$ [128]). For these values, Fig. 4.3 shows that the Stückelberg oscillations and KZ scaling behavior of

the SRMD can be observed within the experimentally limiting single-body decay time ($\approx 3000t_r$) and thus is feasible experimentally.

4.4 Conclusion

In this chapter we study the dynamics of 1D SOCFGs quenched across the TQPT from conventional to TSFs and back. Such a ramp allows us to mitigate spontaneous emission effects from SOC that destabilize the TSF. We found that for sufficiently slow ramps, the change in the SRMD has Stückelberg oscillations and exhibits KZ scaling with the ramp time. Both the oscillations and scaling behaviors can be measured experimentally from the time-of-flight measurement and thus can be used to verify the gap closing of Bogoliubov quasiparticles spectrum at zero momentum. Such a gap closure is a unique signature for the TQPT.

Our dip-in-dip-out protocol is quite general and can be gainfully used for observing features related to quantum phase transitions between long-lived and short-lived phases of ultracold bosonic and fermionic atoms. In addition, it provides a route to escaping the heating problem, which is one of the major obstacles in measuring properties of such systems in or near their short-lived phases. Moreover, our work also shows that such a protocol applied to ultracold atom systems, including the one we analyzed in detail, may provide us with test beds for observation of both KZ scaling [100, 101, 102, 103, 104, 105, 106, 107] and Stückelberg interference phenomenon [142, 143, 144].

Chapter 5

Conclusion

In recent years, there has been a great interest in realizing topological superconductors which host MZMs at the boundaries or defects. This is driven mainly by the prospect of using MZMs as the building blocks for a fault-tolerant topological quantum computer.

In Chapter 1, we gave an introduction of MZM and topological superconductors. In particular, we focused on two models of topological superconductors, namely, the spinless p-wave superconductor and the spin-split spin-orbit-coupled superconducting, which are the models studied in this thesis. We also reviewed several signatures of the topological superconductors and the experimental progress done in detecting the MZMs.

In Chapter 2, we generalized the BTK formalism to calculate analytically the conductance in NS junctions involving topological superconductors. We provided a comprehensive analysis of the conductance spectroscopy across the TQPT. We show that in the topological regime, the topological NS junction necessarily gives rise to a $2e^2/h$ zero-bias conductance at zero temperature. Another important finding of our work is that when the junction transparency is not small, the zero-bias conductance can be quantized without developing a peak in the spectra.

In Chapter 3, we calculated the current and conductance of SNS junctions involving topological superconductors using the scattering matrix formalism. We explored various combinations of the SNS junctions where none, one or both of the superconductors can be in the topological regime. We verified that the MZM conductance, probed using an s-wave superconducting lead with a gap Δ_s, is quantized at $(4-\pi)2e^2/h$ at the gap-bias voltages $eV = \pm\Delta_s$ in the tunneling limit (small junction transparencies). In this limit where only single Andreev reflections contribute to the current, the conductance for voltages $e|V| < \Delta_s$ is zero. However, when the junction transparency is not small, there is a finite conductance for $e|V| < \Delta_s$ arising from MAR. The conductance at $eV = \pm\Delta_s$ in this case is no longer quantized. Moreover, we found that unlike the case of s-wave superconducting probe lead with a BCS singularity (where $\sum_{\sigma=\uparrow,\downarrow} |u_\sigma|^2 = \sum_{\sigma=\uparrow,\downarrow} |v_\sigma|^2$ at the gap edge with u and v being the electron and hole component of the BdG superconducting wavefunction at the gap edge), the MZM tunneling conductance measured using a superconducting lead without a BCS singularity has a non-universal value which decreases with decreasing junction transparencies. We have also shown that for some parameter values, the conductance of a zero-energy ABS may look very similar to that of a Majorana, such that the two cases may not be distinguishable within experimental resolution. This implies that, despite other benefits of using SNS junctions to probe MZMs, conductance quantization may not be a robust and definitive experimental signature. Finally, we showed that for finite-energy ABSs, the conductance peaks shift away from the gap bias voltage $eV = \pm\Delta_{\text{lead}}$ to a larger value set by the ABSs energy.

In Chapter 4, we proposed a bulk probe to detect the topological phase. Specifically, we demonstrated that dynamical probes can be used to detect the topological quantum phase transition. The detection of such a phase transition would constitute smoking-gun evidence of the unique bulk properties of the topological phase. Such a bulk probe is more reliable than the local detection applied so far in the solid state, which is susceptible to disorder effects. Our dip-in dip-out protocol, where the system is prepared in its long-lived non-topological phase and driven into the topological phase and back, mitigates the heating problem due to spontaneous emission. We showed that the excitations' momentum distributions exhibit Stückelberg oscillations and Kibble-Zurek scaling characteristic of the topological phase transition.

In this thesis, we have investigated several signatures of Majorana zero modes. We provide a comprehensive analysis of each signature by studying systems *with* and *without* MZMs. Our work has important implications for the extensive current experimental efforts toward detecting topological superconductivity and MZMs. Moreover, our detailed analysis for each of the detection scheme should be a useful guide for future experimental work in detecting the MZMs in the solid-state and ultracold atom settings.

Appendix A

Remarks on Numerical Calculation for The Conductance in SNS Junctions

In this appendix we give a few remarks for the numerical calculation of the conductance in the SNS junctions discussed in Chapter 3. The scattering matrices at the left (S_L) and right NS interfaces (S_R) [Eq. (3.1)] can calculated numerically from Kwant [79] by constructing the tight-binding models for the corresponding NS junctions. Since the scattering matrices given by Kwant are calculated using the current amplitudes with arbitrary phases at each energy, one can fix the phases by setting the largest element of the current amplitudes for every energy to be real.

We note that Eqs. (3.1)(a) and (3.1)(c) are invariant under the transformation:

$$\begin{aligned} t^{\text{in}}_{L,R}(E) &\to t^{\text{in}}_{L,R}(E)U^{\dagger}_{L,R}(E), \\ \mathcal{J}^{\text{in}}_{L,R}(E) &\to U_{L,R}(E)\mathcal{J}^{\text{in}}_{L,R}(E), \end{aligned} \tag{A.1}$$

where $t^{\text{in}}_{L,R}(E)$ is the transmission matrices at the left and right NS interfaces, $U_{L,R}(E)$ are unitary matrices, and $\mathcal{J}^{\text{in}}_{L,R}(E)$ are the input current amplitudes from the left and right NS interfaces. By polar decomposition, there exists a unitary

matrix $U_{L,R}(E)$ such that $t^{\text{in}}_{L,R}(E) = \widetilde{t}^{\text{in}}_{L,R}(E)U^{\dagger}_{L,R}(E)$, where

$$\widetilde{t}^{\text{in}}_{L,R}(E) = \sqrt{t^{\text{in}}_{L,R}(E)[t^{\text{in}}_{L,R}(E)]^{\dagger}} = \sqrt{\mathbb{1} - r_{L,R}(E)r^{\dagger}_{L,R}(E)}, \tag{A.2}$$

with $r_{L,R}$ being the reflection matrices at the left and right NS interfaces. For computational efficiency, we obtained only the reflection matrices $r_{L,R}$ from Kwant and used Eq. (A.2) to calculate the transmission matrix.

For the numerical evaluation of Eq. (3.4), we used an energy cutoff E_c in the summation over energy where E_c is chosen such that the calculation converges for each voltage V. The introduction of the energy cutoff sets the following constraint on the scattering matrix:

$$S^{e}_{N}(E, E + eV) = S^{h}_{N}(-E, -(E + eV)) = -\mathbb{1}, \tag{A.3}$$

for all $E > E_c$. The above constraint is required for the unitarity of the scattering matrices to hold.

Appendix B

Proof for The Non-negativity of The Current in SNS Junctions

In this appendix we give a proof for the non-negativity of the current in SNS junctions. The current amplitude in the normal region is given by

$$\widetilde{j}^{\mathrm{tot}}_{\ell,\nu}(E) = \widetilde{j}^{e}_{\ell,\nu}(E) + \widetilde{j}^{h}_{\ell,\nu}(E), \tag{B.1}$$

where

$$\widetilde{j}^{\tau}_{\ell,\nu}(E) = \sum_{\sigma=\uparrow,\downarrow} j^{\tau,\sigma,+}_{\ell,\nu}(E) - j^{\tau,\sigma,-}_{\ell,\nu}(E), \tag{B.2}$$

is the electron/hole ($\tau = e/h$) component of the current in the left ($\ell = NL$) or right ($\ell = NR$) normal region. Since the electron (hole) energy increases (decreases) by eV every time it passes from the left to the right, we have

$$\widetilde{j}^{e}_{NL,\nu}(E) = \widetilde{j}^{e}_{NR,\nu}(E + eV), \tag{B.3a}$$

$$\widetilde{j}^{h}_{NL,\nu}(E) = \widetilde{j}^{h}_{NR,\nu}(E - eV). \tag{B.3b}$$

From Eqs. (B.1) and (B.3), we obtain the following recurrence relation

$$\widetilde{j}^{e}_{NL,\nu}(E) = \widetilde{j}^{\mathrm{tot}}_{NL,\nu}(E) - \widetilde{j}^{\mathrm{tot}}_{NR,\nu}(E - eV) + \widetilde{j}^{e}_{NL,\nu}(E - 2eV), \tag{B.4}$$

which implies that

$$\widetilde{j}^{e}_{NL,\nu}(E) = \sum_{n=0}^{\infty} \widetilde{j}^{\mathrm{tot}}_{NL,\nu}(E - 2neV) - \widetilde{j}^{\mathrm{tot}}_{NR,\nu}(E - (2n+1)eV). \tag{B.5}$$

The total electrical current is given by

$$I_{\nu} = \frac{2e}{h} \int dE \sum_{m} \left[\widetilde{j}^{e}_{NL,\nu}(E + 2meV) - \widetilde{j}^{h}_{NL,\nu}(E + 2meV) \right]. \tag{B.6}$$

Multiplying the integrand of Eq. (B.6) by V, we have the power dissipated by the SNS junction as

$$
\begin{aligned}
I_\nu V &= \frac{2eV}{h}\int dE \sum_m \left[2\widetilde{j}^{e}_{NL,\nu}(E+2meV) - \widetilde{j}^{\rm tot}_{NL,\nu}(E+2meV)\right], \\
&= \frac{2eV}{h}\int dE \sum_m \Bigg\{2\sum_{n\geq 0}\left[\widetilde{j}^{\rm tot}_{NL,\nu}(E+2(m-n)eV) - \widetilde{j}^{\rm tot}_{NR,\nu}(E+(2(m-n)-1)eV)\right] \\
&\qquad\qquad - \widetilde{j}^{\rm tot}_{NL,\nu}(E+2meV)\Bigg\}, \\
&= \frac{2eV}{h}\int dE \sum_m \Bigg\{2\sum_{m'\leq m}\left[\widetilde{j}^{\rm tot}_{NL,\nu}(E+2m'eV) - \widetilde{j}^{\rm tot}_{NR,\nu}(E+(2m'-1)eV)\right] \\
&\qquad\qquad - \widetilde{j}^{\rm tot}_{NL,\nu}(E+2meV)\Bigg\}, \\
&= \frac{2eV}{h}\int dE \Bigg\{2\sum_{m'}(m_{\rm max}-m'+1)\left[\widetilde{j}^{\rm tot}_{NL,\nu}(E+2m'eV) - \widetilde{j}^{\rm tot}_{NR,\nu}(E+(2m'-1)eV)\right] \\
&\qquad\qquad - \sum_m \widetilde{j}^{\rm tot}_{NL,\nu}(E+2meV)\Bigg\}, \\
&= \frac{2eV}{h}\int dE \sum_m \left[(2m-1)\widetilde{j}^{\rm tot}_{NR,\nu}(E+(2m-1)eV) - 2m\widetilde{j}^{\rm tot}_{NL,\nu}(E+2meV)\right] \geq 0.
\end{aligned}
\tag{B.7}
$$

So, for $V \geq 0$, we have $I_\nu \geq 0$. In lines 1 and 2, we have made use of Eqs. (B.1) and (B.5), respectively. In lines 4 and 5 of Eq. (B.7), we have used the current conservation equation:

$$
\sum_m \left[\widetilde{j}^{\rm tot}_{NL,\nu}(E+2meV) - \widetilde{j}^{\rm tot}_{NR,\nu}(E+(2m-1)eV)\right] = 0, \tag{B.8}
$$

and the fact that $\pm(E+neV)\widetilde{j}^{\rm tot}_{NL/NR,\nu}(E+neV) \geq 0$ is the power dissipated by current $\widetilde{j}^{\rm tot}_{NL/NR,\nu}$.

Appendix C

Adiabatic-Impulse Approximation

In this appendix we derive the Kibble Zurek scaling of the excitations' momentum distribution of the 1D SOCFGs subjected to the dip-in dip-out protocol described in Chapter 4. The equation of motion $i\hbar\partial_t \mathbf{b}_k(t) = \widetilde{\mathcal{H}}_{\mathrm{BdG},k}(t)\mathbf{b}_k(t)$ [Eq. (4.8)], where $\mathbf{b}_k(t) = (b_k^+(t), b_k^-(t))^\top$ [Eq. (4.7)] and $\widetilde{\mathcal{H}}_{\mathrm{BdG},k}(t) = \widetilde{\alpha}(t)k\eta_x + \widetilde{E}_0(t)\eta_z$ [Eq. (4.6)] with η_x and η_z being the Pauli matrices acting on the subspace $\widetilde{\phi}_0^{\pm}(t)$ [Eq. (4.5)], can be expressed in form of two-decoupled second-order differential equations as

$$\left\{-\hbar^2\partial_t^2 - \widetilde{E}_k(t)^2 + i\hbar\left[\mp\partial_t\widetilde{E}_0(t) \pm \widetilde{E}_0(t)\partial_t - \frac{\partial_t\widetilde{\alpha}(t)}{\widetilde{\alpha}(t)}\left[i\hbar\partial_t \mp \widetilde{E}_0(t)\right]\right]\right\} b_k^{\pm} = 0. \tag{C.1}$$

Assuming no self-consistency, we can use the adiabatic-impulse approximation [109] to write Eq. (C.1) as $\mathbf{b}_k(t) = V\mathbf{b}_k(0)$ where the total evolution operator V is decomposed into adiabatic U and impulse N operators. The adiabatic (impulse) regime corresponds to the time duration far away from (near) the critical gap-closing time

$t_{c(1,2)}$. In matrix form we can write down U as

$$U_j = \begin{pmatrix} e^{-i\zeta_{jk}} & 0 \\ 0 & e^{i\zeta_{jk}} \end{pmatrix}, \quad j = 1, 2, 3, \tag{C.2}$$

where the dynamical phases are given by $\zeta_{1k} = \int_0^{t_{c1}} dt\widetilde{E}_k(t)/\hbar$, $\zeta_{2k} = \int_{t_{c1}}^{t_{c2}} dt\widetilde{E}_k(t)/\hbar$, and $\zeta_{3k} = \int_{t_{c2}}^{2t_{\rm ramp}} dt\widetilde{E}_k(t)/\hbar$. The impulse operator N can be written as [109]

$$N = \begin{pmatrix} \sqrt{1-p_k}e^{-i\widetilde{\varphi}_{{\rm S},k}} & -\sqrt{p_k} \\ \sqrt{p_k} & \sqrt{1-p_k}e^{i\widetilde{\varphi}_{{\rm S},k}} \end{pmatrix}, \tag{C.3}$$

where $p_k = \exp(2\pi\delta_k)$ is the LZ transition probability [96, 97] at each critical time, $\delta_k = (\alpha k)^2/(2\hbar|d\widetilde{E}_0(t)/dt|_{t_c})$, $\widetilde{\varphi}_{{\rm S},k} = \varphi_{{\rm S},k} - \pi/2$ and $\varphi_{{\rm S},k} = \pi/4 + \delta_k(\ln\delta_k - 1) + \arg\Gamma(1-i\delta_k)$. The Stokes phase $\varphi_{{\rm S},k}$ increases monotonously from 0 in the adiabatic limit ($\delta_k \to \infty$) to $\pi/4$ in the diabatic or fast driving limit ($\delta_k \to 0$), as seen from the asymptotic argument of the gamma function [134]

$$\arg\,\Gamma(1-i\delta_k) \approx \begin{cases} C\delta_k, & \delta_k \ll 1, \\ -\frac{\pi}{4} - \delta_k(\ln\delta_k - 1), & \delta_k \gg 1, \end{cases} \tag{C.4}$$

where $C \approx 0.58$ is the Euler constant. At the end of the ramp protocol, the total evolution operator becomes

$$V = U_3 N U_2 N U_1 = \begin{pmatrix} \beta_k & -\gamma_k^* \\ \gamma_k & \beta_k^* \end{pmatrix}, \tag{C.5}$$

with matrix elements

$$\begin{aligned}\beta_k &= (1-p_k)e^{-i\zeta_{+k}} - p_k e^{-i\zeta_{-k}},\\ \gamma_k &= \sqrt{(1-p_k)p_k}e^{i(\widetilde{\varphi}_{\mathrm{S},k}+2\zeta_{3k})}\left(e^{-i\zeta_{+k}} + e^{-i\zeta_{-k}}\right),\end{aligned} \tag{C.6}$$

where the phases are given by $\zeta_{+k} = \zeta_{1k} + \zeta_{2k} + \zeta_{3k} + 2\widetilde{\varphi}_{\mathrm{S},k}$ and $\zeta_{-k} = \zeta_{1k} - \zeta_{2k} + \zeta_{3k}$. The probability of defect formation at the end of the ramp protocol (at $t = 2t_{\mathrm{ramp}}$) is then given by

$$P_k^{\mathrm{ex}} = |\gamma_k|^2 = 4p_k(1-p_k)\sin^2\Phi_{\mathrm{St},k}, \tag{C.7}$$

where $\Phi_{\mathrm{St},k} = \zeta_{2k} + \varphi_{\mathrm{S},k}$ is the Stückelberg phase. Note that in the case of no-self consistency, $|d\widetilde{E}_0(t)/dt| = \Omega_{\mathrm{R}f}/(2t_{\mathrm{ramp}})$, and consequently δ_k is a function of $k\sqrt{t_{\mathrm{ramp}}}$. Since p_k and $\varphi_{\mathrm{S},k}$ are functions of δ_k, P_k^{ex} is also a function of $k\sqrt{t_{\mathrm{ramp}}}$. As a result, the defect density displays Kibble-Zurek scaling $\sim \sqrt{t_{\mathrm{ramp}}}$.

Appendix D

Self-Consistency Condition

In this appendix we derive the self-consistency condition for the chemical potential in the td-BdGE used in Chapter 4. The self-consistent chemical potential $\mu(t)$ [Eq. (4.13b)] is derived from the constraint on the particle density $\widetilde{n}$, i.e.,

$$\int dk \mathrm{Tr}\left(\rho_k(t)\left(\frac{1+\tau_z}{2}\right)\right) = \widetilde{n}. \tag{D.1}$$

Taking the time derivative of Eq. (D.1), i.e., $i\hbar\partial_t\rho_k(t) = [\mathcal{H}_{\mathrm{BdG},k}(t), \rho_k(t)]$, and using the cyclic property of trace, we have

$$\begin{aligned}
\frac{1}{2}\int dk \mathrm{Tr}([\mathcal{H}_{\mathrm{BdG},k}(t), \rho_k(t)]\tau_z) &= 0 \\
\frac{1}{2}\int dk \mathrm{Tr}([\tau_z, \mathcal{H}_{\mathrm{BdG},k}(t)]\rho_k(t)) &= 0 \\
\int dk \mathrm{Tr}(\tau_y\rho_k(t)) &= 0.
\end{aligned} \tag{D.2}$$

Differentiating Eq. (D.2) with respect to time and using the cyclic property of trace, we then obtain

$$\int dk \mathrm{Tr}(\tau_y[\mathcal{H}_{\mathrm{BdG},k}(t), \rho_k(t)]) = 0$$

$$\int dk \mathrm{Tr}([\mathcal{H}_{\mathrm{BdG},k}(t), \tau_y]\rho_k(t)) = 0$$

$$\int dk \mathrm{Tr}\left((\hbar^2 k^2/2m - \mu(t) + \alpha k \sigma_z)\tau_x \rho_k(t) - \Delta(t)\tau_z \rho_k(t)\right) = 0. \tag{D.3}$$

Noting that $g_{1\mathrm{D}} \int dk \mathrm{Tr}(\rho_k(t)\tau_x)/4 = \Delta(t)$, we then have the self-consistent chemical potential $\mu(t)$ as

$$\mu(t) = \frac{g_{1\mathrm{D}}}{4\Delta(t)} \int dk \mathrm{Tr}\left((\hbar^2 k^2/2m + \alpha k \sigma_z)\tau_x \rho_k(t) - \Delta(t)\tau_z \rho_k(t)\right). \tag{D.4}$$

Appendix E

Remarks on The Numerical Simulation of The Time-Dependent Bogoliubov-de Gennes Equation

In Sec. 4.3.2, the td-BdGE is given in terms of the single-particle density matrix $\rho_k(t)$. The td-BdGE can also be written in terms of the wave function $\chi_{n,k}(t) = (u_{n,k\uparrow}(t), u_{n,k\downarrow}(t), v_{n,k\downarrow}(t), -v_{n,k\uparrow}(t))^\top$ as

$$i\hbar\partial_t \chi_{n,k}(t) = \mathcal{H}_{\mathrm{BdG},k}(t)\chi_{n,k}(t), \tag{E.1}$$

subject to the self-consistency conditions

$$\Delta(t) = \frac{g_{1\mathrm{D}}}{4} \sum_{\substack{n \\ E_{n,k}(0)<0}} \int dk \mathcal{I}^-_{n,k}(t), \tag{E.2a}$$

$$\mu(t) = \frac{g_{1\mathrm{D}}}{4\Delta(t)} \sum_{\substack{n \\ E_{n,k}(0)<0}} \int dk \left[\frac{\hbar^2 k^2}{2m} \mathcal{I}^-_{n,k}(t) + \alpha k \mathcal{I}^+_{n,k}(t) - \Delta(t)\mathcal{Q}_{n,k}(t) \right], \tag{E.2b}$$

where

$$\mathcal{I}^\pm_{n,k}(t) = (2f_{n,k} - 1)\{[v^*_{n,k\downarrow}(t)u_{n,k\uparrow}(t) \pm u_{n,k\downarrow}(t)v^*_{n,k\uparrow}(t)] + \mathrm{H.c.}\}, \tag{E.3a}$$

$$\mathcal{Q}_{n,k}(t) = (2f_{n,k} - 1)\sum_\sigma (|u_{n,k\sigma}|^2 - |v_{n,k\sigma}|^2), \tag{E.3b}$$

with $f_{n,k} = [\exp(E_{n,k}(0)/k_{\mathrm{B}}T) + 1]^{-1}$ being the Fermi function of the initial Hamiltonian.

The self-consistent solution of the td-BdGE involves solving a large number of coupled time-dependent differential equations (one for each k point). To reduce the number of time-dependent variables, we first calculated the self-consistent $\Delta(t)$ and $\mu(t)$ in the adiabatic regime by solving the time-independent BdG equation. The td-BdGE was then solved self-consistently for a small range of states near $k = 0$ where excitations occur. Since the $\pm k$ eigenstates are related by $\mathrm{X}_{n,-k} = \sigma_x \mathrm{X}_{n,k}$, we accelerated the computation by focusing on $k \geq 0$. Solving the td-BdGE self-consistently with the Zeeman potential $\Omega_{\mathrm{R}}(t)$ varied according the piecewise linear ramp protocol (see blue curve in Fig. 4.2(a)), we obtained $\widetilde{\alpha}(t)$, $\Delta(t)$, $\widetilde{E}_0(t)$, and $\mu(t)$ as shown in Fig. 4.2(a).

Appendix F

Spin-Resolved Momentum Distribution

In the appendix we show explicitly the Kibble Zurek scaling of the spin-resolved momentum distribution in Fig. 4.3. The change in spin-resolved momentum distribution δn_{k-} shows Stückelberg oscillations with the ramp time t_{ramp} and for large t_{ramp}, δn_{k-} scales with $\sqrt{t_{\text{ramp}}}$, as shown in Fig. 4.3 in Chapter 5. In Fig. F.1, we demonstrate the scaling more explicitly by plotting δn_{k-} as a function of scaled momentum $k/k_r\sqrt{t_{\text{ramp}}/t_r}$.

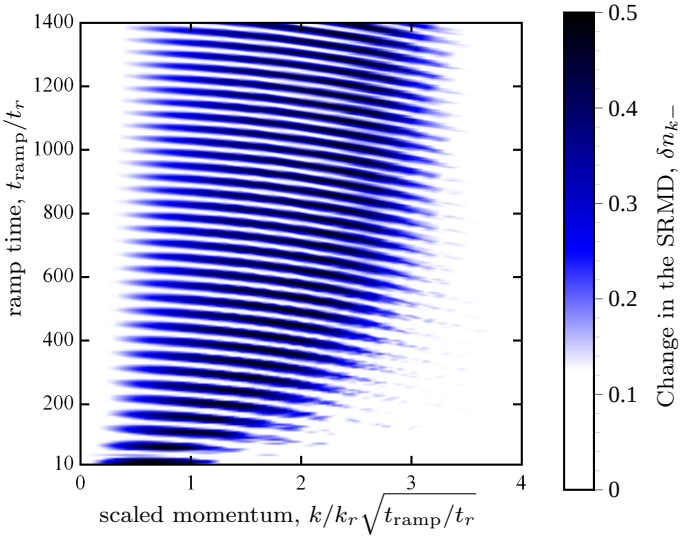

Figure F.1: Change in the SRMD δn_{k-} for pseudospin $|-\rangle = (|\uparrow\rangle - |\downarrow\rangle)/\sqrt{2}$ as a function of $t_{\rm ramp}/t_r$ and $k/k_r\sqrt{t_{\rm ramp}/t_r}$. Note that δn_{k-} is a function of $k\sqrt{t_{\rm ramp}}$ only for large $t_{\rm ramp}$, as seen from its almost flat nature for small k/k_r and the width of its oscillation envelopes. The scaling of δn_{k-} can be read off directly from the x axis. δn_{k-} is symmetric with respect to $k = 0$; thus, for illustration purposes, we only plot δn_{k-} for $k \geq 0$. The plots are obtained by numerically solving the td-BdGE self-consistently with initial conditions $\Omega_{\rm R}(0) = 0$, $\Delta(0) = 2E_r$ and $\mu(0) = 0$ for a temperature $k_{\rm B}T = 0.1E_{\rm F}$ (which is below the critical temperature $T_c = 0.19T_{\rm F}$ [139, 140]), SOC strength $\alpha = 2E_r/k_r$, and $\Omega_{{\rm R}f} = 3.12E_r$. Note that $\delta n_{k+} = -\delta n_{k-}$ due to particle number conservation.

List of Publications

Publications this thesis is based on:

1. *Conductance spectroscopy of topological superconductor wire junctions*
   F. Setiawan, P. M. R. Brydon, Jay D. Sau, and S. Das Sarma, Phys. Rev. B **91**, 214513 (2015).

2. *Conductance spectroscopy of nontopological-topological superconductor junctions*
   F. Setiawan, W. S. Cole, Jay D. Sau, and S. Das Sarma, Phys. Rev. B 95, 020501(R) (2017).

3. *Transport in superconductor–normal metal–superconductor junctions: spinful p-wave and spin-orbit-coupled topological wire*
   F. Setiawan, W. S. Cole, Jay D. Sau, and S. Das Sarma, arXiv:1703.02047.

4. *Dynamical detection of topological phase transitions in short-lived atomic systems*
   F. Setiawan, K. Sengupta, I. B. Spielman and Jay D. Sau, Phys. Rev. Lett. **115**, 190401 (2015).

Other publications and preprints that I contributed to:

1. *Robust two-qubit gates for exchange-coupled qubits*
   F. Setiawan, H.-Y. Hui, J. Kestner, X. Wang, and S. Das Sarma, Phys. Rev. B **89**, 085314 (2014).

2. *Detecting topological superconductivity using Shapiro steps*
   Jay D. Sau and **F. Setiawan**, Phys. Rev. B 95, 060501(R) (2017).

3. *Temperature-dependent many-body effects in Dirac-Weyl materials: Interacting compressibility and quasiparticle velocity*
   F. Setiawan and S. Das Sarma, Phys. Rev. B **92**, 235103 (2015).

Bibliography

[1] E. Majorana, Nuovo Cimento **5**, 171 (1937).

[2] G. E. Volovik, *The universe in a helium droplet* (Oxford University Press, 2003).

[3] A. Y. Kitaev, Phys. Usp. **44**, 131 (2001).

[4] N. Read and D. Green, Phys. Rev. B **61**, 10267 (2000).

[5] D. A. Ivanov, Phys. Rev. Lett. **86**, 268 (2001).

[6] N. B. Kopnin and M. M. Salomaa, Phys. Rev. B **44**, 9667 (1991).

[7] G. E. Volovik, Journal of Experimental and Theoretical Physics Letters **70**, 609 (1999).

[8] T. Senthil and M. P. A. Fisher, Phys. Rev. B **61**, 9690 (2000).

[9] S. Das Sarma, C. Nayak, and S. Tewari, Phys. Rev. B **73**, 220502 (2006).

[10] L. Fu and C. L. Kane, Phys. Rev. Lett. **100**, 096407 (2008).

[11] J. D. Sau, R. M. Lutchyn, S. Tewari, and S. Das Sarma, Phys. Rev. Lett. **104**, 040502 (2010).

[12] J. D. Sau, S. Tewari, R. M. Lutchyn, T. D. Stanescu, and S. Das Sarma, Phys. Rev. B **82**, 214509 (2010).

[13] R. M. Lutchyn, J. D. Sau, and S. Das Sarma, Phys. Rev. Lett. **105**, 077001 (2010).

[14] Y. Oreg, G. Refael, and F. von Oppen, Phys. Rev. Lett. **105**, 177002 (2010).

[15] J. Alicea, Phys. Rev. B **81**, 125318 (2010).

[16] V. Mourik *et al.*, Science **336**, 1003 (2012).

[17] L. P. Rokhinson, X. Liu, and J. K. Furdyna, Nat. Phys. **8**, 795 (2012).

[18] M. T. Deng *et al.*, Nano Lett. **12**, 6414 (2012).

[19] A. Das *et al.*, Nat. Phys. **8**, 887 (2012).

[20] A. D. K. Finck, D. J. Van Harlingen, P. K. Mohseni, K. Jung, and X. Li, Phys. Rev. Lett. **110**, 126406 (2013).

[21] H. O. H. Churchill *et al.*, Phys. Rev. B **87**, 241401 (2013).

[22] H. Zhang *et al.*, arXiv:1603.04069 (2016).

[23] M. Deng *et al.*, Science **354**, 1557 (2016).

[24] J. Chen *et al.*, arXiv:1610.04555 (2016).

[25] J. Alicea, Rep. Prog. Phys. **75**, 076501 (2012).

[26] M. Leijnse and K. Flensberg, Semicond. Sci. Technol. **27**, 124003 (2012).

[27] T. D. Stanescu and S. Tewari, J. Phys. Condens. Matter **25**, 233201 (2013).

[28] C. W. J. Beenakker, Annu. Rev. Con. Mat. Phys. **4**, 113 (2013).

[29] S. R. Elliott and M. Franz, Rev. Mod. Phys. **87**, 137 (2015).

[30] S. D. Sarma, M. Freedman, and C. Nayak, NPJ Quantum Information **1**, 15001 (2015).

[31] C. Beenakker and L. Kouwenhoven, Nature Physics **12**, 618 (2016).

[32] K. Sengupta, I. Žutić, H.-J. Kwon, V. M. Yakovenko, and S. Das Sarma, Phys. Rev. B **63**, 144531 (2001).

[33] K. T. Law, P. A. Lee, and T. K. Ng, Phys. Rev. Lett. **103**, 237001 (2009).

[34] K. Flensberg, Phys. Rev. B **82**, 180516 (2010).

[35] M. Wimmer, A. R. Akhmerov, J. P. Dahlhaus, and C. W. J. Beenakker, New J. Phys. **13**, 053016 (2011).

[36] F. Setiawan, P. M. R. Brydon, J. D. Sau, and S. Das Sarma, Phys. Rev. B **91**, 214513 (2015).

[37] C. Nayak, S. H. Simon, A. Stern, M. Freedman, and S. Das Sarma, Rev. Mod. Phys. **80**, 1083 (2008).

[38] S. Mi, D. I. Pikulin, M. Wimmer, and C. W. J. Beenakker, Phys. Rev. B **87**, 241405 (2013).

[39] T.-P. Choy, J. M. Edge, A. R. Akhmerov, and C. W. J. Beenakker, Phys. Rev. B **84**, 195442 (2011).

[40] M. Duckheim and P. W. Brouwer, Phys. Rev. B **83**, 054513 (2011).

[41] S. B. Chung, H.-J. Zhang, X.-L. Qi, and S.-C. Zhang, Phys. Rev. B **84**, 060510 (2011).

[42] L. Mao, M. Gong, E. Dumitrescu, S. Tewari, and C. Zhang, Phys. Rev. Lett. **108**, 177001 (2012).

[43] J. D. Sau and S. Das Sarma, Nat. Commun. **3**, 964 (2012).

[44] Y. Kim, M. Cheng, B. Bauer, R. M. Lutchyn, and S. Das Sarma, Phys. Rev. B **90**, 060401 (2014).

[45] P. M. R. Brydon, S. Das Sarma, H.-Y. Hui, and J. D. Sau, Phys. Rev. B **91**, 064505 (2015).

[46] H.-Y. Hui, P. M. R. Brydon, J. D. Sau, S. Tewari, and S. Das Sarma, Sci. Rep. **5**, 8880 (2015).

[47] S. Nadj-Perge, I. K. Drozdov, B. A. Bernevig, and A. Yazdani, Phys. Rev. B **88**, 020407 (2013).

[48] A. R. Akhmerov, J. P. Dahlhaus, F. Hassler, M. Wimmer, and C. W. J. Beenakker, Phys. Rev. Lett. **106**, 057001 (2011).

[49] C.-H. Lin, J. D. Sau, and S. Das Sarma, Phys. Rev. B **86**, 224511 (2012).

[50] R. M. Lutchyn and J. H. Skrabacz, Phys. Rev. B **88**, 024511 (2013).

[51] C. R. Reeg and D. L. Maslov, arXiv preprint arXiv:1702.05046 (2017).

[52] Y. Peng, F. Pientka, Y. Vinkler-Aviv, L. I. Glazman, and F. von Oppen, Phys. Rev. Lett. **115**, 266804 (2015).

[53] F. von Oppen, Y. Peng, and F. Pientka, *Topological superconducting phases in one dimension* (http://topo-houches.pks.mpg.de/wp-content/uploads/2015/09/lecture_Oppen.pdf).

[54] A. L. Yeyati, J. C. Cuevas, A. López-Dávalos, and A. Martín-Rodero, Phys. Rev. B **55**, R6137 (1997).

[55] S. Nadj-Perge *et al.*, Science **346**, 602 (2014).

[56] B. E. Feldman *et al.*, Nat. Phys. **13**, 286 (2017).

[57] F. Setiawan, W. S. Cole, J. D. Sau, and S. Das Sarma, Phys. Rev. B **95**, 020501 (2017).

[58] F. Setiawan, W. S. Cole, J. D. Sau, and S. Das Sarma, arXiv:1703.02047 (2017).

[59] F. Setiawan, K. Sengupta, I. B. Spielman, and J. D. Sau, Phys. Rev. Lett. **115**, 190401 (2015).

[60] D. Roy, N. Bondyopadhaya, and S. Tewari, Phys. Rev. B **88**, 020502 (2013).

[61] T. D. Stanescu, R. M. Lutchyn, and S. Das Sarma, Phys. Rev. B **84**, 144522 (2011).

[62] E. Prada, P. San-Jose, and R. Aguado, Phys. Rev. B **86**, 180503 (2012).

[63] J. J. He, T. K. Ng, P. A. Lee, and K. T. Law, Phys. Rev. Lett. **112**, 037001 (2014).

[64] S. Rex and A. Sudbø, Phys. Rev. B **90**, 115429 (2014).

[65] G. E. Blonder, M. Tinkham, and T. M. Klapwijk, Phys. Rev. B **25**, 4515 (1982).

[66] S. Kashiwaya and Y. Tanaka, Reports on Progress in Physics **63**, 1641 (2000).

[67] B. Braunecker, G. I. Japaridze, J. Klinovaja, and D. Loss, Phys. Rev. B **82**, 045127 (2010).

[68] J. Klinovaja and D. Loss, Phys. Rev. B **86**, 085408 (2012).

[69] X. Liu, J. D. Sau, and S. Das Sarma, Phys. Rev. B **92**, 014513 (2015).

[70] T. D. Stanescu, R. M. Lutchyn, and S. Das Sarma, Phys. Rev. B **90**, 085302 (2014).

[71] S. Takei, B. M. Fregoso, H.-Y. Hui, A. M. Lobos, and S. Das Sarma, Phys. Rev. Lett. **110**, 186803 (2013).

[72] M. Cheng, R. M. Lutchyn, V. Galitski, and S. Das Sarma, Phys. Rev. Lett. **103**, 107001 (2009).

[73] M. Cheng, R. M. Lutchyn, V. Galitski, and S. Das Sarma, Phys. Rev. B **82**, 094504 (2010).

[74] S. Das Sarma, J. D. Sau, and T. D. Stanescu, Phys. Rev. B **86**, 220506 (2012).

[75] D. Rainis, L. Trifunovic, J. Klinovaja, and D. Loss, Phys. Rev. B **87**, 024515 (2013).

[76] D. Averin and A. Bardas, Phys. Rev. Lett. **75**, 1831 (1995).

[77] M. Octavio, M. Tinkham, G. E. Blonder, and T. M. Klapwijk, Phys. Rev. B **27**, 6739 (1983).

[78] T. Klapwijk, G. Blonder, and M. Tinkham, Physica B+ C **109**, 1657 (1982).

[79] C. W. Groth, M. Wimmer, A. R. Akhmerov, and X. Waintal, New Journal of Physics **16**, 063065 (2014).

[80] M. Hurd, S. Datta, and P. F. Bagwell, Phys. Rev. B **54**, 6557 (1996).

[81] M. Hurd, S. Datta, and P. F. Bagwell, Phys. Rev. B **56**, 11232 (1997).

[82] A. Zazunov, R. Egger, and A. Levy Yeyati, Phys. Rev. B **94**, 014502 (2016).

[83] U. Gunsenheimer and A. D. Zaikin, Phys. Rev. B **50**, 6317 (1994).

[84] P. San-Jose, J. Cayao, E. Prada, and R. Aguado, New Journal of Physics **15**, 075019 (2013).

[85] G. Kells, D. Meidan, and P. W. Brouwer, Phys. Rev. B **86**, 100503 (2012).

[86] S. Das Sarma, A. Nag, and J. D. Sau, Phys. Rev. B **94**, 035143 (2016).

[87] C.-X. Liu, J. D. Sau, and S. Das Sarma, Phys. Rev. B **95**, 054502 (2017).

[88] J. Dalibard, F. Gerbier, G. Juzeliūnas, and P. Öhberg, Rev. Mod. Phys. **83**, 1523 (2011).

[89] H. Zhai, International Journal of Modern Physics B **26**, 1230001 (2012).

[90] V. Galitski and I. B. Spielman, Nature **494**, 49 (2013).

[91] N. Goldman, G. Juzeliūnas, P. Öhberg, and I. B. Spielman, Reports on Progress in Physics **77**, 126401 (2014).

[92] H. Zhai, Reports on Progress in Physics **78**, 026001 (2015).

[93] Y.-J. Lin, K. Jiménez-García, and I. Spielman, Nature **471**, 83 (2011).

[94] L. W. Cheuk *et al.*, Phys. Rev. Lett. **109**, 095302 (2012).

[95] P. Wang *et al.*, Phys. Rev. Lett. **109**, 095301 (2012).

[96] L. Landau, Phys. Z. Sowjetunion **2**, 1 (1932).

[97] C. Zener, Proc. R. Soc. London, Ser. A **137**, 696 (1932).

[98] T. W. Kibble, Journal of Physics A: Mathematical and General **9**, 1387 (1976).

[99] W. H. Zurek, Nature **317**, 505 (1985).

[100] L. Sadler, J. Higbie, S. Leslie, M. Vengalattore, and D. Stamper-Kurn, Nature **443**, 312 (2006).

[101] C. N. Weiler *et al.*, Nature **455**, 948 (2008).

[102] G. Lamporesi, S. Donadello, S. Serafini, F. Dalfovo, and G. Ferrari, Nature Physics **9**, 656 (2013).

[103] D. Chen, M. White, C. Borries, and B. DeMarco, Physical Review Letters **106**, 235304 (2011).

[104] N. Navon, A. L. Gaunt, R. P. Smith, and Z. Hadzibabic, Science **347**, 167 (2015).

[105] S. Braun *et al.*, Proceedings of the National Academy of Sciences **112**, 3641 (2015).

[106] L. Corman *et al.*, Phys. Rev. Lett. **113**, 135302 (2014).

[107] L. Chomaz *et al.*, Nature communications **6** (2015).

[108] E. C. G. Stückelberg, Helv. Phys. Acta **5**, 369 (1932).

[109] S. Shevchenko, S. Ashhab, and F. Nori, Physics Reports **492**, 1 (2010).

[110] M. Greiner, O. Mandel, T. W. Hänsch, and I. Bloch, Nature **419**, 51 (2002).

[111] S. Mondal, D. Pekker, and K. Sengupta, EPL (Europhysics Letters) **100**, 60007 (2013).

[112] U. Divakaran and K. Sengupta, Phys. Rev. B **90**, 184303 (2014).

[113] C. Zhang, S. Tewari, R. M. Lutchyn, and S. Das Sarma, Phys. Rev. Lett. **101**, 160401 (2008).

[114] M. Sato, Y. Takahashi, and S. Fujimoto, Phys. Rev. Lett. **103**, 020401 (2009).

[115] J. D. Sau, R. Sensarma, S. Powell, I. B. Spielman, and S. Das Sarma, Phys. Rev. B **83**, 140510 (2011).

[116] A. Bermudez, D. Patanè, L. Amico, and M. A. Martin-Delgado, Phys. Rev. Lett. **102**, 135702 (2009).

[117] A. Bermudez, L. Amico, and M. Martin-Delgado, New Journal of Physics **12**, 055014 (2010).

[118] W. DeGottardi, D. Sen, and S. Vishveshwara, New Journal of Physics **13**, 065028 (2011).

[119] E. Perfetto, Phys. Rev. Lett. **110**, 087001 (2013).

[120] A. Rajak and A. Dutta, Phys. Rev. E **89**, 042125 (2014).

[121] G. Kells, D. Sen, J. K. Slingerland, and S. Vishveshwara, Phys. Rev. B **89**, 235130 (2014).

[122] P. D. Sacramento, Phys. Rev. E **90**, 032138 (2014).

[123] S. Hegde, V. Shivamoggi, S. Vishveshwara, and D. Sen, New Journal of Physics **17**, 053036 (2015).

[124] R. A. Williams, M. C. Beeler, L. J. LeBlanc, K. Jiménez-García, and I. B. Spielman, Phys. Rev. Lett. **111**, 095301 (2013).

[125] M. Greiner, C. A. Regal, and D. S. Jin, Nature **426**, 537 (2003).

[126] T. Bergeman, M. G. Moore, and M. Olshanii, Phys. Rev. Lett. **91**, 163201 (2003).

[127] G. E. Astrakharchik, D. Blume, S. Giorgini, and L. P. Pitaevskii, Phys. Rev. Lett. **93**, 050402 (2004).

[128] X.-J. Liu, H. Hu, and P. D. Drummond, Phys. Rev. A **76**, 043605 (2007).

[129] J. D. Sau and K. Sengupta, Physical Review B **90**, 104306 (2014).

[130] B. Damski, Physical review letters **95**, 035701 (2005).

[131] B. Damski and W. H. Zurek, Physical Review A **73**, 063405 (2006).

[132] A. Dutta, A. Das, and K. Sengupta, Physical Review E **92**, 012104 (2015).

[133] J. Dziarmaga, Advances in Physics **59**, 1063 (2010).

[134] I. S. Gradshteyn and I. M. Ryzhik, *Table of integrals, series, and products* (Academic press, 2014).

[135] T. Mizushima and M. Sato, New Journal of Physics **15**, 075010 (2013).

[136] J. D. Sau, B. I. Halperin, K. Flensberg, and S. Das Sarma, Phys. Rev. B **84**, 144509 (2011).

[137] M. Cheng and H.-H. Tu, Phys. Rev. B **84**, 094503 (2011).

[138] L. Fidkowski, J. Alicea, N. H. Lindner, R. M. Lutchyn, and M. P. A. Fisher, Phys. Rev. B **85**, 245121 (2012).

[139] S. Nascimbene, N. Navon, K. Jiang, F. Chevy, and C. Salomon, Nature **463**, 1057 (2010).

[140] M. J. Ku, A. T. Sommer, L. W. Cheuk, and M. W. Zwierlein, Science **335**, 563 (2012).

[141] C. A. Regal, M. Greiner, and D. S. Jin, Phys. Rev. Lett. **92**, 083201 (2004).

[142] M. Mark *et al.*, Physical review letters **99**, 113201 (2007).

[143] S. Kling, T. Salger, C. Grossert, and M. Weitz, Physical review letters **105**, 215301 (2010).

[144] A. Zenesini, D. Ciampini, O. Morsch, and E. Arimondo, Physical Review A **82**, 065601 (2010).